



53 Leninsky prospect, 117924 Moscow, Russia

ISTC 007012
(Partner ISTC Project #1865-P)

Approved by Dr. A.N.Starodub,
Director of
Quantum Radiophysics Institute of
Lebedev Physics Institute

"01" August 2001

First-overtone CO laser: gain kinetics, RF discharge and atmospheric spectroscopy

Final report

01 August 2000 - 31 July 2001

Project manager:

Prof. A.Ionin

Participants:

Prof. A.Napartovich

Prof. Yu.Konev

Dr. A.Kotkov

Mr. D.Sinitsyn

Dr. A.Kurnosov

Dr. I.Kochetov

Dr. S.Ivanov

Mrs. N.Ionina

Mr. L.Seleznev

Mr. Yu.Klimachev

Moscow, 2001

REPORT DOCUMENTATION PAGE

Form Approved OMB No. 0704-0188

Public reporting burden for this collection of information is estimated to average 1 hour per response, including the time for reviewing instructions, searching existing data sources, gathering and maintaining the data needed, and completing and reviewing the collection of information. Send comments regarding this burden estimate or any other aspect of this collection of information, including suggestions for reducing the burden, to Department of Defense, Washington Headquarters Services, Directorate for Information Operations and Reports (0704-0188), 1215 Jefferson Davis Highway, Suite 1204, Arlington, VA 22202-4302. Respondents should be aware that notwithstanding any other provision of law, no person shall be subject to any penalty for failing to comply with a collection of information if it does not display a currently valid OMB control number.

PLEASE DO NOT RETURN YOUR FORM TO THE ABOVE ADDRESS.

1. REPORT DATE (DD-MM-YYYY) 23-08-2001			2. REPORT TYPE Final Report		3. DATES COVERED (From – To) 01/08/2000 - 10-Oct-01	
4. TITLE AND SUBTITLE First overtone CO laser: gain kinetics, RF discharge properties, and atmospheric spectroscopy			5a. CONTRACT NUMBER ISTC Registration No: 1865			
			5b. GRANT NUMBER			
			5c. PROGRAM ELEMENT NUMBER			
6. AUTHOR(S) Prof. Andrei Alekseevich Ionine			5d. PROJECT NUMBER			
			5d. TASK NUMBER			
			5e. WORK UNIT NUMBER			
7. PERFORMING ORGANIZATION NAME(S) AND ADDRESS(ES) Lebedev Physics Institute 53 Leninsky Prospect Moscow 117924 Russia				8. PERFORMING ORGANIZATION REPORT NUMBER N/A		
9. SPONSORING/MONITORING AGENCY NAME(S) AND ADDRESS(ES) EOARD PSC 802 BOX 14 FPO 09499-0014				10. SPONSOR/MONITOR'S ACRONYM(S)		
				11. SPONSOR/MONITOR'S REPORT NUMBER(S) ISTC 00-7012		
12. DISTRIBUTION/AVAILABILITY STATEMENT Approved for public release; distribution is unlimited						
13. SUPPLEMENTARY NOTES						
14. ABSTRACT The main objective of the Project was a complex study of first-overtone (FO) CO laser kinetics, RF discharge features and atmospheric spectroscopy, which is extremely important for getting recommendations for a development of RF discharge FO CO laser and delivery its radiation to the object. Experimental and theoretical activity on the Project consisted of three main tasks which were carried out in parallel: <ul style="list-style-type: none">• Experimental and theoretical study of FO CO laser active medium characteristics.• Feasibility study experiments on studying the radio-frequency (RF) discharge in gas mixtures containing CO molecules and preliminary theoretical calculations of its properties.• Experimental study and theoretical analysis of IR radiation absorption coefficients for different organic and non-organic substances near the wavelengths corresponding to FO CO laser spectrum lines.						
15. SUBJECT TERMS EOARD, Electrotechnology & Fluidics, Lasers & Masers						
16. SECURITY CLASSIFICATION OF:			17. LIMITATION OF ABSTRACT UL	18. NUMBER OF PAGES 85	19a. NAME OF RESPONSIBLE PERSON Dr. Alexander J. Glass	
a. REPORT UNCLAS	b. ABSTRACT UNCLAS	c. THIS PAGE UNCLAS			19b. TELEPHONE NUMBER (Include area code) +44 20 7514-4953.	

This work was supported financially by EOARD, USA and performed under the contract to the International Science and Technology Center (ISTC), Moscow

Contents	
Introduction	3
Part I. Theoretical and experimental study of FO CO laser gain kinetics and spectrum formation	5
Introduction	5
1.1. Re-examination of data for MQE model of CO overtone laser	5
<i>1.1.1. Calculations of constants for processes CO(v)+N₂(0) ®CO(v-2)+N₂(1)</i>	6
<i>1.1.2. Incorporation of new kinetic and spectral constants into the full kinetic model of the first overtone CO laser</i>	8
<i>1.1.3. Theoretical modeling of gain and laser characteristics of the FO CO laser</i>	1
<i>1.1.4. Room-temperature overtone laser evaluation</i>	0
<i>1.1.5. Analysis of cross sections for electron induced transitions between vibrational levels of N₂ and CO</i>	1
<i>1.1.6. Gain saturation effects in CO laser active medium</i>	2
<i>1.1.7. Conclusions</i>	7
1.2. Experimental study of FO CO laser gain and spectrum formation	2
<i>1.2.1. Measurement of SSG build up and rise time</i>	2
<i>1.2.2. SSG measurement with master oscillator - laser amplifier system</i>	2
<i>1.2.3. FO CO laser spectrum formation</i>	4
1.3. Comparative analysis of experimental and theoretical results	2
1.4. Conclusions	5
Part II. Theoretical and experimental study of RF discharge in gas mixtures with CO	2
Introduction	9
2.1. RF discharge modeling for CO laser conditions	2
<i>2.1.1. Fast flow discharge modeling</i>	9
<i>2.1.2. Discharge model for a diffusion cooled CO slab laser</i>	2
2.2. Experiments on RF discharge in gas mixtures containing CO molecules	3
<i>2.2.1. Modification of the experimental RF discharge installation.</i>	7
<i>2.2.2. Power supply, measuring system and additional electrical setup.</i>	3
<i>2.2.3. Experiments on RF discharge in transversal "slab" geometry.</i>	8

<i>2.2.4. Experimental measurements of impedance and maximal SIP depending on mixture content and gas pressure.</i>	4
<i>2.2.5. Data analysis</i>	1
Conclusions	4
Part III. Resonant absorption of first-overtone CO laser radiation by atmospheric water vapor and pollutants	4
Introduction	4
3.1. Spectroscopy of atmospheric gases within FO CO lasing spectral range	4
3.2. Theoretical model for nonlinear absorption of FO CO laser radiation	4
<i>3.2.1. Main equations of theoretical model</i>	4
<i>3.2.2 Multifrequency radiation</i>	7
<i>3.2.3 Gas-dynamic model</i>	5
3.3. Simulation of nonlinear absorption	5
3.4. Experiments on absorption of FO CO laser radiation by gaseous substances	5
<i>3.4.1. Experimental facility</i>	5
<i>3.4.2. Experimental results</i>	5
Conclusions	6
Tables	6
References	7
List of publications	8
	2

Introduction

The main objective of the Project was a complex study of first-overtone (FO) CO laser kinetics, RF discharge features and atmospheric spectroscopy, which is extremely important for getting recommendations for a development of RF discharge FO CO laser and delivery its radiation to the object. Experimental and theoretical activity on the Project consisted of three main tasks which were carried out in parallel:

Task 1. Experimental and theoretical study of FO CO laser active medium characteristics (gain parameters for different spectral lines depending on laser mixture content, output characteristics of FO CO laser operating in different spectral modes) to obtain understanding of new features of kinetic processes on high vibrational levels of CO molecules. Modifications of FO CO laser model improving description of vibrational and electron kinetics.

Subtask 1.1. Modification of cryogenically cooled electron beam sustained discharge laser chamber. Optical windows of the chamber should be modified to diminish optical losses of polarized radiation inside the laser cavity. These losses should be minimized and controlled in the experiments with maximal accuracy. Experimental measurements of FO CO laser output characteristics on high vibrational transition of CO molecule depending on the relative concentration of nitrogen in the laser mixture. Preparation of data on multi-quantum exchange rate coefficients for CO molecules for inclusion into the laser kinetic model.

Subtask 1.2. Experimental measurements of small signal gain (SSG) on several ro-vibrational overtone transitions ($V \rightarrow V-2$) of CO molecule. The technique of calibrated intracavity optical losses will be applied for these measurements: time delay of the beginning of lasing will be defined under the fixed value of optical losses in the laser resonator. The temporal behavior of SSG in active medium of the laser will be monitored by varying the intracavity optical losses. Calculations of new data on multi-quantum exchange probabilities for CO-N₂ collisions for different gas temperatures.

Subtask 1.3. Experimental measurements of SSG on high ro-vibrational overtone transitions of CO molecule for different laser gas mixtures. Experimental measurements of gain dynamics for single line CO laser radiation using "master oscillator - power amplifier" (MOPA) system to define gain parameters in the active medium of CO laser. Incorporation of modified vibrational exchange rate coefficients into the full kinetic model of FO CO laser. Analysis of cross sections for electron induced transitions between vibrational levels of N₂ and CO.

Subtask 1.4. Experimental study of output characteristics of the FO CO laser operating on high ro-vibrational transitions depending on active gas mixture content. Comparative analysis of the experimental and calculated data on SSG and saturated gain in active medium of CO laser. Simulations of experimental measurements of gain and laser characteristics using modified full kinetic model.

Task 2. Feasibility study experiments on studying the radio-frequency (RF) discharge in gas mixtures containing CO molecules and preliminary theoretical calculations of its properties. Defining of conditions of stable RF discharge sustaining in "slab" geometry of the electrode system.

Subtask 2.1. Modification of the experimental RF discharge CO₂ laser installation to obtain a possibility of obtaining and studying reliable RF discharge characteristics in gas mixtures containing CO molecules. Development of 1-D numerical code for calculation of discharge structure.

Subtask 2.2. Preparing high frequency power supply (~80MHz, 250W), measuring system and additional electrical setup for the study of RF discharge in gas mixtures containing CO molecules. Calculations of discharge characteristics for typical gas laser mixtures and gas dynamic parameters.

Subtask 2.3. Experiments on RF discharge in transversal "slab" geometry with water cooled electrode system. Defining the conditions corresponding to maximal specific input power (SIP) at room temperature of gas mixture. Incorporation of vibrational kinetics model into the 1-D discharge code.

Subtask 2.4. Experimental measurements of impedance and maximal SIP depending on mixture content, gas pressure and electrode spacing. Comparison of the experimental data with calculated properties of RF discharge.

Task 3. Experimental study and theoretical analysis of IR radiation absorption coefficients for different organic and non-organic substances near the wavelengths corresponding to FO CO laser spectrum lines. Preliminary research on potential using the FO CO laser as an instrument for the purposes of the atmospheric spectroscopy.

Subtask 3.1. Preparing the low and high pressure gas cells and acousto-optical detecting system to measure the absorption coefficients in gas mixtures containing usual and organic compounds.

Subtask 3.2. Testing experiments on single line FO CO laser radiation absorption in gases and saturated vapors. Measurements of multiline FO CO laser radiation absorption in different substances.

Subtask 3.3. Analysis of absorption spectra for different organic and inorganic substances, selection of intense absorption lines coinciding with FO CO laser lines, measurements of absorption coefficients on selected wavelengths. Testing of acousto-optical detecting system.

Subtask 3.4. Computer simulation of intense multifrequency FO CO laser radiation propagation in the atmosphere. Estimation of possible using FO CO laser for detecting different kinds of IR radiation attenuation during its propagation through atmosphere.

According to the above tasks the Final Report consists of three parts.

Part I. Theoretical and experimental study of FO CO laser gain kinetics and spectrum formation

Introduction

A first-overtone (FO) CO laser (Bergman et al., 1977; Basov et al., 1978) is an efficient source of multiwavelength IR radiation within the spectral range of 2.5 - 4.1 μm (Basov et al., 1999a, 2000a,b). Frequency tunable pulsed single-line FO CO lasing was obtained on more than 400 spectral lines within spectral range of 2.7 - 4.2 μm (Basov et al., 2000a,c, d) The spectral range of FO CO laser covers that of well-known HF- and DF-lasers, ro-vibrational line spacing being several times less than that of those lasers. FO CO laser spectral lines coincide with a lot of absorption lines of numerous organic and inorganic substances (see Part III). FO CO laser running on these wavelengths can be successfully used for resonance influence upon various media in nonlinear spectroscopy, remote sensing, laser chemistry, etc. Long wavelength-range spectrum of the FO CO laser corresponding to highly excited two-quantum vibrational transitions $V+2 \rightarrow V$ from $20 \rightarrow 18$ up to $38 \rightarrow 36$ coincides with atmospheric "transparency window" between ~ 3 and $\sim 4 \mu\text{m}$. The very opportunity of FO CO lasing on such high transitions is due to the fact that Einstein coefficient $A_{V+2,V}$ for a FO transition $V+2 \rightarrow V$ depends on the number of vibrational level V , the ratio $A_{V+2,V} / A_{V+1,V}$ increasing with the number V and even being higher than 1 for highly excited CO molecule transitions (Sobolev & Sokovikov, 1971; Rockwood et al., 1973; Ionin et al., 1998b). Therefore FO CO laser small-signal gain (SSG) for such transitions can be comparable with that of fundamental band laser. Single-line FO CO laser SSG was measured in (Basov et al., 2000c) for the first time, its maximum value coming up to 0.35 m^{-1} . The objective of this part is experimental and theoretical study of FO CO laser gain kinetics and effects responsible for spectrum formation of the FO CO laser operating on highly excited vibrational transitions. The information about SSG temporal behavior is extremely important for both further development of theoretical model of the FO CO laser operating on high vibrational transitions (Ionin et al., 2000a) and designing FO CO laser devices running even in CW mode of operation (McCord et al., 2000).

1.1. Re-examination of data for MQE model of CO overtone laser

It was demonstrated earlier (Ionin et al, 1999; Ionin et al 2000a) that for the correct description of a FO CO laser it is necessary to employ Multi-Quantum Exchange (MQE) theory. The set of kinetic constants accepted in the first version of the model (Ionin et al, 1999) for different gas temperatures, vibrational level numbers and number of exchanged vibrational quanta from 1 to 4 was collected using a special procedure based on published data of semi-classical calculations (Cacciatore et al, 1981; Billing et al, 1983). It should be noted that published data were incomplete. Therefore, interpolation and extrapolation procedures were performed to set the model into workable form.

No information was available about multi-quantum vibrational exchange processes between CO and N₂ molecules. Recent experimental results show the necessity of new kinetic information about energy transfer processes with highly excited CO molecules. It was found (Basov et al, 2000a) that the influence of small additions of N₂ into the CO:He active medium on the spectral characteristics of the FO CO laser for transitions with $\lambda > 3.8 \mu\text{m}$ is rather strong. This phenomenon could be explained by quasi-resonance Vibration-Vibration (VV) exchange processes CO(v)+N₂(0) \rightarrow CO(v-2)+N₂(1) and the need in the corresponding rate constants stimulated this study.

Meantime, a progress in knowing molecular and collision parameters results in more accurate data allowing for better description of VV exchange processes, in particular for high lying levels. We have

contacted leaders of two scientific groups most actively working in this field: Professors G. Billing (Denmark) and M. Cacciatore (Italy). Professor Billing gave a commission to his colleague C. Coletti to perform new calculations for VV exchange processes in pure CO requested by us. At present, these data, which were already published in (Coletti et al, 2000), are incorporated into our model. However, the published set of data is still incomplete and hence interpolated for unknown rate constants. To this moment, Dr. Coletti has provided us with much more complete set of rate constants. The process of incorporation of these new data allowing for formulation of the complete MQE model of the FO CO is in progress.

Professor Cacciatore suggested that our colleague Dr. Kurnosov come for two months to the University of Bari to do the work on modification of a numerical code aimed to simulate V-V exchange collisions between CO and N₂, to perform the necessary calculations. Dr. Kurnosov has visited Bari and the results of his research are also presented below.

1.1.1. Calculations of constants for processes CO(v)+N₂(0) → CO(v-2)+N₂(1)

Calculations of the rate constants have been carried out using the time-dependent coupled state semiclassical method (Billing, 1984). According to this method, the vibrational motion of the two colliding molecules is described quantum-mechanically, while the nuclear motion for the translational motion and molecular rotations is treated classically by solving corresponding classical equations of motion of two rigid rotors in the field of effective potential V_{eff} (see details in (Billing, 1984)). New potential surface was chosen. We constructed the CO-N₂ potential as a sum of short-range repulsive potential with the long-range multipole interaction. The site-to-site approach for determination of short-range (Ling et al, 1984) and Van-der-Waals part of intermolecular potential energy (Berns et al, 1980) was used. The factors in the CO quadrupole moment expansion were taken from (Billingsley et al, 1974), while the quadrupole moment components of N₂ were scaled values of (Reuter et al, 1986) to obtain agreement with the average value Q=-1.52E (1E=10⁻²⁶esu cm²) recommended by Buckingham (Cacciatore, 2000). The last data about dipole moment function (DMF) of CO molecule were taken from (Langhoff et al, 1995). But this DMF was not analytical, and the best 4th order expansion was found by us for usage in calculations. We compare in Fig.1.1 the dipole moment functions from (Yong et al, 1966) (used in the previous publications (Cacciatore et al, 1981; Billing, 1980)) and from (Chackerian et al, 1980) with our analytical fit of Langhoff data (Langhoff et al, 1995). Compared to the previously used data (Yong et al, 1966) the Langhoff DMF exhibits a maximum at larger bond length of CO. The different behaviour of the DMF in the asymptotic bond distance region can have an impact on the relaxation of the highly vibrationally excited CO molecules.

Table 1.1. Experimental and theoretically calculated rate constants [cm³/s] for the process CO(1)+N₂(0)
→ CO(0)+ N₂(1)

	T=100	T=150	T=200	T=250	T=300
a)	3.53E-15	5.66E-15	8.50E-15	1.16E-14	1.47E-14
b)	4.1E-15	5.9E-15	8.6E-15	1.2E-14	1.4E-14
c)	5.3E-15	6.4E-15	7.8E-15	9.3E-15	1.1E-14
d)	1.4E-15	2.2E-15	3.3E-15	4.6E-15	0.62E-14
e)	2.3E-15	3.9E-15	6.0E-15	8.6E-15	1.2E-14

a) results of our calculations; b)experimental results of (Allen et al, 1980);

c), d), e)-data of (Billing, 1980), obtained for different potential surfaces.

The basic test of the computer code for N₂-CO collisions was to calculate rate constants for the process N₂(0)+CO(1)→N₂(1)+CO(0). It was done and the corresponding rate constants for this process obtained in our calculations for temperature range 90÷300 K are presented in Fig. 1.2.

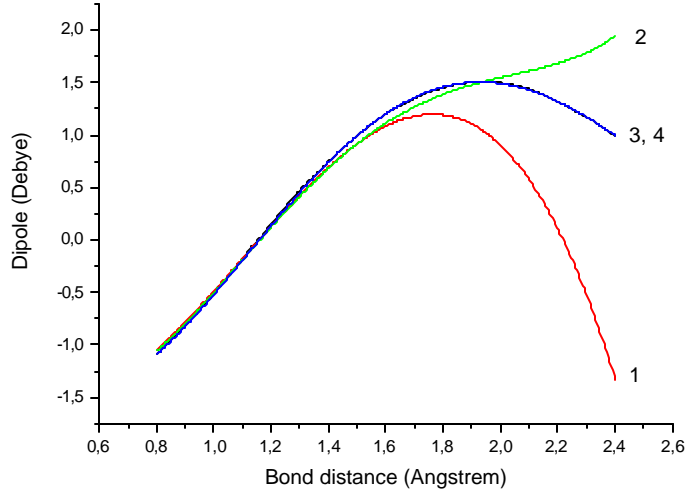


Fig. 1.1. Electric dipole moment function for the CO molecule in the ground electronic state;
1, 2 – empirical DMF from (Yong et al, 1966) and (Chackerian et al, 1980);
3, 4 - theoretical DMF from (Langhoff et al, 1995) and our 4th order fit.

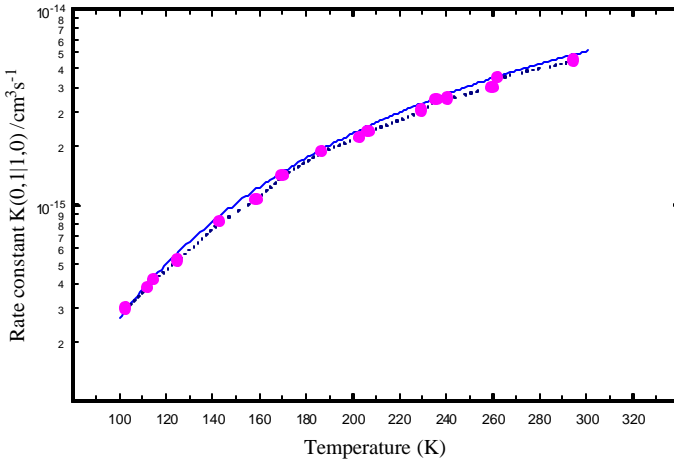


Fig. 1.2. Experimental and calculated ab initio semi-classical rate constants for process N₂(v=0) + CO(v=1)→ N₂(v=1) +CO(v=0). Points show experimental data from (Allen et al, 1980).

The agreement of our results with the experiment is rather good. In Table 1.1 we compare also our results for T=100, 150, 200, 250, 300 K with the rate constants calculated in the work (Billing, 1980) for three different potential surfaces and experiment (see Table 3 in the cited paper). One can see the better agreement of our results with experiment at T≤ 300 K, and probably this is a result of more adequate potential surface used by us.

The results of the quasi-classical calculations for near-resonance asymmetric processes CO(v)+N₂(0) → CO(v-2)+ N₂(1) are presented in Table 1.2 for T=100 and 500 K. The corresponding rate constant values are quite sizeable and reach the values up to 4·10⁻¹³ cm³s⁻¹. The role of such processes

in vibrational kinetics of highly excited CO molecules may be very important (analogous to processes $\text{CO}(v)+\text{CO}(0)\rightarrow\text{CO}(v-2)+\text{CO}(1)$ (Coletti et al, 2000; Dem'yanov et al, 1980)).

Table 1.2. Rate constants [cm³/s] for processes CO(v)+N₂(0)→CO(v-2)+N₂(1)

v	ΔE(cm ⁻¹)	T=100	T=500
33	348.443	4.031E-16	8.525E-15
34	299.445	9.492E-16	1.470E-14
35	250.573	2.314E-15	2.902E-14
36	201.827	6.118E-15	4.860E-14
37	153.207	2.051E-14	8.315E-14
38	104.713	8.905E-14	1.193E-13
39	56.346	2.252E-13	1.566E-13
40	8.104	4.323E-13	1.837E-13
41	-40.011	1.549E-13	1.605E-13
42	-88.000	4.849E-14	1.288E-13
43	-135.863	7.387E-15	9.441E-14
45	-231.211	2.529E-16	3.457E-14
47	-326.054	1.566E-17	1.137E-14

It can be demonstrated by comparison of characteristic VV-relaxation time values $\tau_{vv}(v)$ calculated in (Ionin et al, 2000a) and corresponding values of $\tau_{vv}(v)$ evaluated for near-resonance processes CO(v)+N₂(0) → CO(v-2)+ N₂(1) in conditions typical for FO CO laser ($[N_2] \geq 10^{18} \text{ cm}^{-3}$). The role of discussed processes in the mixtures CO:N₂ may be even greater than the role of processes CO(v)+CO(0)→CO(v-2)+CO(1) (Coletti et al, 2000) because they exert strong influence at lower levels. It is important for understanding situation with competition of VV and VT processes at high vibrational levels.

The calculations performed for analogous asymmetric processes CO(v)+N₂(0)→CO(v-3) +N₂(2) led us to near-resonance rate constants values less than $2.5 \cdot 10^{-17} \text{ cm}^3 \text{s}^{-1}$ and consequently their role is negligible.

It can be concluded that the renovation of potential surface for CO-N₂ intermolecular interaction led to better agreement with available rate constant values for process N₂(1)+CO(0)→ N₂(0)+CO(1) at low temperatures.

1.1.2. Incorporation of new kinetic and spectral constants into the full kinetic model of the first overtone CO laser

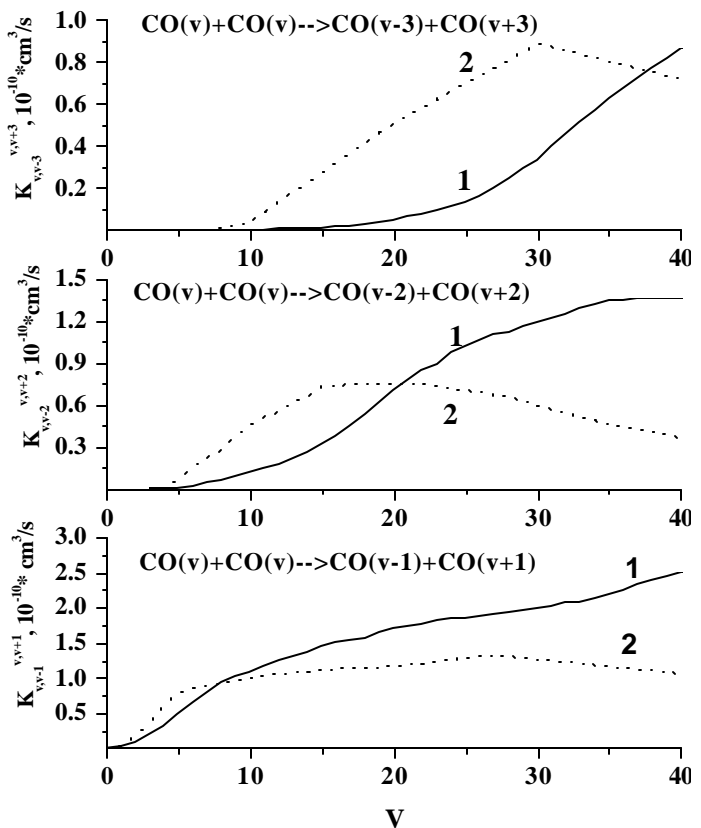


Fig. 1.3. Dependences of rate constants for quasi-resonant VV exchange on the vibrational number at 100 K. 1- extrapolated and interpolated data of (Coletti et all, 2000), 2-data of (Ionin et al, 2000)

We have modified the MQE model by incorporation new kinetic data, obtained from Prof. G. Billing and Dr. C. Coletti (nowadays these data are published in (Coletti et al, 2000)). The corresponding values of multi-quantum V-V-exchange rate constants calculated using the latest information about interaction potentials (Coletti et al, 2000) differ remarkably from those previously published in (Cacciatore et al, 1981; Billing et al, 1983). One-, two- and three-quantum processes rate constants were modified, and four-quantum processes were excluded from the model, since their new values were found to be approximately 30 times lower than adopted earlier. The full matrix of rate constants for T=100, 200, 300 K and for intermediate temperatures were determined using interpolation and extrapolation procedures described in (Ionin et al, 1999, 2000a, 2001a). In Fig. 1.3 we compare the old (Ionin et al, 2000a, 2001a) and new (Coletti et al, 2000) values of rate constants for quasi-resonant single-, double- and three-quantum V-V-exchange taken for T=100 K.

The paper (Coletti et al, 2000) contains also new data on asymmetric two-to-one quanta V-V-exchange processes: $\text{CO}(v)+\text{CO}(0)\rightarrow\text{CO}(v-2)+\text{CO}(1)$, and corresponding rate constant values are rather high (see Fig. 1.4). These asymmetric processes were also included into the model. Simultaneously, the Einstein coefficients for spontaneous emission for fundamental, first – and second overtone bands and V-T-rate constants were revised and corrected using the latest published data. The “new” values of spontaneous emission coefficients for fundamental and first overtone bands taken from (Langhoff et al, 1995) and corresponding “old” values (Ionin et al, 1998b) are presented in Fig. 1.5.

The revision of V-T rate constants was made taking into account theoretical and experimental results published in (Cacciatore et al, 1983; Reid et al, 1995, 1997). In particular, in (Cacciatore et al, 1983) the dependencies of the V-T relaxation rate constants on the number of the vibration level of CO molecule were found with usage of quasi-classical trajectory calculations. Comparing dependence of V-T rate constants calculated in (Cacciatore et al, 1983) on the vibrational number with formulas of modified SSH-theory (Smith et al, 1976), faster growth was revealed for high vibrational levels ($v>30$) in SSH-theory. Most reliable experimental data on of V-T relaxation rate constants for the process $? ?(v=1)+? ?\rightarrow? ?(v=0)+??$ were published in (Reid et al, 1995, 1997) . The experimental results (Reid et al, 1995, 1997) gave the values of these constants several times lower than reported previously (Allen et al, 1979) in the temperature range of 100-200 K. Therefore, we use the latest experimental data on V-T relaxation rates for the lowest level and extrapolate values of rate constants as a function of V according to the correlations calculated in (Cacciatore et al, 1983). An effect produced by modifications of VT relaxation

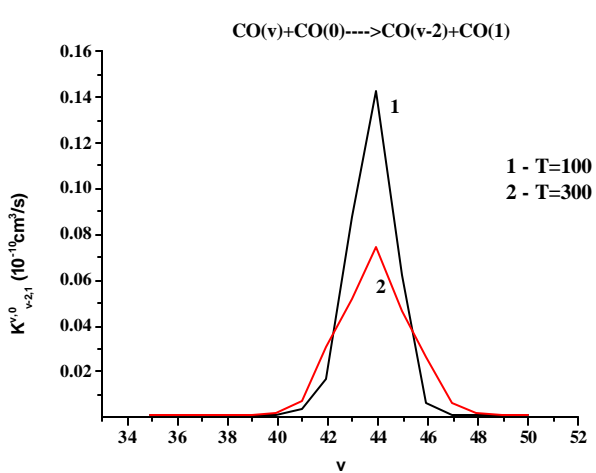


Fig. 1.4. Rate constants of asymmetric one-to-two quanta exchange vs vibrational number

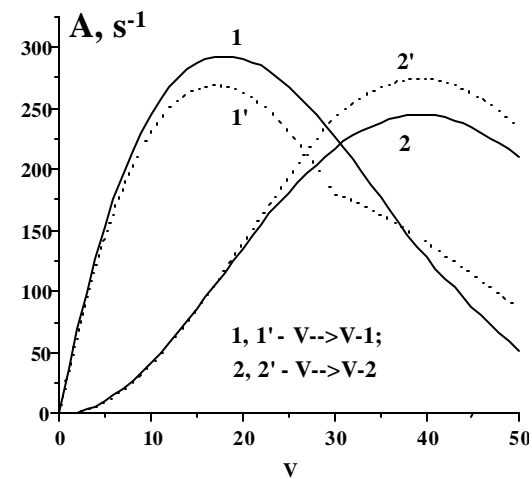


Fig. 1.5. Einstein coefficients for fundamental and the first overtone bands: 1,2 – new data; 1', 2' – the data used earlier.

constants is illustrated in Fig. 1.6 demonstrating predicted small signal gain (SSG) time behavior for the transition $36 \rightarrow 34$.

Concluding, in the modified kinetic model of the FO CO laser a number of kinetic constants were replaced by more exact values becoming available recently: VV-multi-quantum exchange constants between CO molecules and between N_2 and CO molecules; Einstein coefficients for spontaneous emission (as a result, stimulated emission cross sections were also changed); VT-relaxation constants for CO-He collisions. All the listed modifications made our model more reliable and adequate to the reality.

1.1.3. Theoretical modeling of gain and laser characteristics of the FO CO laser

The modified model was applied for modeling SSG time behavior on the first overtone transitions

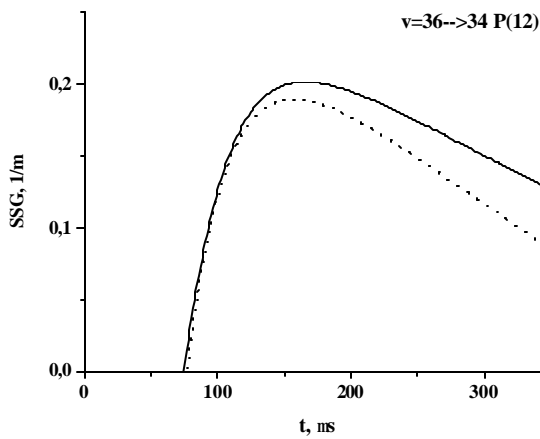


Fig.1.6. SSG time behavior calculated for $v=36 \rightarrow 34$ transition with two sets of V-T relaxation rates: solid line – new set: dotted line – old set.

with modified model are characterised by longer time delay, smaller gain amplitude and slower gain recession. The results calculated without taking into account asymmetric processes $CO(v)+CO(0) \rightarrow CO(v-2)+CO(1)$ are presented in Fig. 1.8, too. It is seen (curve 3) that exclusion of the asymmetric exchange processes results in an essential reduction of the maximum gain.

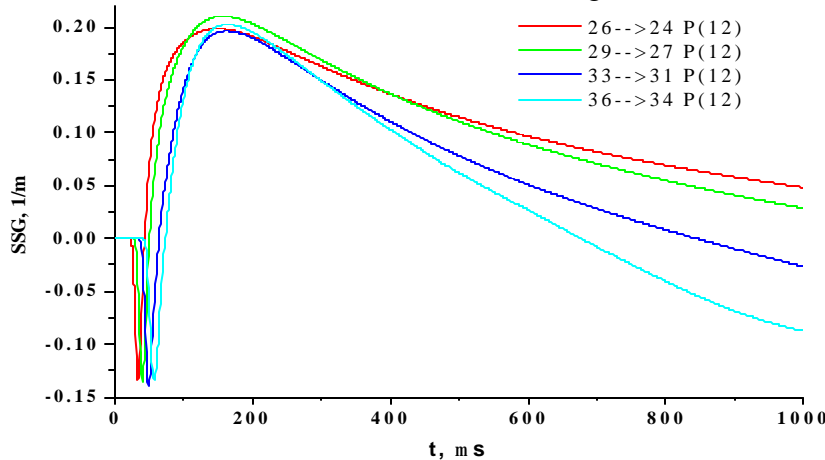


Fig. 1.7. SSG time behavior for the FO transitions.

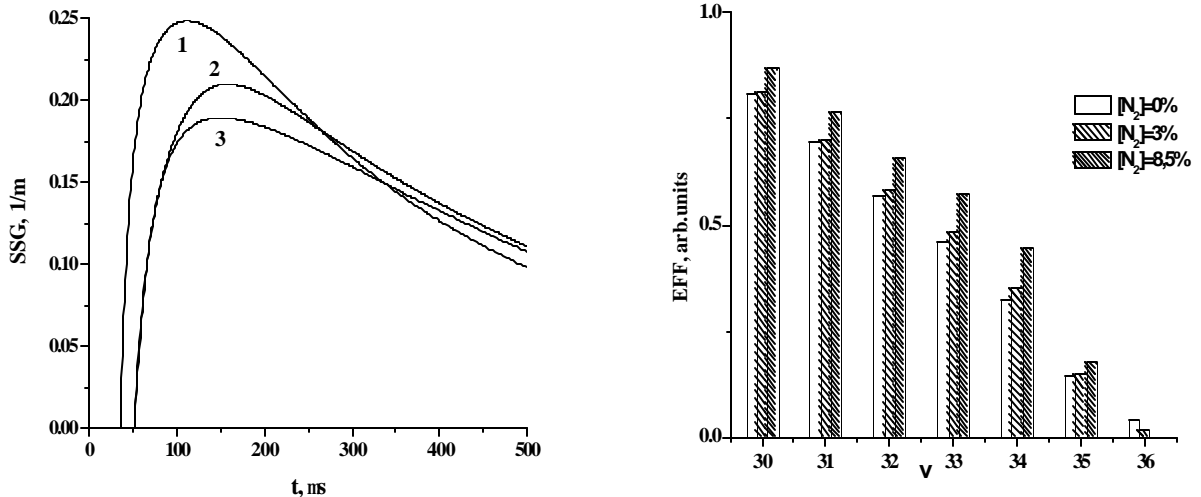


Fig. 1.8. Calculated SSG time behavior for the transition $v=29\rightarrow27$ P(12); 1 – the old version of MQE model; 2 – the modified MQE model; 3 – the asymmetric VV exchange ?? -?? was neglected

Generally, this agrees with the results of earlier studies (Dem'yanov et al, 1980) on the role of two-to-one-quantum vibrational exchange for CO molecules, made using constants calculated by SSH-theory. It is necessary to emphasize that the role played by two-to-one quantum VV exchange essentially depends on a magnitude of VT-relaxation rate constants used in the model, and this is explained by strong competition between two-to-one quanta V-V exchange and V-T relaxation processes on high vibrational levels.

As it was mentioned above, the influence of small additives of N_2 in $CO:He=1:4$ mixture on spectral characteristics of the first-overtone CO laser may be quite sizable. For analysis of these effects we applied the modified MQE model including the asymmetric processes $CO(v)+N_2(0)\rightarrow CO(v-2)+N_2(1)$. The results of such calculations made for experimentally realized conditions (see section 1.2) are given in Fig.

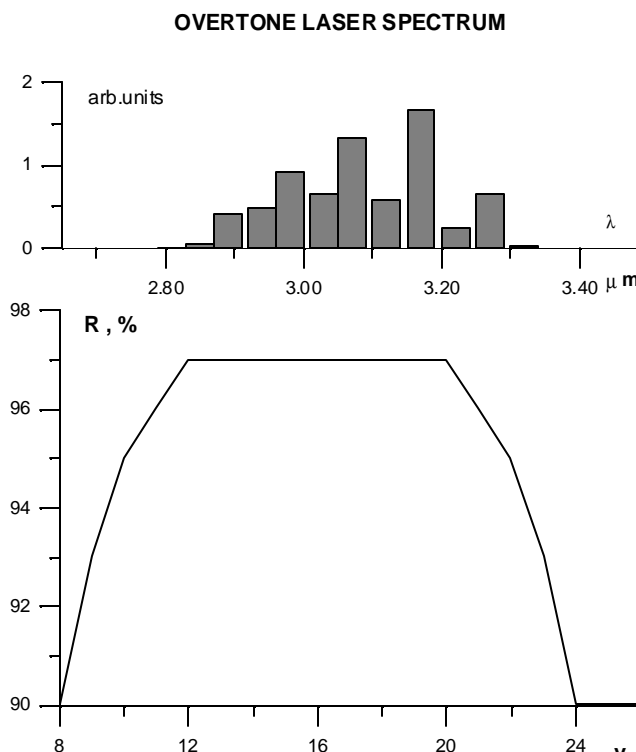


Fig. 1.10. The mirrors reflectance, used in calculations, and calculated output FB spectrum.

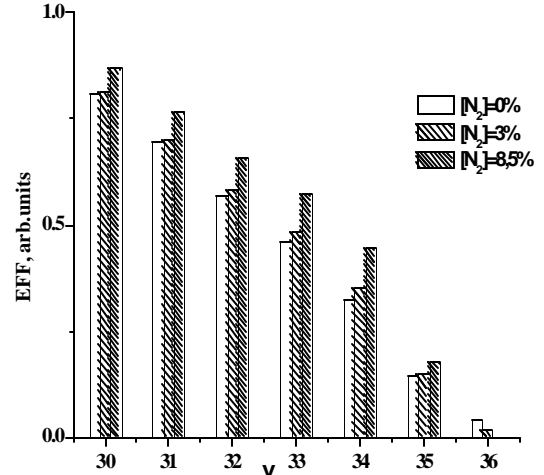


Fig. 1.9. Laser efficiency for large vibrational numbers v ($v+2\rightarrow v$) for three different mixtures

Fig. 1.10. The mirrors reflectance, used in calculations, and calculated output FB spectrum. The overtone laser spectrum calculated for $CO:He=1:4$ mixture relates rather well with experimentally observed spectrum. The decrease of intensity on extremely high vibrational transition $v=38\rightarrow36$ is caused by intercepting of significant fraction of

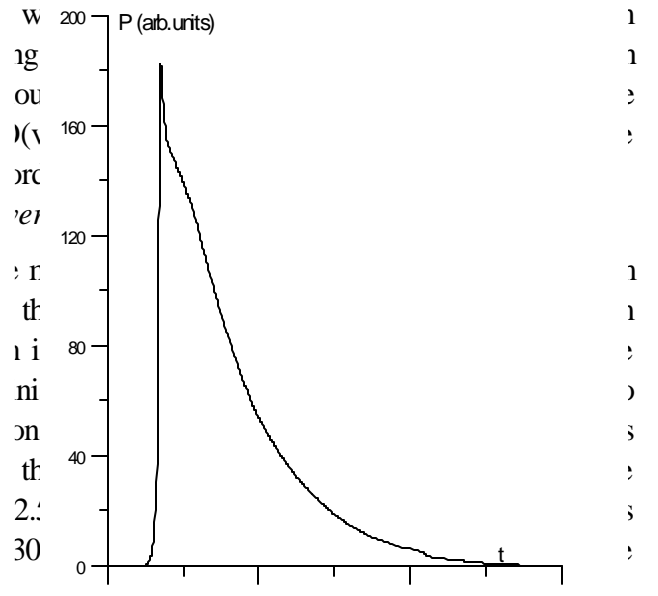


Fig. 1.11. The total intensity time dependence predicted for conditions of Ref. (Zeyfang et al,

with electric pulse duration $30 \mu\text{s}$ at initial reduced electric field strength $(E/N)_0 = 1.5 \cdot 10^{-16} \text{ V} \cdot \text{cm}^2$. Parameters of laser resonator are the following: the active medium length 110 cm ; the resonator is formed by two plane mirrors with reflectance R being a function of FO transitions from $v=12 \rightarrow 10$ up to $v=20 \rightarrow 18$ shown in Fig. 1.10; the passive losses per round trip 3% . The FB lasing was supposed to be totally suppressed.

The spectrum predicted numerically is presented in Fig. 1.10. The calculated spectrum exhibits clearly seen alternation of strong and weak vibrational bands, described earlier by us for cryogenic conditions (Basov et al, 2000a). Theoretically predicted FO CO laser efficiency for these conditions is 2.1% . The efficiency is in a reasonable agreement with efficiency experimentally obtained in (Zeyfang et al, 2000). Theoretically predicted laser pulse shape is shown in Fig. 1.11.

1.1.5. Analysis of cross sections for electron induced transitions between vibrational levels of N_2 and CO

To calculate the electron energy distribution function (EEDF) and kinetic coefficients associated with it, including electron energy balance, for CO laser excited mixtures, where a high percentage of molecules is vibrationally excited, it is necessary to account not only excitation of molecules but their de-excitation, too. In inelastic second-order collisions electrons gain energy of vibrational transition. Cross sections for excitation of molecules from the ground vibrational state were measured experimentally, and cross sections for reverse processes can be found using detailed balance principle. But correct description requires taking into account all the processes of excitation and de-excitation of molecules from an arbitrary vibrational level. Except transitions from the ground state, cross sections for such processes never were measured. They can be evaluated theoretically.

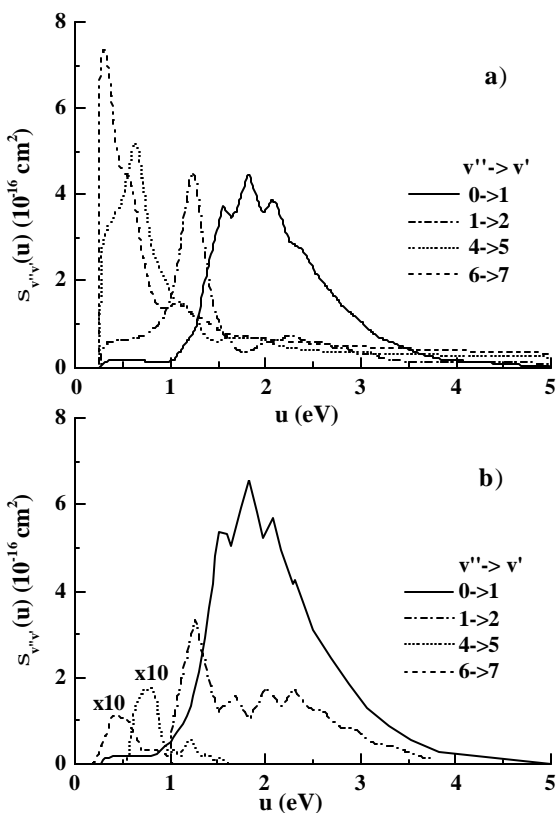


Fig. 1.12. Cross sections for excitation of ? ?

molecules from state v'' into state v' .

a) prepared in TRINITI. b) prepared in Bari

Earlier a set of cross sections for processes $\text{CO}(X^1\Sigma^+, v'') + e \rightarrow \text{CO}(X^1\Sigma^+, v') + e$ was calculated by us for $v''=1 \rightarrow 7 \rightarrow v'=2 \rightarrow 8$ using a semi-empirical methods (Chen, 1964; Alexandrov et al, 1979) proposed for calculations of cross sections for nitrogen molecules. Some of calculated cross sections are shown in Figs. 1.12-1.14. However, an accuracy of theoretical calculations is not known. Therefore, comparison between different sets of similar cross sections computed in different ways could be very helpful. We have performed such kind of comparison of our cross sections with that adopted in the laboratory of Professor Capitelli (the University of Bari, Italy). As it is seen from Figs. 1.12-1.14, the difference between cross sections is rather big, and in particular for electron-induced transitions between higher vibrational levels. Now it is impossible to say which of the sets is more reliable.

Sensitivity of laser characteristics to the particular complete set of cross sections is interesting to find out. One of such indirect characteristics is the electron energy balance. We calculated the electron energy balance solving the electron Boltzmann equation for the spherically symmetric part of the EEDF. Calculations were made for the gas mixture CO:N₂=1:9. The CO VDF was taken from the analytical theory (Dem'yanov et al, 1981). Namely, the VDF for levels lower than the so-called Treanor number was taken in a form of Treanor function, and for higher levels it has a form: $f_v = \frac{c}{v+1}$. The constant c was found from continuity condition for the VDF at the Treanor number. Nitrogen molecules distribution over vibrational levels was assumed to be Boltzmann distribution with the vibrational temperature satisfying an equation:

$$\frac{E_{1CO}}{T_{vCO}} - \frac{E_{1N_2}}{T_{vN_2}} = \frac{E_{1CO} - E_{1N_2}}{T}.$$

Here E_{1CO} , E_{1N_2} are the energies of the first vibrational levels of CO and N₂, respectively; T_{vCO} , T_{vN_2} are correspondent vibrational temperatures (for CO this is Treanor temperature); T is the gas temperature.

Figs. 1.15 and 1.16 show discharge power fractions going to excitation of CO and N₂ molecules in dependence on the CO vibrational temperature at the fixed reduced electric field strength, E/N . It is seen how with growth of vibrational temperature (Fig. 1.15) more and more fraction goes to excitation of nitrogen molecules. This is due to more intense heating of electrons in second kind collisions which increases their average energy. Note that maximum of cross sections for excitation of nitrogen lies at 2.3 eV, while for CO molecules it is located at 1.9 eV. For the CO vibrational temperature higher than 3000 K the fraction going to CO molecular vibrations becomes negative. It means that effectively electrons participate in the process of energy transfer from CO to N₂. For higher value of E/N parameter (Fig. 1.16) the rate of electron heating by electric field increased. As a result, the fraction of power going to CO vibrations is positive for all the range of vibrational temperatures examined. It is rather strange, but the difference in energy balance distortions induced by high vibrational excitation degree when using two sets of cross sections (TRINITI and Bari) is insignificant.

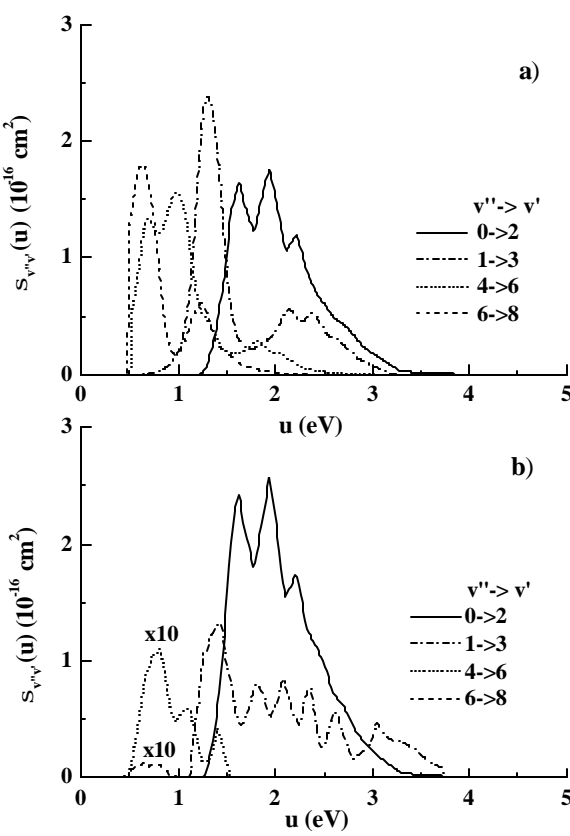


Fig. 1.13. Cross sections for excitation of CO molecules from state v'' into state $v' = v'' + 2$.
a) prepared in TRINITI, b) prepared in Bari

Excitation of CO molecular vibration by electron impact in the range of vibration quantum numbers $v'' \geq 10$ proceeds in non-resonant cascade processes. Cross sections for non-resonant excitation in Born approximation were determined analytically in the following formula (Takayanagi, 1966):

$$Q_{v+m,v}(u) = Q_{v,m} f(u/E_{v,m}) \quad (1.1)$$

where

$$f(x) = \frac{1}{x} \ln \left(\frac{\sqrt{x} + \sqrt{x-1}}{\sqrt{x} - \sqrt{x-1}} \right) \quad (1.2)$$

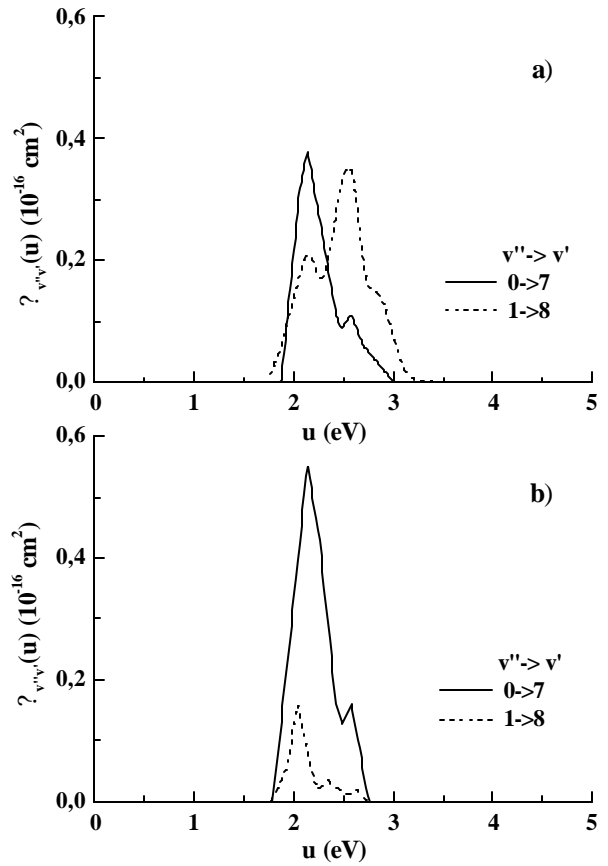


Fig. 1.14. Cross sections for excitation of CO molecules from state v'' into state $v' = v'' + 7$.
a) prepared in TRINITI, b) prepared in Bari

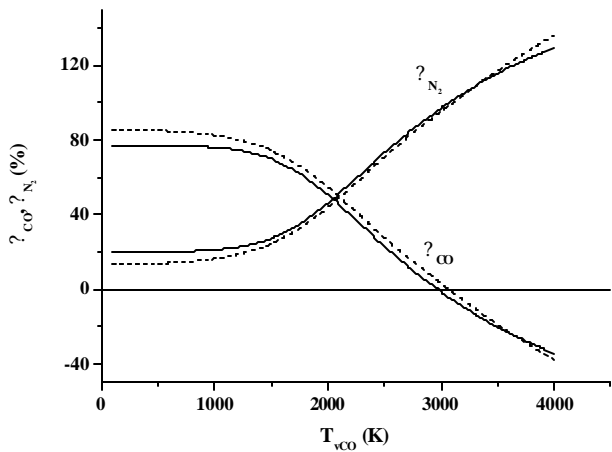


Fig. 1.15. Discharge power fractions going to excitation of ?? and N_2 molecules. ?? : $\text{N}_2 = 1:9$, $E/N = 1 \cdot 10^{-16} \text{ V cm}^2$, $T = 100 \text{ K}$. Solid line for cross section set of TRINITI, dashed line for cross section set of Bari

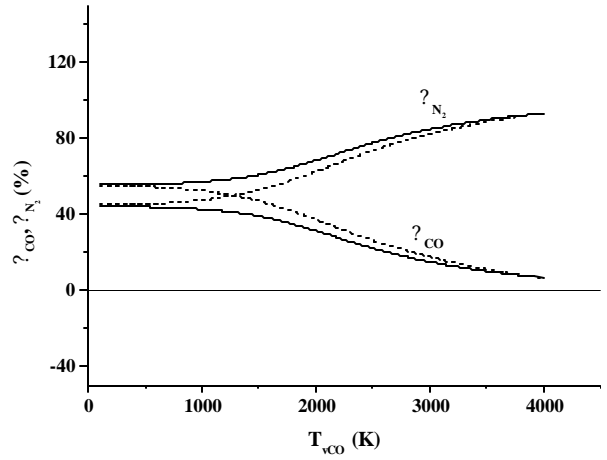


Fig. 1.16. Discharge power fractions going to excitation of ?? and N_2 molecules. ?? : $\text{N}_2 = 1:9$, $E/N = 3 \cdot 10^{-16} \text{ V cm}^2$, $T = 100 \text{ K}$. Solid line for cross section set of TRINITI, dashed line for cross section set of Bari

Here u is electron energy, $E_{v,m}$ – energy of excited transition, m is the number of excited quanta. Values of parameters $Q_{v,m}$ may be obtained using relations between energies and dipole matrix elements $\mathbf{m}_{v,m}$ of transitions

$$Q_{v,m} = Q \frac{E_{0,1}}{E_{n,m}} \frac{\mathbf{m}_{v,m}^2}{\mathbf{m}_{0,1}^2} = Q \left(\frac{E_{0,1}}{E_{n,m}} \right)^4 \frac{A_{v,m}}{A_{0,1}} \quad (1.3)$$

where $A_{v,m}$ are spontaneous radiation probabilities for transitions $v+m \rightarrow v$, $Q=0.2 \cdot 10^{-16} \text{ cm}^2$ (Hake et al, 1967). Parameters $Q_{v,m}$ for excitation of several single- and two-quantum transitions are presented in Table 1.3. One can see that non-resonant excitation cross sections are of the same order of magnitude as resonance excitation cross sections in the range of $v < 10$. Cross sections for three- and four-quantum excitation are small.

Table 1.3. Energies of transitions and cross sections parameters of single- and two-quantum excitation of CO molecule vibration by electron impact.

V	$E_{v+1,v}$, eV	$E_{v+2,v}$, eV	$Q_{v,1}, 10^{-16} \text{ cm}^2$	$Q_{v,2}, 10^{-16} \text{ cm}^2$
10	0.232	0.461	2.4	-
15	0.216	0.428	3.7	-
20	0.199	0.395	4.9	0.2
25	0.182	0.361	5.9	0.4
30	0.166	0.328	7.0	0.6
35	0.149	0.294	9.5	1.1
40	0.132	0.261	13.0	1.7
45	0.116	0.228	17.9	2.8

Cross sections for electron impact vibration de-excitation should be obtained using detailed balance principle. Fig. 1.17 shows cross sections of single- and two-quantum excitation for several vibration transitions in CO. Large cross sections and high effective vibration temperatures relating to high v numbers in strongly non-equilibrium conditions may result in considerable redistribution of relative electron energy fractions. Figs. 1.18-1.19 show the results of calculations of electron energy fractions in vibrationally

excited CO. CO vibration population distribution function supposed to be just the same as above in calculations of electron energy fractions in CO:N_2 mixtures, CO vibration temperature $T_{v\text{CO}}=3000 \text{ K}$, $T=150 \text{ K}$. Treanor number is $v_?=4$ for this case. Fig. 1.18 shows relative fractions of electron energy flowing to molecule excitation in the group of vibration levels lower (1) and higher (2) Treanor v number.

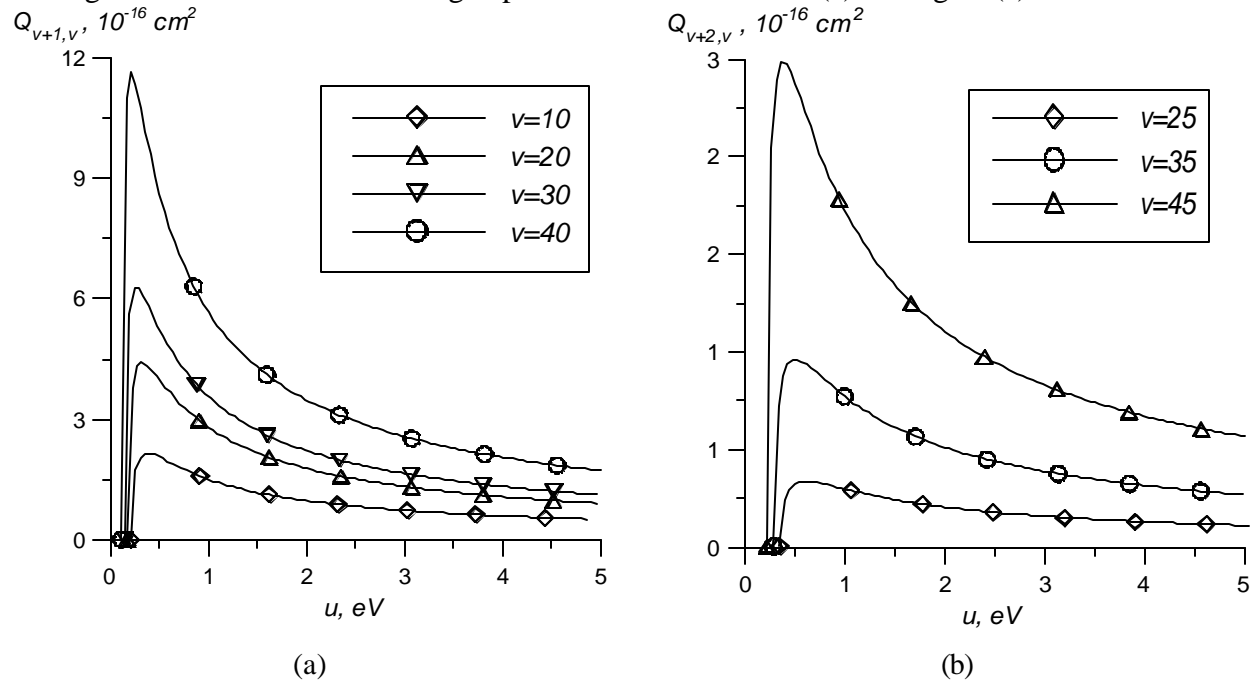


Fig. 1.17. Cross sections of electron non-resonant (?) – single-quantum and (b) – two-quantum excitation of CO molecule vibration.

Fig. 1.19 shows relative fractions of electron energy flowing to molecule excitation in the group of vibration levels $v \leq 8$ (1) where resonant excitation dominates and $v > 8$ (2) where cascade excitation proceeds. For low reduced field, energy flows from excited molecules to electrons. The higher v numbers the wider the range of reduced electric fields, in which energy flows from excited molecules to electrons.

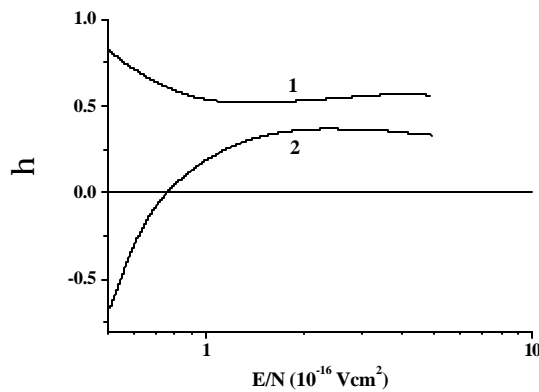


Fig. 1.18. Relative electron energy fractions η , excitation in the group of vibration CO levels lower (1) and higher (2) Treanor v number.

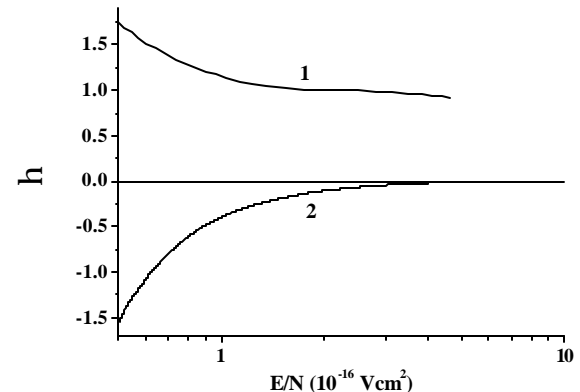


Fig. 1.19. Relative electron energy fractions η , excitation in the group of vibration levels $v \leq 8$ (1) and $v > 8$ (2).

1.1.6. Gain saturation effects in CO laser active medium

Gain saturation effect in lasers is usually described by saturation intensity I_s . In the case of homogeneous line broadening the dependence of laser gain k on radiation intensity I is well known (e.g. (Rigrod, 1963)):

$$k = \frac{k_0}{1 + I / I_s} \quad (1.4)$$

At $I=I_s$ gain decreases twice relative small signal gain k_0 , while induced transitions rate becomes equal to relaxation rate. Saturation intensity may be expressed by active media parameters – effective relaxation time constant of inverted population on laser transition $\tau^l = \tau_1^{-1} + \tau_2^{-1}$, $\tau_{1,2}$ – time constants of relaxation of lower and upper laser levels, laser photon quantum $h\nu$ and induced transitions cross section $s : I_s = h\nu / s\tau$.

It would be helpful to know saturation intensity for operation of CO laser as amplifier or oscillator on selected vibration-rotation line. However, CO laser being a multi-level system cannot be described exactly in terms of simple saturation intensity, even if it is defined as a function of the vibrational number.

Partial inversion in CO laser forms for a range of high-lying levels populated in the course of quasi-resonant VV exchange. In such a case vibrational distribution function (VDF) acquires specific features (Treanor et al, 1968). It decreases rapidly in the range of a few lower levels (this range is called as Treanor region), then gradually transforms into a plateau, the region of slow decrease. Boundary vibration number between these two regions is called as Treanor number v_T . In plateau region partially inverted population on rotation-vibration transitions occurs. Populations of levels in plateau region depend essentially on frequencies of VV exchange processes. Besides, they depend on pumping power density and gas temperature. As a result, gain saturation effect in CO laser active media has an important peculiarity – it depends not only on active media parameters but also on pumping power density and gas temperature.

In the simplest kinetic model of CO laser, only single-quantum VV exchange (SQE) processes are considered (Gordietz et al, 1980). Analytical theory of CO laser was developed (Napartovich et al, 1977) considering only resonant VV exchange processes in non-linear vibration level diffusion equation. In the frame of this analytical theory estimation of saturation intensity on selected $v @ v - 1$ transition was obtained:

$$I_{sv} \sim \frac{h\nu_v}{s_v} \frac{8\Delta E}{T d_{vv}^3} v v_T Q_{10} N_{CO} c \quad (1.5)$$

In formula (1.5) N_{CO} is CO molecule density, Q_{10} the lowest transition VV exchange rate constant, ΔE molecular anharmonism energy, d_{vv} reciprocal VV exchange radius, c numerical coefficient. Factor, following the parameter $h\nu_v / s_v$, may be considered as an effective rate of VV exchange. Numerical value of c means Treanor minimum population (and thus characteristic population of levels in the range of plateau) relative to the ground state population:

$$c = f_0 \exp[-\Delta E(v_T)^2 / T - 1/2] \quad (1.6)$$

$v_T = (E_1/2\Delta E)(T/T_v) + 1/2$ is Treanor number, E_1 is energy of fundamental vibration quantum, T_v vibration temperature of the first vibrational level, f_0 relative population of ground state (it is assumed that the VDF is normalized to 1). Conservation of vibrational quanta in VV processes allows obtaining the relation between pumping power density W_p , vibration excitation power fraction h_v and c :

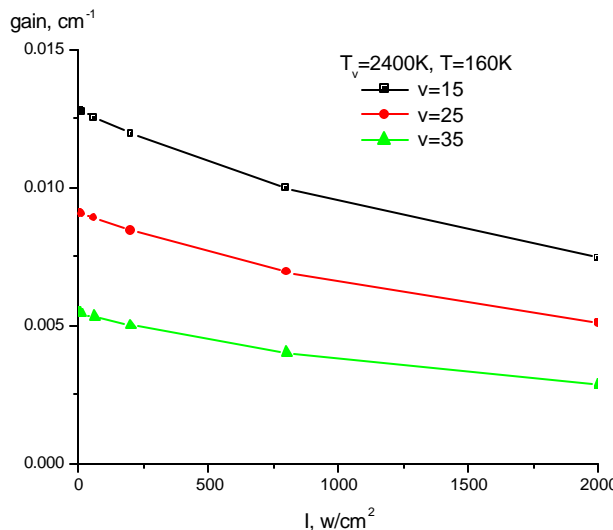


Fig. 1.20. Gain on selected CO $v \otimes v-1$ transitions as a function of radiation intensity.

$$\frac{W_p h_v}{E_1 N_{CO}} = \frac{4\Delta E v_T^2 Q_{10}}{T d_{vv}^3} c^2 \quad (1.7)$$

Equations (1.6) and (1.7) provide a relation between Treanor number and pumping power density. An analytical theory (Likalter, 1979) gave a solution to the problem to describe saturation for CO laser line selective operation. The following expression for saturation intensity was derived:

$$I_{sv} = \frac{\hbar n_v}{s_v} \frac{4}{d_{vv}^2} \sqrt{\frac{\Delta E}{T}} v v_T Q_{10} N_{CO} c \quad (1.8)$$

Equation (1.8) differs from evaluation (1.5) only by factor of the order of unity

$$\frac{2}{d_{vv}} \sqrt{\frac{\Delta E}{T}}$$

The results of the analytical theory illustrate explicitly the peculiarities of CO laser saturation effect. Realistic model of CO laser kinetics should consider multi-quantum VV exchange (MQE) (Konev et al, 1994; Ionin et al, 2000a). In this case, the analytical theory is hardly applicable, and we should rely on numerical calculations. It was found that effective relaxation time of the VDF, recovering after pulsed disturbance introduced for a selected vibrational transition, calculated with MQE model is several times longer than computed in the frame of SQE model (Ionin et al, 1998b), especially at high vibration levels. Saturation effects were studied in the following manner. CO laser MQE kinetic model was employed for conditions of constant vibrational and gas temperatures. Gain reduction induced by resonant radiation with frequency in the center of rotational line possessing maximum gain in the fundamental vibrational band was examined. Gain dependence on radiation intensity was numerically computed. A particular value of intensity was taken as saturation intensity, under which gain decreased twice relative to small signal gain. Fig.1.20 shows the examples of gain calculation on various selected transitions in dependence on radiation intensity. Such curves were used to calculate saturation intensities.

Figs. 1.21-1.23 show the results of calculation of saturation intensities for $v \otimes v-1$ transitions at various vibrational and gas temperatures in CO:He=1:4 mixture at total gas number density $N=0.12$ Amagat. Calculations show that saturation intensity weakly depends on vibration numbers v , and strongly increases for lower gas temperature and higher vibrational temperature.

Using correlations between stimulated emission cross sections and spontaneous emission Einstein coefficients $A_s \sim A / n^2$, one can obtain saturation intensities for the first overtone $v \otimes v-2$ transitions:

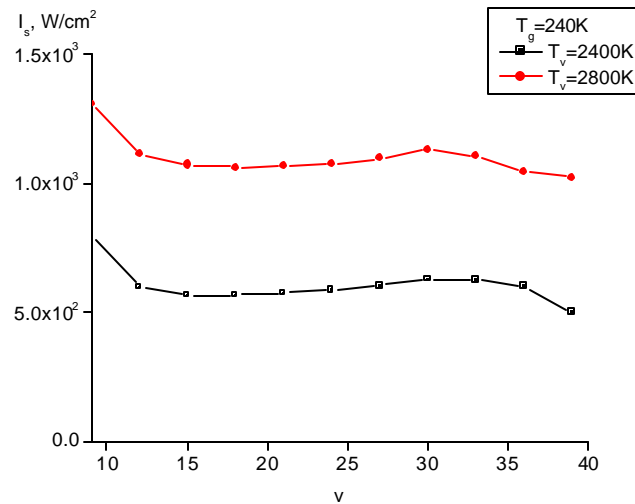


Fig. 1.21. Saturation intensities for CO molecule $v@v-1$ transitions for various vibration temperatures; $T=240\text{K}$

proceeds in Treanor range of vibrational quantum numbers, $v \ll v_T$, where SQE processes dominate. Thus, characteristic populations of levels in the range of plateau are approximately presented by formulas (1.6) and (1.7), which determine the order of magnitude of saturation intensities and their dependence on vibrational and gas temperatures. For pumping power growing with CO molecule number density $W_p \sim N_{CO}^2$, c is approximately constant according to (1.7). For collisional line broadening, $s_v \sim N^{-1}$, $I_{sv} \sim N^2$. Using this scaling and the results of calculations presented above one can evaluate saturation intensities at various molecular densities.

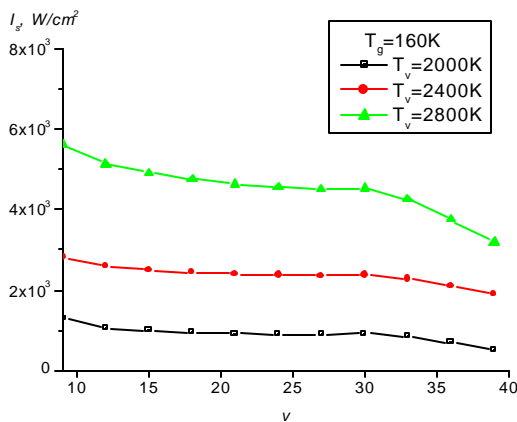


Fig. 1.22. Saturation intensities for $v@v-1$ transitions at various vibration temperatures; $T=160?$

$$I_{sv,v-2} = I_{sv,v-1} \left(\frac{\mathbf{n}_{v,v-2}}{\mathbf{n}_{v,v-1}} \right)^3 \frac{A_{v,v-1}}{A_{v,v-2}} \quad (1.9)$$

The results of calculations of first overtone saturation intensities from eqn. (1.9) are presented in Figs. 1.24-1.25. Let us note that multi-quantum VV exchange is quasi-resonant process. The number of levels coupled by collisions in MQE model exceeds that in SQE model, but still is much smaller than the plateau size. Multi-quantum VV exchange rate constants hardly can be correlated with resonant exchange rate constant at the lowest level. However, effective VV exchange frequency is still proportional to populations of plateau levels, $I_{sv} \sim h n_v N_{CO} c / s_v$. Plateau formation

$$I_{sv} \sim N^{-1}$$

proceeds in Treanor range of vibrational quantum numbers, $v \ll v_T$, where SQE processes dominate. Thus, characteristic populations of levels in the range of plateau are approximately presented by formulas (1.6) and (1.7), which determine the order of magnitude of saturation intensities and their dependence on vibrational and gas temperatures. For pumping power growing with CO molecule number density $W_p \sim N_{CO}^2$, c is approximately constant according to (1.7). For collisional line broadening, $s_v \sim N^{-1}$, $I_{sv} \sim N^2$. Using this scaling and the results of calculations presented above one can evaluate saturation intensities at various molecular densities.

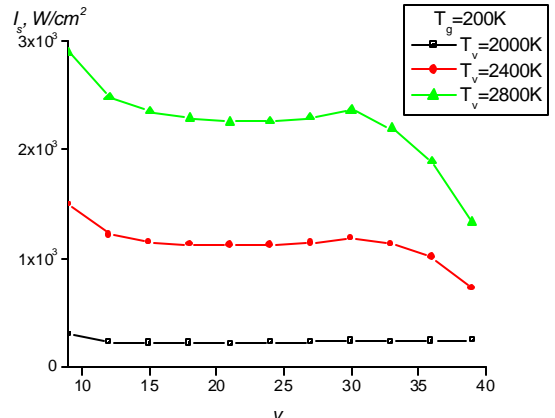


Fig. 1.23. Saturation intensities for $v@v-1$ transitions at various vibration temperatures; $T=200\text{K}$

It is worth to discuss applicability of the quantity ‘saturation intensity’ in conditions of pulsed CO laser. The specific feature of CO laser, particularly operated on the first overtone transitions, is that laser pulse is, as a rule, much longer than the discharge pulse. It is quite common, that the laser pulse develops after termination of the discharge. Nevertheless, in such a situation the saturation intensity has a clear physical meaning. It characterizes VV exchange processes causing formation of the plateau with long delay with respect to beginning of excitation. The intensity of these processes keeps a memory about pumping.

Generally, this memory is not described by relationships like (1.7). However, the level of the plateau (quantity c) can be connected with the SSG using the analytical theory for establishing VDF (Zhdanok et al, 1979). The relationship (1.6) holds by the order of magnitude allowing for estimation of the saturation intensity even for the pulsed excitation.

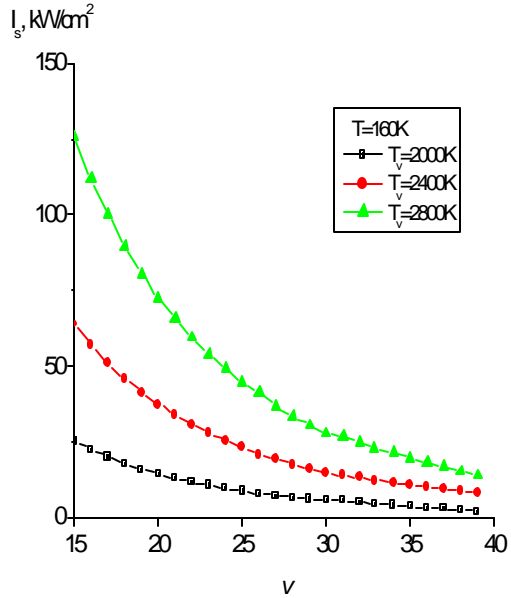


Fig. 1.24. Saturation intensities for $\nu @ \nu-2$ transitions at various vibration temperatures; $T=160K$

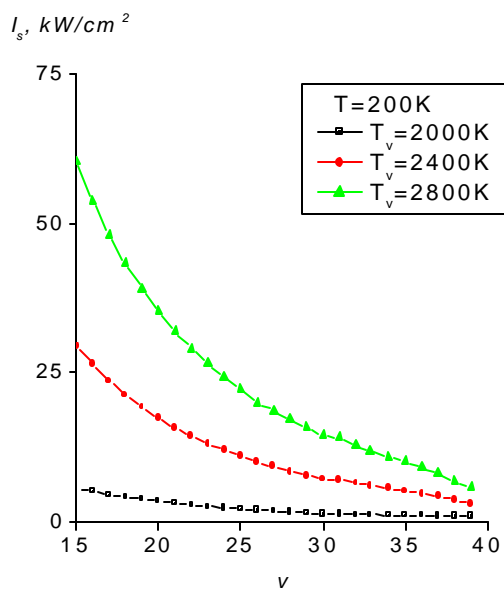


Fig. 1.25. Saturation intensities for $\nu @ \nu-2$ transitions at various vibration temperatures; $T=200K$

It is known that for sufficiently short laser pulse effect of gain saturation is described more adequately by the quantity ‘saturation energy’. Evidently, the measure of this saturation given generally by the quantity $1/\sigma$ (σ is the stimulated emission cross section dependent on vibrational and rotational numbers) holds for the CO laser, too. The criterion whether the laser pulse is short or not short gives comparison of laser pulse duration with characteristic relaxation time of the VDF. For CO laser such a characteristic relaxation time was discussed earlier in (Ionin et al, 2000a).

1.1.7. Conclusions

Transition to more correct description of VV exchange processes taking into account multi-quantum exchange results in a remarkable improvement of predictions. Further progress in development of the kinetic model of the FO CO laser was associated with modification of numerous kinetic constants entering into equations: 1) Einstein coefficients were changed according to the latest more accurate data; 2) VV exchange rate constants for CO-CO and CO-N₂ collisions were changed according to the last results of semi-classical calculations of these quantities; 3) VT relaxation constants for particularly important collisions of CO molecules on very high levels with He atoms were changed by combining the latest experimental data with most reliable theoretical results. The result is that at present our model enjoys much more confidence than earlier. However, this work is still not finished. The exploited by us latest published set of data on VV exchange between CO molecules is incomplete. As it was mentioned, the extrapolation procedure was used to evaluate missed data. Quite recently, in response to our request Dr. Coletti (the postgraduate student of Prof. Billing) has provided us with a complete set of the rate constants, excluding the necessity to do extrapolations. Inclusion of these data will complete modification of the kinetic model of the FO CO laser.

Nevertheless, comparison of calculations with FO gain measurements showed that modified model does not allow understanding of long gain build up observed in experiments. This problem is of key importance in design of supersonically cooled laser device. Further special efforts should be undertaken to realize the reasons of disagreement of model and gain measurements.

Concerning electron interactions with molecular vibrations, a large scatter in computed cross sections for collisions of vibrationally excited CO and N₂ molecules with electrons through the negative-ion resonance is observed. No criterion is found to make a choice of most reliable values of these cross sections. Surprisingly, modeling of the FO CO laser characteristics shows a weak sensitivity of them to the shape and magnitude of these cross sections. Further studies are necessary to achieve better understanding about resonant interaction of electrons with molecular vibrations. It was shown in section 1.1.5 that adequate description of electron interaction with highly excited molecules (so-called potential scattering) is very desirable and may introduce a remarkable correction into computed laser characteristics. It is worth to remind that this more detailed description of the electron-molecule interactions will result in more complex numerical code, which hardly can be used for modeling systems with spatial gradients.

1.2. Experimental study of FO CO laser gain and spectrum formation

1.2.1. Measurement of SSG build up and rise time

Detailed description of an experimental facility is given in (Basov et al., 2000a-c, Ionin et al., 1998b). Cryogenically cooled pulsed e-beam controlled discharge CO laser with active length of 1.2 m was used. Pump pulse length was $\sim 25 \mu\text{s}$. Specific input energy (SIE) was $\sim 200\text{-}400 \text{ J/l Amagat}$. Laser mixture $\text{CO:N}_2:\text{He}$ with different content of nitrogen and helium at gas temperature of $\sim 100 \text{ K}$ and gas density 0.18 Amagat was used. The optical scheme of the laser facility is presented in Fig.1.26. A laser resonator consisted of totally reflecting mirror 2 situated on a laser chamber 1 and diffraction grating 4 (200 grooves/mm; grating G3 in (Basov et al., 2000a,c,d) operating in a Littrow configuration and located at 0.4 m far from Brewster window 3. FO CO laser radiation was extracted through the zero diffraction order of the grating (5). FO CO laser SSG build up time and rise time were measured by changing intracavity optical losses. Output coupling determined by the grating 4 was 0.5-10% depending on a laser wavelength (Basov et al., 2000a,c,d). Controllable intracavity optical losses were determined by scattering and absorption of the grating and other optical elements, and additional optical losses, the latter being introduced by intracavity flat 6 made of CaF_2 . There was used a set of the flats for the strongest spectral lines. For instance, lasing on the strong spectral line $34 \rightarrow 32\text{P}(12)$ with the wavelength $3.84 \mu\text{m}$ still took place even at round-trip optical losses of 55% (three intracavity CaF_2 flats were inclined at the angle of $\sim 10^\circ$ to the optical axis of the laser resonator).

Changing the additional intracavity optical loss resulted in alteration of FO CO lasing delay time, which was considered as a time needed for SSG to get its threshold value. The latter was calculated using data on total optical losses including additional ones. The dependence of the threshold gain for different additional optical losses upon FO CO lasing delay time just reflects SSG time behavior, namely its build up and rise time.

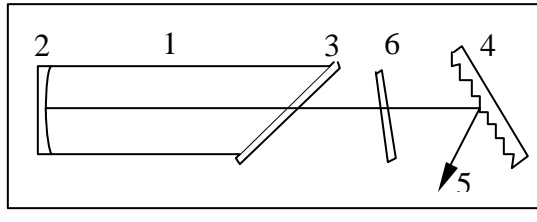


Fig.1.26. Optical scheme of the laser facility. 1-laser chamber, 2-totally reflecting mirror, 3-Brewster window, 4-diffraction grating, 5- laser output, 6- intracavity flat made of CaF_2

The SSG time behavior is presented in Fig.1.27, pump pulse switching on time being considered as a time reference point. SSG time behavior measurement was carried out for nitrogen free mixture $\text{CO:He}=1:4$ (SIE $\sim 320 \text{ J/l Amagat}$) and helium free mixture $\text{CO:N}_2=1:9$ (SIE $\sim 380 \text{ J/l Amagat}$). The experiments were carried out with frequency agile FO CO laser, which operated on a single spectral line P(12) belonging to the different vibrational transitions $20 \rightarrow 18$ ($\lambda=3.041 \mu\text{m}$), $26 \rightarrow 24$ ($\lambda=3.341 \mu\text{m}$), $29 \rightarrow 27$ ($\lambda=3.512 \mu\text{m}$), $33 \rightarrow 31$ ($\lambda=3.767 \mu\text{m}$) and $36 \rightarrow 34$ ($\lambda=3.982 \mu\text{m}$).

SSG build up time strongly depends on the vibrational transition number being $\sim 70 \mu\text{s}$ for the lower overtone transition $20 \rightarrow 18$ and comes up to $\sim 170 \mu\text{s}$ for the upper transition $36 \rightarrow 34$. The build up time was defined in the experiment as a time needed for SSG to reach the value of 0.05 m^{-1} (15-20% of its maximum value), i.e. as a time needed for SSG to get its positive value. If minimal measured value of SSG exceeded this value, linear extrapolation was used. Dependence of the build up time on the vibrational number of overtone transition $V+2 \rightarrow V$ for nitrogen-free and helium-free laser mixtures is presented in Fig. 1.28a (for $\text{CO:He}=1:4$ and $\text{CO:N}_2=1:9$ laser mixtures). Both the curves have approximately the same behavior, i.e. a time needed for SSG to be positive only slightly depends on nitrogen or helium fraction. It

should be noted that SSG build up time for highly excited overtone transitions is considerably higher than both pump pulse duration ($\sim 25 \mu\text{s}$) and SSG build up time for fundamental band transitions, which was estimated as ~ 30 - $50 \mu\text{s}$ by measuring time delay of fundamental band superradiance pulse.

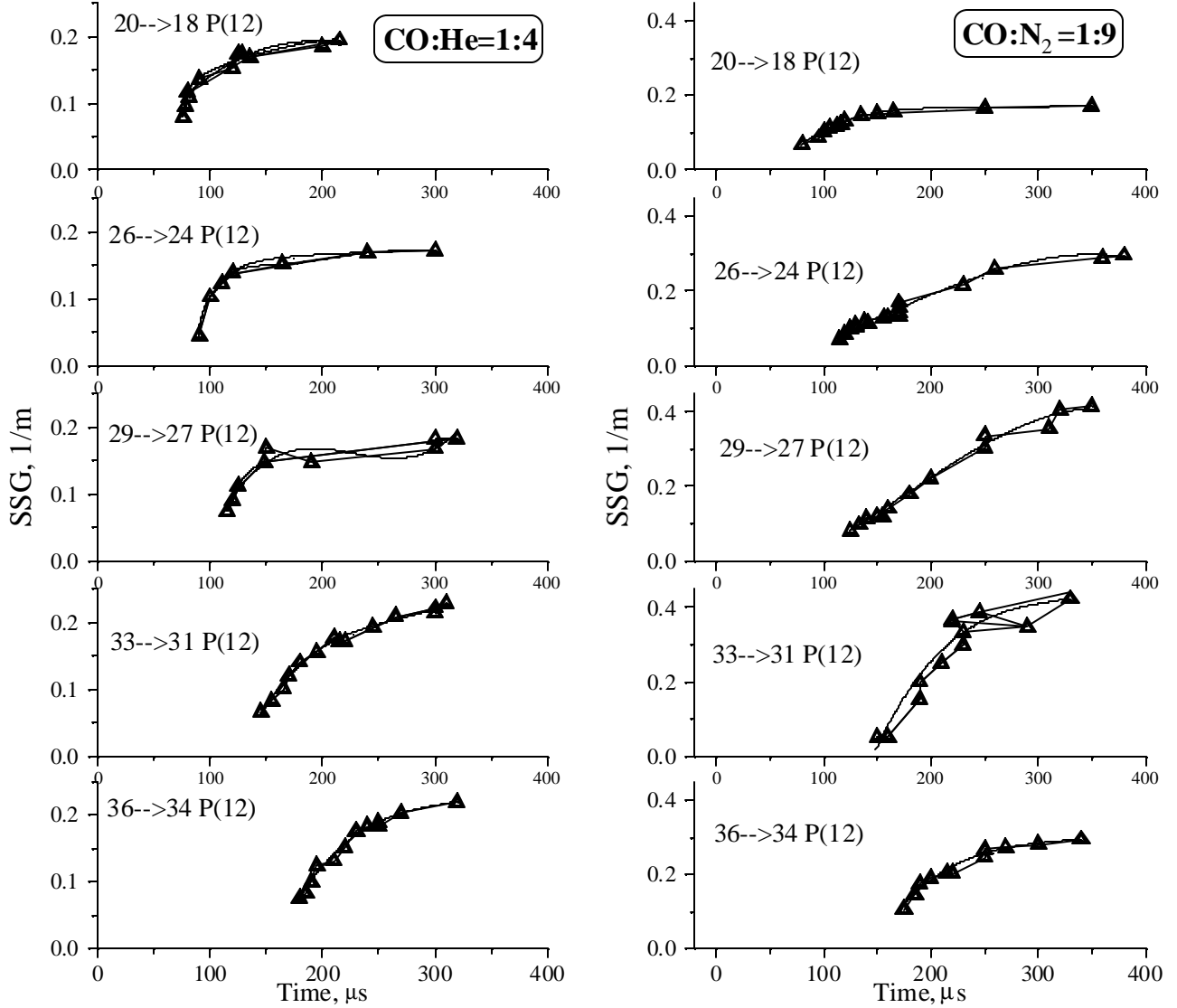


Fig.1.27. SSG time behavior measured for different laser mixtures: CO:He=1:4 (SIE $\sim 320 \text{ J/l Amagat}$) and CO:N₂=1:9 (SIE $\sim 320 \text{ J/l Amagat}$)

The dependencies of maximum SSG on the vibrational number have quite a different behavior for the two laser mixtures (Fig. 1.28b). Maximum SSG increases slightly with the vibrational number for nitrogen-free gas mixture CO:He being approximately $(0.2 \pm 0.05) \text{ m}^{-1}$. Maximum SSG increases noticeably for helium-free laser mixture CO:N₂ from 0.18 m^{-1} for the overtone transition $20 \rightarrow 18$ up to $\sim 0.4 \text{ m}^{-1}$ for the transition $33 \rightarrow 31$. There is the decrease of maximum SSG down to $\sim 0.3 \text{ m}^{-1}$ for higher vibrational transition $36 \rightarrow 34$. It should be noted that SSG rise time, defined as a time needed for SSG to increase from 0.2 up to 0.8 of its maximum value, is comparable for CO:He and CO:N₂ laser mixtures being $(100 \pm 30) \mu\text{s}$.

1.2.2. SSG measurement with master oscillator - laser amplifier system

The method of intracavity losses gives an opportunity of measuring SSG build up and rise time. However, it is difficult to apply it for measuring a tail of SSG pulse and SSG pulse structure. A master oscillator-laser amplifier system was used in our experiments for measuring above parameters. The optical scheme of the experiments is in Fig.1.29. Another pulsed FO CO laser was used as a master oscillator.

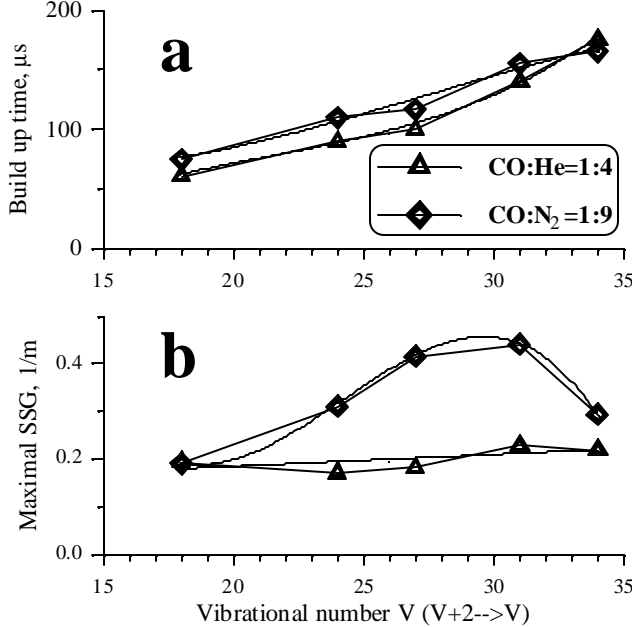


Fig.1.28. Dependencies of build up time (a) and maximum SSG (b) for two laser mixtures vs. the vibrational number V (vibrational transition V+2→V)

~0.5 ms. The laser facility described in section 2 was used as a laser amplifier 7. Laser mixture CO:N₂=1:9 at gas temperature of ~100 K and gas density 0.18 Amagat was used. SIE was ~390J/l Amagat. Temporal behavior of the laser pulse amplified in the two-pass amplifier (amplification length ~2.4 m) was measured by Au:Ge photodetector 8. Fundamental band superradiance from the amplifier was cut off by thin (~2 mm) flat 9 of fused silica.

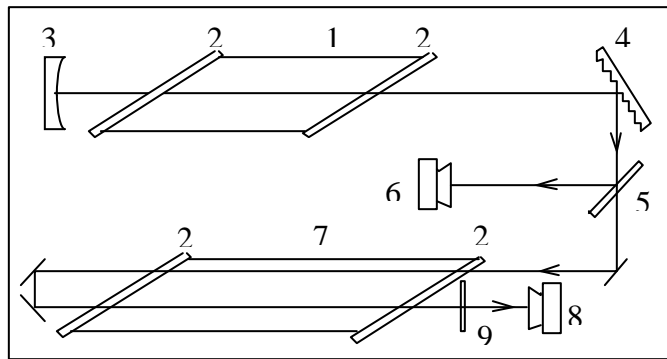


Fig.1.29. Optical scheme of the master oscillator-laser amplifier system 1-laser chamber, 2- Brewster window, 3-totally reflecting mirror, 4-diffraction grating, 5- flat made of CaF₂, 6- photodetector, 7-laser amplifier chamber, 8-Au:Ge photodetector, 9-flat made of fused silica

To measure SSG time behavior in the laser amplifier, master oscillator pulse 3 (Fig.1.30) was directed into the amplifier, time delay between pump electric discharge pulses for the master oscillator 2 and amplifier 1 being varied between +300 μs and -600 μs (“-“ means that amplifier pump pulse started earlier than master oscillator one). The comparison of pulse shapes at the entrance and the exit of the laser amplifier (Fig.1.30) for different time delays enabled us to measure SSG temporal behavior, which is presented in Fig.1.31 for the overtone transition 33→31P(12). Build up

time $\sim 100 \mu\text{s}$ and rise time $\sim 100 \mu\text{s}$ are in good agreement with the experimental results obtained in section 2. Maximum SSG values obtained with the method of intracavity optical losses and master oscillator - laser amplifier system were close to each other: $\sim 0.4 \text{ m}^{-1}$ and $\sim 0.3 \text{ m}^{-1}$, correspondingly. It should be pointed out, that SSG pulse tail is quite long being $\sim 1 \text{ ms}$, SSG life time is being longer than $\sim 1 \text{ ms}$.

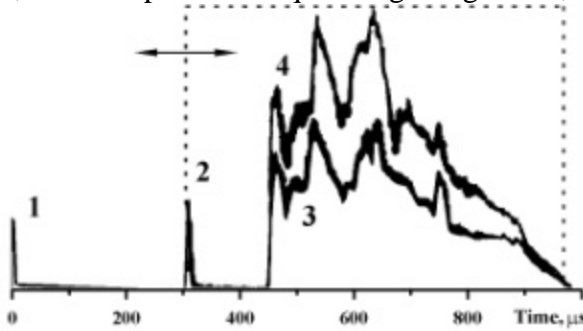


Fig.1.30. Temporal behavior of FO CO laser pulse intensity before (3) and after (4) the amplifier. The beginnings of pumping pulse of the master oscillator (2) and the laser amplifier (1) are shown. The laser transition $33 \rightarrow 31 \text{ P}(12)$

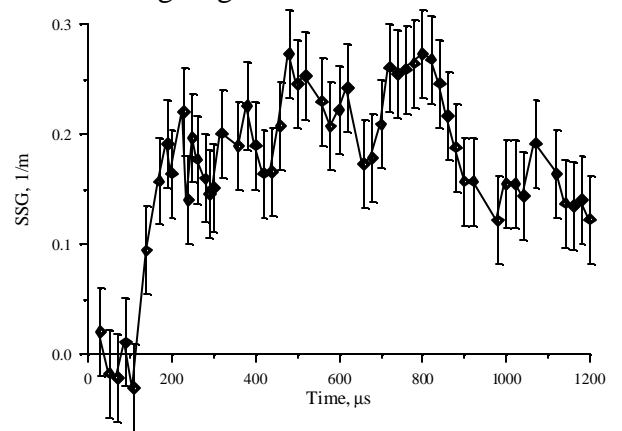


Fig.1.31. SSG temporal behavior for the overtone transition $33 \rightarrow 31 \text{ P}(12)$

1.2.3. FO CO laser spectrum formation

It should be noted that a low-pressure low-power CW FO CO laser operates on high vibrational transitions up to $37 \rightarrow 35$ (Urban, 1991; Bachem et al. 1993). The lack of FO CO lasing on higher overtone transitions was explained by vibrational energy transfer into the energy of electronic state $A^1\Pi$ of CO molecule (Farrenq and Rossetti, 1985). However, FO CO lasing does take place on the overtone transition $38 \rightarrow 36$ (Basov et al., 2000a,c,d). There was pointed out, that output energy of the FO CO laser operating on the overtone transitions $36 \rightarrow 34$ and $38 \rightarrow 36$ strongly depends on nitrogen concentration in laser mixture. In particular, while increasing nitrogen concentration, output energy for $36 \rightarrow 34$ transition increases and for $38 \rightarrow 36$ transition decreases.

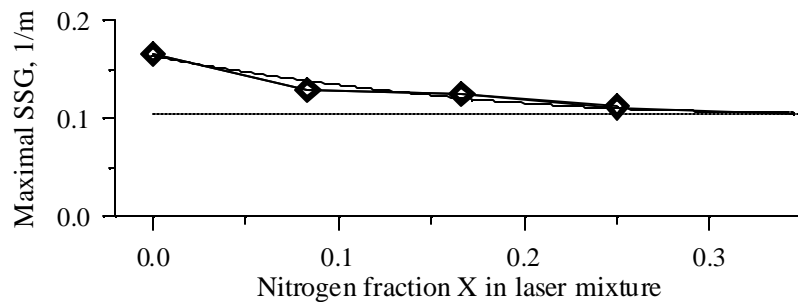


Fig.1.32. Dependence of maximum SSG for the vibrational transition $38 \rightarrow 36 \text{ P}(12)$ on nitrogen concentration X for laser mixture $\text{CO:He:N}_2=1:4:X$, $N=0.12 \text{ Amagat}$, $SIE=370 \text{ J/l Amagat}$.

The influence of nitrogen concentration upon SSG of $38 \rightarrow 36$ overtone transition was also observed experimentally. The dependence of maximum SSG for the vibrational transition $38 \rightarrow 36 \text{ P}(12)$ on nitrogen concentration X for laser mixture $\text{CO:He:N}_2=1:4:X$ is presented in Fig.1.32. (The method of intracavity optical losses was used, see section 1.2.1) Maximum SSG $\sim 0.16 \text{ m}^{-1}$ was obtained for nitrogen free mixture $\text{CO:He}=1:4$ ($X=0$). Increasing nitrogen concentration up to $X \approx 0.3$ results in 1.5 times

decrease of SSG. (The horizontal line in Fig.1.32 corresponds to threshold SSG for the laser resonator without additional optical losses).

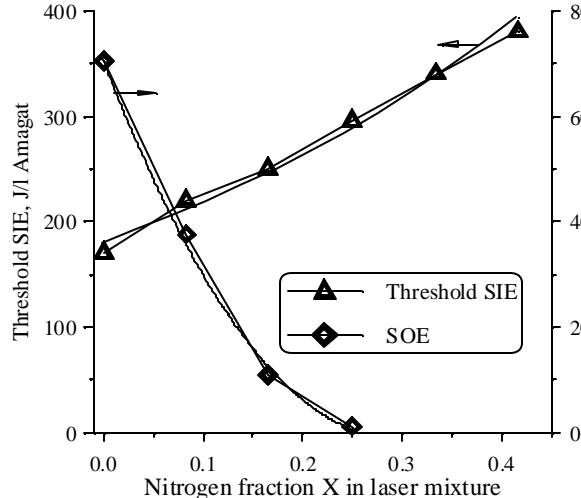


Fig.1.33. Threshold specific input energy (SIE) and specific output energy (SOE) at SIE=300 J/l Amagat vs. nitrogen fraction in laser mixture CO:He:N₂=1:4:X, N=0.12 Amagat.

FO CO lasing characteristics for the highest 38→36 overtone transition was also studied. The dependence of SOE on nitrogen content for the 38→36 P(14) spectral line is demonstrated in Fig.1.33 (SIE = 300 J/l Amagat). A little admixture of nitrogen results in SOE decreasing from 70 mJ/l Amagat (nitrogen fraction X=0) down to practically zero (X=0.25). With X increasing from 0 to 0.42, threshold SIE rises more than two times, from 170 J/l Amagat up to 370 J/l Amagat (Fig.1.33). Time delay of the laser pulse increases from 220 up to 340 μs (Fig.1.34) and laser pulse duration decreases from 180 down to ~10 μs (Fig.1.34). When X in the gas mixture reaches 0.5, lasing on the 38→36 vibrational transition is not observed at all. The phenomenon of nitrogen influence upon SSG and FO CO laser characteristics can be explained by quasi-resonant collisional interaction between the 38→36 vibrational transition of CO molecule and the 0→1 vibrational transition of N₂ molecule, so called asymmetric V-V exchange: N₂(0)+CO(V)→ N₂(1)+CO(V-2). (Transition 40→38 of CO molecule and 0→1 of N₂ molecule are exactly resonant) (see section 1.1).

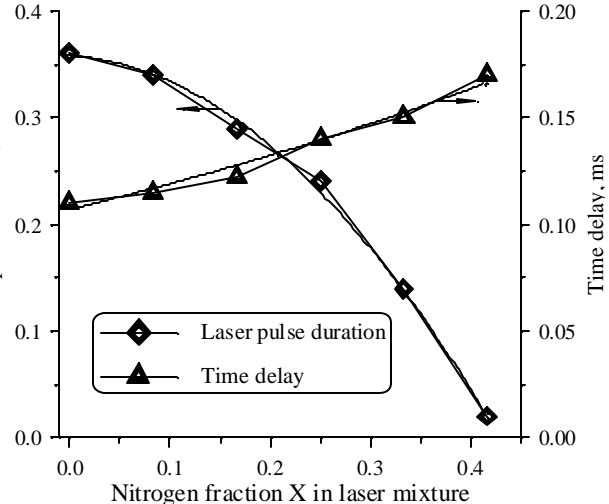
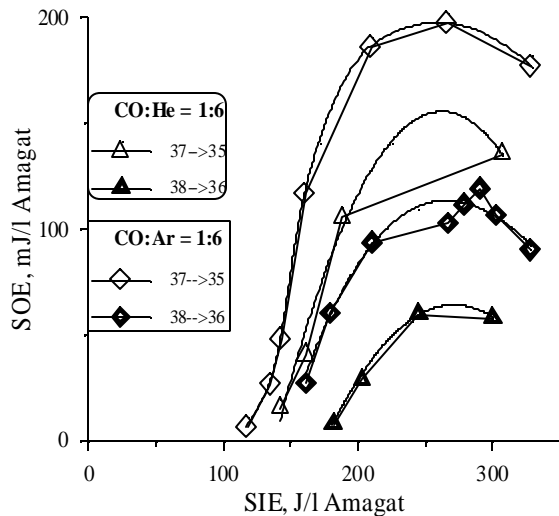


Fig.1.34. Time delay and laser pulse duration vs. nitrogen fraction in laser mixture CO:He:N₂=1:4:X, N=0.12 Amagat, SIE=370 J/l Amagat.

Fig.1.35. Specific output energy (SOE) for two different ro-vibrational transitions 38→36 P(14) and 37→35 P(13) vs. specific input energy (SIE) for various laser mixtures CO:He =1:6 and CO:Ar=1:6, N=0.12 Amagat

The usage of gas mixture CO:Ar=1:6 resulted in decreasing threshold SIE for the $38\rightarrow36$ P(14) and $37\rightarrow35$ P(13) spectral lines as compared with the gas mixture CO:He=1:6 (see Fig.1.35). Maximal magnitudes of SOE for these spectral lines obtained in the experiments increased up to 30% for $37\rightarrow35$ P(13) and almost two times for the $38\rightarrow36$ P(14) ro-vibrational transition when using CO:Ar laser mixture. This can be explained by decreasing influence of V-T relaxation which is stronger for the highest vibrational transitions with Ar in the gas mixture instead of He.

1.3. Comparative analysis of experimental and theoretical results

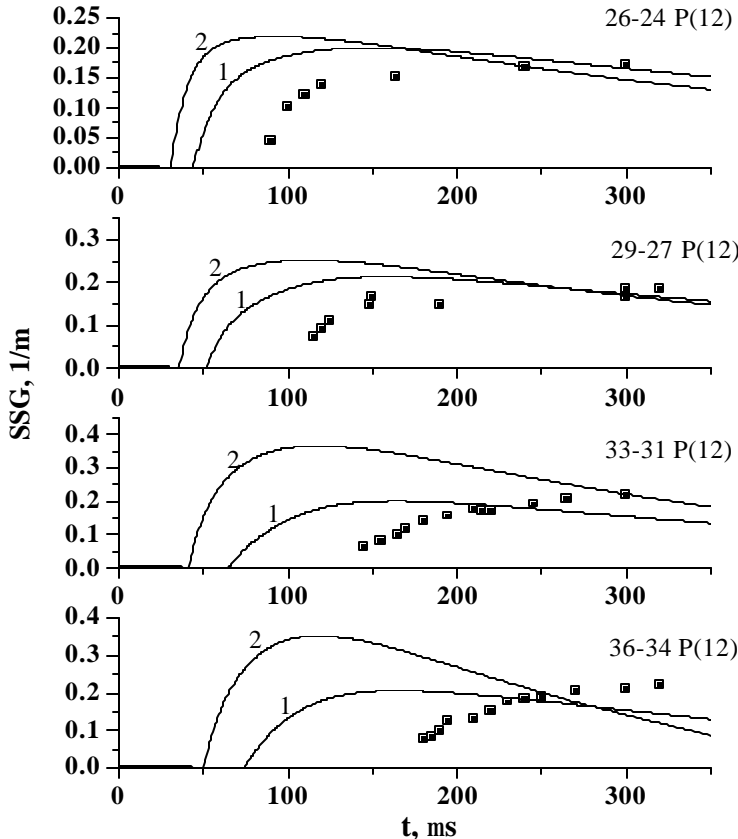


Fig. 1.36. The calculated and experimental SSG for high overtone transitions. 1 – ‘new’ MQE model is used; 2 – ‘old’ MQE model.

MQE-model (Ionin et al, 2000a) or “new” (see section 1.1.2). The comparison of calculated results with the experiment for four high-lying overtone transitions ($v=26\rightarrow24$, $v=29\rightarrow27$, $v=33\rightarrow31$ and $v=36\rightarrow34$) is presented in Fig.1.36.

One can see from this figure that the modified model describes the experimental results much better than ‘old’ one and leads to longer time delay, smaller gain amplitude and slower gain recession. However, the measured SSG time delay is obviously longer than that obtained in calculations. This problem remains for future studies.

We assume this discrepancy could be caused by acoustic disturbances of the active medium density. In any case the experimental SSG measurements with master oscillator – laser amplifier system (see Fig. 1.31) demonstrated the time modulation of SSG, which may be interpreted as a result of acoustic disturbances. It is necessary to point out also that both in the experiments (Fig.1.31) and in calculations with modified MQE model (Fig. 1.7) the SSG pulse tail is quite long ~ 1 ms.

Theoretical analysis of small N₂ adds into CO:He active medium based on modified MQE model was done in section 1.1.2. The corresponding calculated spectra presented in Fig. 1.9 demonstrate that the

The experimental data on time evolution of SSG for high overtone transitions of CO molecule are of particular importance for theoretical analysis because these data provide detailed information for the set of single ro-vibrational transitions in different vibrational bands, and such information was not hitherto available. The SSG values were calculated numerically for discharge and gas mixture parameters of the experiments described in section 1.2. We computed SSG time behavior only for CO:He mixture since this system is simpler and more convenient for comparison of experimental and calculated results. The calculations were made with either “old” rate constants of

increase of N_2 concentration leads to the rise of efficiency on transition lower than $v=37\rightarrow35$ and to disappearance of lasing on the transition $v=38\rightarrow36$. In Fig. 1.37, we compare the calculated and experimentally measured dependences of the output laser efficiency on N_2 concentration for transitions $v=38\rightarrow36$, $v=37\rightarrow35$ and $v=36\rightarrow34$. It is seen that experimental and theoretical dependences agree sufficiently well. Nevertheless, more exact values of rate constants for all processes, which control the VDF on high vibrational levels (see section 1.1), are desirable for more reliable modeling of effects on high

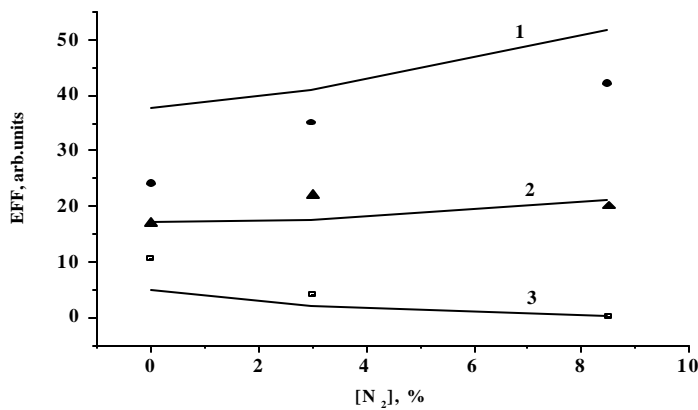


Fig. 1.37. Efficiency of frequency selective CO laser vs N_2 concentration 1 ~ $v=36\rightarrow34$; 2 ~ $v=37\rightarrow35$; 3 ~ $v=38\rightarrow36$.

vibrational transitions, caused by small N_2 adds.

1.4. Conclusions

Temporal behavior of SSG for a single-line FO CO laser operating on highly excited vibrational transitions has been studied both experimentally and theoretically. The vibrational transitions were studied from $20\rightarrow18$ up to $38\rightarrow36$ corresponded to FO CO laser spectral range between $\sim 3 \mu m$ and $\sim 4 \mu m$, which coincides with an atmospheric “transparency window”. Maximum SSG of 0.4 m^{-1} has been obtained for CO:N₂ laser mixture, maximum SSG for CO:He mixture being half as much. SSG build up time increases with the vibrational number being $\sim 70 \mu s$ for the low transition $20\rightarrow18$ and up to $\sim 170 \mu s$ for the upper transition $36\rightarrow34$, SSG build and rise time being independent of nitrogen or helium fraction. SSG life time for the experimental conditions exceeds 1 ms. The data obtained are extremely important not only for further development of theoretical model for a pulsed FO CO laser and/or master oscillator - laser amplifier system, but also for designing a fast flow CW FO CO laser facilities including a supersonic FO CO laser, because information about SSG build up and life time are necessary for determining position and configuration of a laser resonator for such kind of a FO CO laser.

Experimental study of gain and laser characteristics on the highest ever experimentally observed FO CO vibrational transition $38\rightarrow36$ has been carried out. These characteristics strongly depend on an amount of nitrogen admixture to nitrogen-free laser mixture CO:He = 1:4. This phenomenon has been explained by quasi-resonant collisional interaction between the $38\rightarrow36$ vibrational transition of CO and the $0\rightarrow1$ vibrational transition of N₂ ($40\rightarrow38$ CO and $0\rightarrow1$ N₂ are exactly resonant). The effect is important for better understanding of the kinetic processes taking place on highly excited vibrational levels of CO molecule.

The modification of the MQE kinetic model was made according to recent theoretical and experimental data on V-V, V-T processes and Einstein coefficients. This led to the better agreement with the experimental SSG measurements. The role of asymmetric two-to-one quanta V-V exchange and of V-T relaxation processes on high vibrational levels was studied.

The data on spectral and energetic characteristics of multi-line FO CO laser using output mirrors from AFRL were presented in (Ionin et al., 2001b).

Part II. Theoretical and experimental study of RF discharge in gas mixtures with CO

Introduction

RF excited CO lasers have a number of advantages over analogous CO₂ lasers. These are: shorter wavelength allowing for better beam focusing and higher electro-optical efficiency. However, there are quite a few experimental and theoretical studies on RF discharge plasma properties for typical CO laser gas mixes. Earlier, we have developed numerical codes for modeling waveguide and slab CO₂ lasers (Ilukhin et al, 1996; Ochkin et al, 1996) and waveguide lasers on IR atomic Xe transitions (Ilukhin et al, 1998) for RF discharge excitation. As a first stage, these numerical codes were adopted to simulate discharge characteristics in CO containing gases. At this phase, no attempt was made to account for influence of different vibrational or electronic levels populations on plasma properties.

There is a number of publications on experimental studies on RF excited CO lasers. They may have thermal diffusion cooling or fast gas flow in the discharge and resonator. RF discharge with the diffusion cooling traditionally has a configuration formed by two plane electrodes separated by a gap of several millimeters length. The typical value for spacing is 2 mm. To achieve a specific high-power of output radiation it is necessary to cool effectively gas in the resonator. With increase of the active medium volume thermal diffusion is becoming ineffective. Then the only way to cool the gas is organization of fast gas flow. In this case, the typical discharge gap has a length of a few centimeters.

The experiments on studying the properties of RF discharge in gas mixtures containing CO molecules were carried out to compare experimentally obtained and theoretically calculated data. Modified and refurbished room temperature RF CO₂ "slab" laser setup with diffusion cooling of discharge region was used in the experiments. Binary mixtures He:CO with respective concentration of CO from 0 up to 20% at total pressure of 30 and 60 Torr were investigated. The dependencies of inter electrode voltage (RMS value) and voltage-to-current phase shift on specific input power (SIP) loaded into RF discharge were obtained. The results of the experiments were compared with numerical calculations.

2.1. RF discharge modeling for CO laser conditions

2.1.1. Fast flow discharge modeling

Despite a great number of experimental studies on RF excited CO lasers, authors are aware only of one publication (Kanazawa et al, 1994) where the discharge plasma properties for typical CO laser gas mixes were examined. The laser mixture CO:N₂:O₂:He = 5:16:0.4:78.6 was blown through the rectangular discharge chamber with sizes 4 (discharge spacing)x3.5 (electrodes width along flow)x 28 (electrodes length) cm³ with flow velocity of 30 m/s at pressure 40 - 60 Torr and temperature 200 K. RF discharge frequency was 13.6 MHz. In this publication the discharge voltage was measured as a function of discharge power. The discharge voltage was found by direct measurement by means of electric probe (Kanazawa et al, 1994). The RF discharge has dielectric electrodes with thickness growing along gas flow to stabilize discharge in view of gas heating and diminishing of its density. When giving an interpretation of results obtained, the authors (Kanazawa et al, 1994) assumed that dielectric electrodes have much lower electric capacitance than the electric boundary layers. The root-mean-square (RMS) of voltage drop on discharge plasma was calculated, as the RMS value of discharge voltage multiplied by $\cos\phi$, ϕ is the phase difference between discharge current and voltage.

To model the experimental results from (Kanazawa et al, 1994) the 1D numerical model was exploited. It was assumed that the electron attachment is completely compensated by detachment

processes in collisions of negative ions with CO molecules. Gas temperature and density were considered as constants. The numerical code for RF discharge includes electron and positive ion kinetics. Fluid equations for both these components were solved in space-time in parallel with Poisson equation. Electrical drift and diffusion of electrons were taken into account. In conditions of Ref. (von Bulow et al, 1993a) corresponding to a fast gas flow through the discharge zone gas heating can be neglected. Therefore, gas temperature and density were considered as constants. The system of equations was completed by boundary and initial conditions, which are self-evident for the considered situation. All the transport and kinetic coefficients were calculated as functions of E/N (E is the electric field strength and N is gas density number) from solution of space-time independent Boltzmann equation for a spherically symmetric component of electron velocity distribution function.

1D space grid was taken non-uniform with cell's size diminishing nearby electrodes. Typical number of space steps was about 100. To achieve an established mode of operation, a number of thousands of RF field cycles was necessary to be computed, and this took about 2 hours for IBM compatible computer with Celeron-466 processor.

Results of numerical calculations were compared with the experimentally measured RMS-values of discharge voltage for different discharge power values.

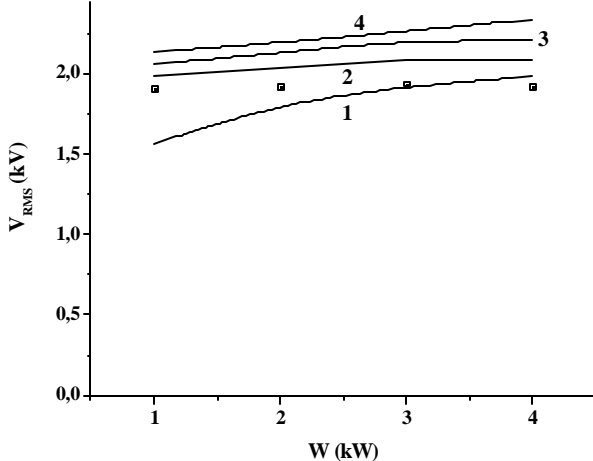


Fig. 2.1. Dependence of RMS discharge voltage vs input power from RF source. Squares are experimental data from (Kanazawa et al, 1994). Simulated RMS discharge voltage across the active resistance of plasma local model (1) (Ilukhin et al 1996); across the all plasma, including sheathes local model (2) (Ilukhin et al, 1996); across the all plasma, including sheathes, local model (3) (Starostin et al, 2000); across the all plasma, including sheathes, non-local model (4) (Starostin et al, 2000)

Besides the described above numerical code, some calculations were made using two versions of a numerical code developed by our colleague S. A. Starostin from The University of Twente, Enschede, the Netherlands. One of these versions exactly corresponds to our approach, the other approximately accounts for non-locality of the electron energy distribution function. A simplified approach described in Ref. (Boeuf et al, 1990) accounts for non-local effects introducing the hydro-dynamic equation for the electron mean energy where the electric drift and diffusion processes were included (Starostin et al 2000). At every moment the electron mean energy was calculated as a function of space variable in the inter-electrode gap.

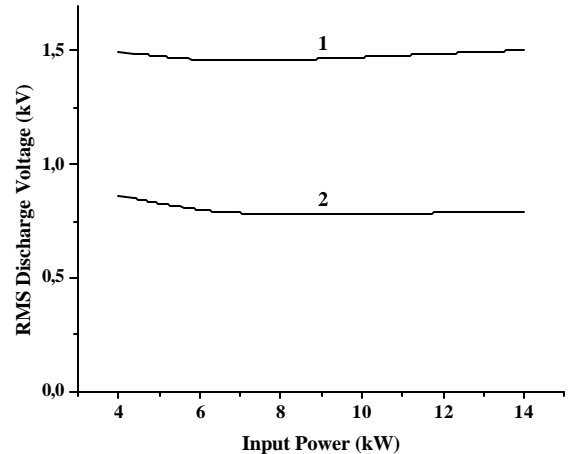


Fig. 2.2. Dependence RMS discharge voltage vs input power from RF source. 1 is the discharge gap length 1.1 ?m, 2 – 0.55 ?m

Separately, by solving electron Boltzmann equation for steady state electric field the kinetic coefficients were found in parallel with the mean energy. Then the ionization rate was considered as a function of the electron mean energy correspondent to the given electric field. In a similar way, the transport coefficients necessary to solve the time-dependent equation for the electron mean energy were found, too. The difference between results of calculations by two Twente versions of the numerical code was insignificant for conditions of the experiment (Kanazawa et al, 1994).

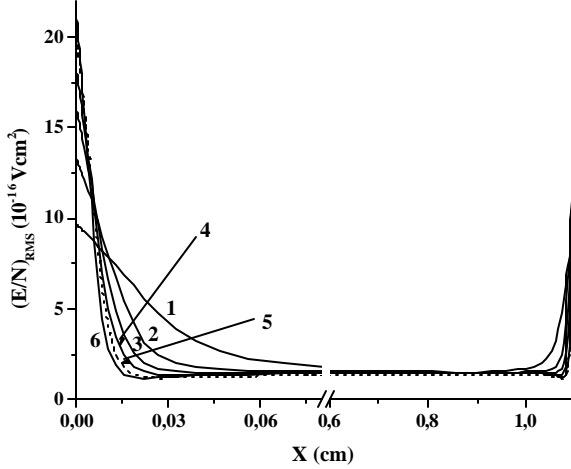


Fig. 2.3. Spatial profiles for the RMS of the reduced electric field strength value $(E/N)_{RMS}$ for the discharge gap length 1.1 cm. 1 – 4 kW, 2 – 6 kW, 3 – 8 kW, 4 – 10 kW, 5 – 12 kW, 6 – 14 kW

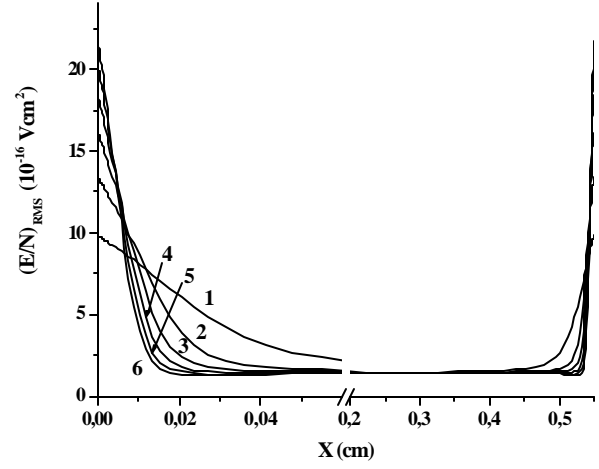
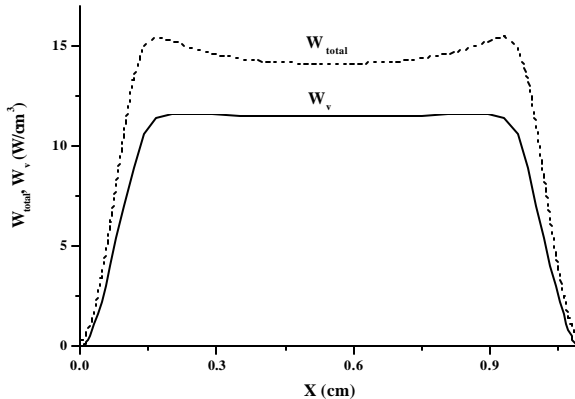
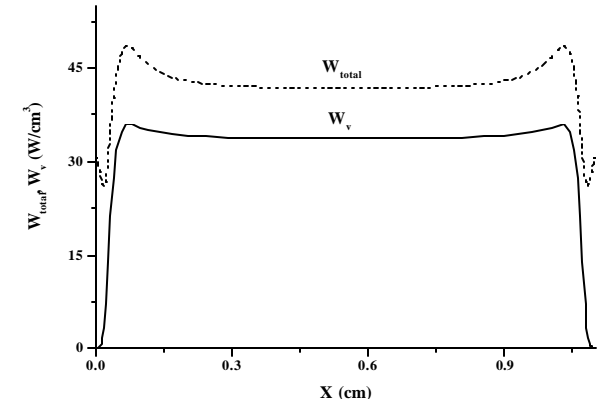


Fig. 2.4. Spatial profiles for the RMS of the reduced electric field strength value $(E/N)_{RMS}$ for the discharge gap length 0.55 cm. 1 – 4 kW, 2 – 6 kW, 3 – 8 kW, 4 – 10 kW, 5 – 12 kW, 6 – 14 kW



a)



b)

Fig. 2.5. Spatial profiles for total discharge power density W_{total} and molecular vibration consumed power density W_v for gas mix $\text{NO:He:O}_2=10:89.6:04$, $P = 250$ Torr, $T = 295$ K, discharge gap length 1.1 cm, voltage frequency 13.6 MHz, space averaged power density: 12.6 (a); 42 W/cm^3 (b)

The RMS-values of the reduced electric field and averaged in time positive ion number density distributions were calculated for different discharge powers 1, 2, 3 and 4 kW at gas pressure 60 Torr for conditions of the experiments (Kanazawa et al, 1994). A balance of electron impact ionization and electron-ion recombination controls the electron number density at the center of the discharge gap. The ionization rate strongly depends on E/N. Therefore, to increase the electron number density and electric current at higher discharge power it is sufficient to raise E/N a little bit. Near electrodes the dominant

component of the current is the displacement current. It grows with increasing the electric field or diminishing the boundary layer thickness. The positive ion concentration has a pronounced maximum at the discharge power 4 kW, and this is an evidence of the transition from the α -mode of the discharge to the γ -mode.

Considering the results presented in Fig. 2.1 as a model verification, the discharge was modeled for conditions, close to the experiments in (von Bulow et al, 1993b), where gas mixture was $\text{CO:He:O}_2 = 12.4:86.6:1$ at pressure 285 Torr, temperature 300 K, RF field frequency 13.6 MHz. In Fig. 2.2 the RMS-voltage-power characteristics is presented for two values of the discharge gap length 1.1 and 0.55 cm. The voltage for the gap length 1.1 cm is nearly 2 times higher than for the gap length 0.55 cm. This is explained by a small fraction of boundary layer voltage in comparison with the voltage drop on discharge plasma. In Figs. 2.3 and 2.4 the spatial profiles for the quantity $(E/N)_{\text{RMS}}$ are presented at discharge power 4, 6, 8, 10 12 and 14 kW and for two values of the discharge gap length. For conditions considered, the thickness of the electric boundary layers apparently depends on the discharge power.

As a result of numerical calculations, spatial distributions for the electric field strength, electron and ion number densities, power density dissipated in plasma by electrons (W_e) and ions (W_i) were found for different moments within RF cycle. Important for the laser operation, efficiency of vibrational levels excitation is controlled by the value of E/N varying in space and time. Therefore, the power density spent by electrons for vibrational levels excitation averaged over the RF cycle, W_v was calculated, too. Fig. 2.5a, b show spatial profiles of the total electric power density (W_{total}) and W_v for gas mixture $\text{CO:He:O}_2 = 10:89.6:0.4$ at pressure 250 Torr, temperature 295 K discharge gap length 1.1 cm, RF field frequency 13.6 MHz and space-averaged total electric power density equal to 12.6 and 42 W/cm³, respectively.

These results are obtained for conditions close to that in Ref. (von Bulow et al, 1993a). Figures 2.5a and 2.5b demonstrate that up to 80% of electric power in RF discharge can be deposited into molecular vibrations of CO. At higher power, the fraction of ion component of electric power within electrode layers grows. However, because of small width of these layers in comparison with discharge gap this effect exerts negligible influence on discharge efficiency.

2.1.2. Discharge model for a diffusion cooled CO slab laser

RF excited slab CO lasers demonstrated a rather high efficiency and laser power. Authors of (Colley et al, 1994) achieved 80 W with laser efficiency 12% with waveguide walls cooled down to -30 C. For cryogenically cooled waveguide walls the output power was 1020 W and laser efficiency 25% (Xin et al, 1999).

In slab lasers the active volume is cooled by thermal conductivity to the waveguide walls, therefore the earlier described numerical code for RF discharge modeling was extended by inclusion an equation for the gas temperature (Ilukhin et al, 1996). As the boundary condition, the temperature of the walls was fixed. There are published data on thermal conductivity

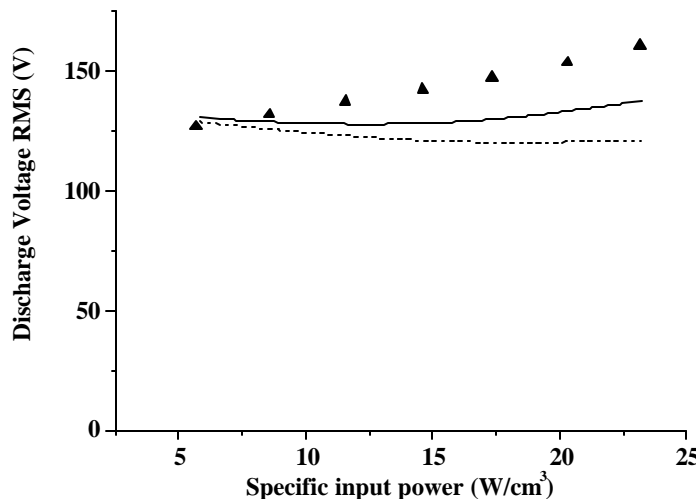


Fig. 2.6. Discharge voltage (RMS) vs specific input power for RF discharge. Triangles show experiment (Kun et al, 1995). Solid and dashed lines present results of full and local models, respectively

coefficients only for pure gases (Grigoriev et al, 1991). We used the method of calculations of thermal conductivity coefficients for gas mixtures exploited in the active medium, which was proposed in Ref. (Mason et al, 1958). In this method, the thermal conductivity coefficient for the laser mixture has been calculated using known molecular weights and thermal conductivity coefficients for individual gas components of the mixture, which were taken from (Grigoriev et al, 1991).

To verify the theoretical model developed we need results of experimental measurements of RF discharge characteristics for typical conditions of CO laser. For diffusion-cooled slab configuration we were able to find only one reference where such data were published (Kun et al, 1995). The RF discharge excited by the electric field with frequency 81.36 MHz in gas mixture $\text{CO:N}_2:\text{He:Xe} = 1:3:12:2$ at pressure 90 Torr and temperature $T=300$ K was studied in this work (Kun et al, 1995). The discharge region was of rectangular form with sizes: $0.25 \times 3 \times 23$ cm 3 . Two versions of the discharge model were exploited for simulations of the experiments (Kun et al, 1995): fluid equations in local approximation (all kinetic coefficients depend on the local value of instant electric field); fluid equations including electron energy transport (“full” model, where all kinetic coefficients are expressed as functions of the average electron temperature). Fig. 2.6 presents comparison of computed in two approximations dependence of RMS value of the discharge voltage on the specific input power with experimental data from (Kun et al, 1995). It is seen that the difference between predictions of two versions of the discharge model is small, and “full” model closer to the measured values of the voltage. This comparison indicates that our model gives a satisfactory description of the experiment. This fact encourages us to make numerical simulations for the experimental conditions of Ref. (Colley et al, 1994).

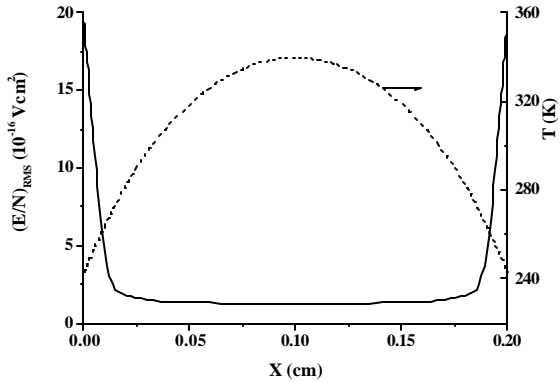


Fig. 2.7. Spatial profiles for the root mean square reduced electric field strength and gas temperature for conditions of (Colley et al, 1994)

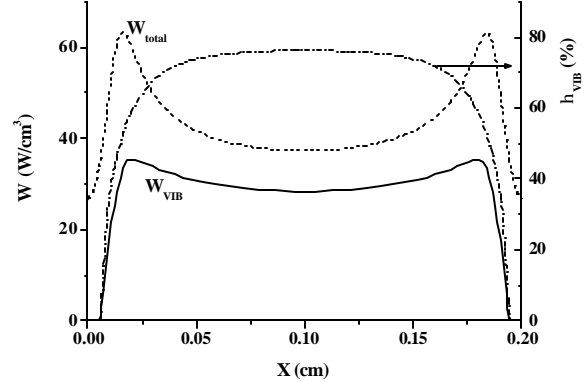


Fig. 2.8. Spatial profiles of total power density, power density going to vibrations excitation, and of their ratio for conditions of Fig. 2.7

In Fig. 2.7 the computed root mean square of E/N parameter and gas temperature profiles are presented for the conditions of Ref. (Colley et al, 1994): gas pressure $p=75$ Torr; $\text{CO:He:Xe:O}_2 = 1:10:0.4:0.045$; RF frequency 125 MHz; the spatially averaged discharge power density 43.2 W/cm 3 ; the discharge gap length 2 mm; electrode temperature 243 K. Discharge power fraction spent for excitation of molecular vibrations of CO molecule was calculated for an instant value of the E/N -parameter by solving the electron Boltzmann equation for the symmetrical part of the electron energy distribution function (EEDF), and then was averaged over one RF cycle. The ion current component simply dissipated in gas by heating it. The high value of E/N -parameter and low electron number density nearby electrodes were the reasons for a low efficiency of CO vibrational levels excitation. Fig. 2.8 presents results of calculations of a total discharge power density (W_{total}) and of a discharge power density fraction spent for CO vibrational

levels excitation (W_{VIB}). In the same figure, the quantity $\mathbf{h}_{VIB}(x) = W_{VIB}(x)/W_{total}(x)$ is shown, which characterized efficiency of CO vibration excitation in RF discharge. The magnitude presented is slightly lower than the value calculated above for conditions of (von Bulow et al, 1993a). This is because now the value of pd is lower than earlier. Diminishing the gas pressure and/or discharge gap length results in reduction of fraction of discharge volume occupied by uniform plasma, where an effective excitation of molecular vibrations took place. The ratio of discharge power consumed by molecular vibrations to the total discharge power is 64.8%.

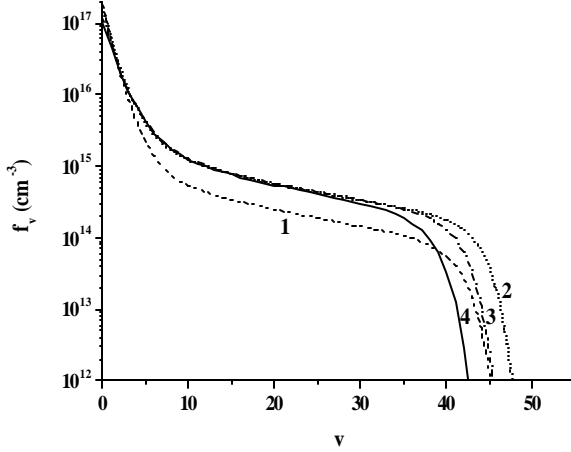


Fig. 2.9. VDF for CO molecules in different locations within the discharge gap. 1 – $6.8 \cdot 10^{-3}$ cm, 2 – $1.3 \cdot 10^{-2}$ cm, 3 – $3.4 \cdot 10^{-2}$ cm, 4 – $1.0 \cdot 10^{-1}$ cm from the electrode

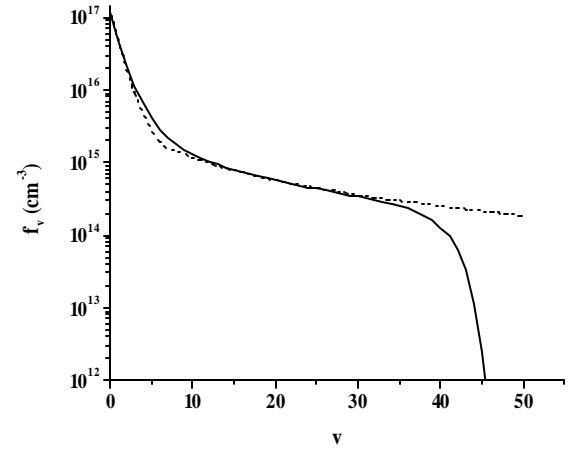


Fig. 2.10. Comparison of analytical and numerical CO VDFs. Solid line for numerical results, dots for analytical solution. Location is $3.4 \cdot 10^{-2}$ cm from the electrode

In our model the diffusion of vibrationally excited molecules to the walls (electrodes) was neglected. When computing the thermal energy balance in the discharge, the spontaneous emission was neglected. It was ignored correlation between gas ionization/de-ionization and vibrational excitation degree. At every position along the discharge gap, a steady state CO vibrational distribution function (VDF) was calculated using known values averaged over the RF cycle for power density spent for vibrational excitation, W_{VIB} , gas temperature and density. The following processes were included: electron impact excitation; vibration-vibration (V-V) exchange; vibration-translational (V-T) relaxation and spontaneous emission. The necessary rate coefficients were taken from Ref. (Ionin et al., 1998b). In Appendix II of Ref.(Ionin et al., 2001b) the numerical subroutine is presented for calculations of V-V exchange rate constants (single quantum exchange approximation).

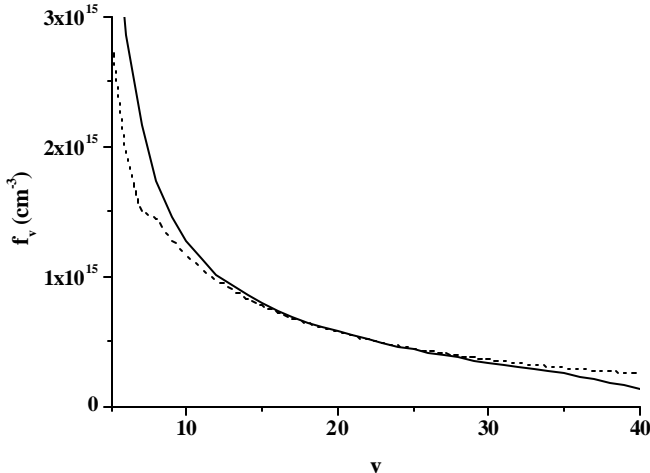


Fig. 2.11. Detailed comparison (linear scale) of VDFs for CO. Solid line for numerical results, dots for analytical solution. Location is $3.4 \cdot 10^{-2}$ cm from the electrode

The steady state VDF was found by iterative procedure involving solving master equation system for populations of vibrational levels f_v with number v . Time for computing one variant with a relative accuracy 10^{-5} for two consecutive iterations (number of vibrational levels 51, discrete spatial mesh contains 100

cells) is about 300 s for IBM compatible computer ‘‘Celeron-466’’.

Fig. 2.9 shows the computed VDFs for CO molecules in different locations in discharge in conditions of the experiment (Colley et al, 1994). As it was noted above, the power for excitation of molecular vibrations is down nearby electrodes. As a result, populations of high vibrational levels are lower (curve 1). While approaching the discharge center, the pumping density varies slowly, and populations on the levels $v=10\div30$ are almost constant. On still higher levels, the effect of accelerating V-T relaxation with gas temperature growing to the center is remarkable. Then populations for these levels are reducing (compare curves 2, 3, 4). Fig. 2.10 demonstrates agreement between analytical predictions (Dem’yanov et al, 1981) and numerical calculations. In this comparison the analytical theory was slightly modified by inclusion more realistic dependence of dipole transition matrix elements taken from Ref. (Our report to EOARD (old model of CO laser)). Analytical and numerical curves diverge for $v\geq35$, what is explained by ignoring V-T relaxation in analytical considerations. For laser characteristics evaluation, it is important to describe correctly a plateau of the VDF ($v\geq9$). A detailed comparison between analytical and numerical calculations is shown in Fig. 2.11. Note using a linear scale for the VDF. It is seen that analytical theory is in good agreement with calculations in the region of plateau.

Analyzing results of numerical simulations, the fast growth of vibrational temperature for lower levels from the discharge walls to the center is associated, in the first line, with pumping power increase seen in Fig. 2.8. Further slow growth of the vibrational temperature for lower levels is explained by analytical theory, which couples this temperature with gas temperature by the formula (Dem’yanov et al, 1981)

$$\frac{E_1}{T_v} = 4.6 \sqrt{\frac{\Delta E}{T}} .$$

Here E_1 is the energy of the first vibrational level, and ΔE is anharmonicity factor.

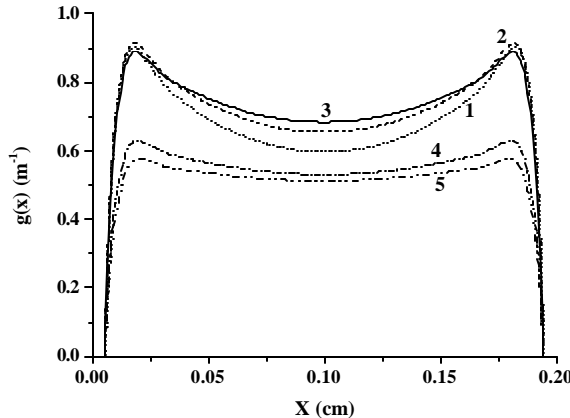


Fig. 2.12. SSG profile within the discharge gap for transitions: 1 – 12P(12), 2 – 12P(13), 3 – 12P(14), 4 – 12P(15), 5 - 12P(16)

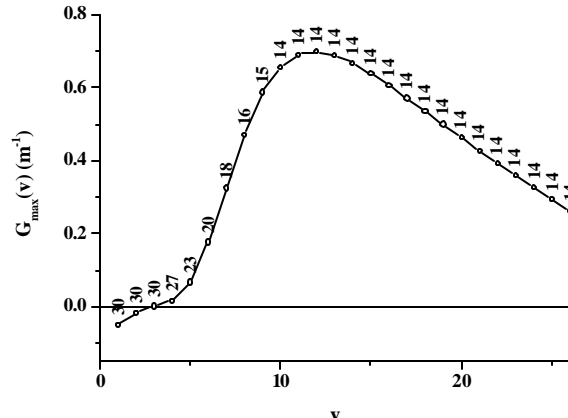


Fig. 2.13. Maximum SSG as a function of the lower vibrational level number. Numerals along the curve denote J for which the SSG is maximum

For description of CO laser, a key role plays the spatial distribution of the small signal gain (SSG) for different rotational-vibrational transitions. In cw CO laser, only the partial inversion is realized, which is rather sensitive to the VDF shape and gas temperature. As along the discharge gap the pumping power and gas temperature are varying, it is expected that the SSG for various vibrational bands has a maximum at different rotational numbers. Fig. 2.12 illustrates spatial profiles of the SSG for selected transitions in the band 13→12. Individual transitions are specified in a traditional fashion: designation of a line $vP(J)$ is used for the transition ($v+1, J-1$)>(v, J). Nearby electrodes the gas temperature is lower, and the SSG is maximum for lower J . In the center of the discharge gas temperature is higher, and the SSG is maximum for

transitions with larger J. For each transition, the average SSG was calculated by integration over the discharge gap according to the formula:

$$G_{v,J} = \frac{1}{d} \int_0^d g_{v,J}(x) dx .$$

Maximum value among calculated in this way SSG set for the fixed vibrational band was found. Fig. 2.13 presents how this maximum gain depends on the number of the vibrational transition. Along the curve, J numbers corresponding to the maximum averaged over spacing gain are shown, too. Gain spectrum has a typical for CO lasers shape: for low v the maximum of gain takes place at high J, for higher v the maximum position is shifted to lower values of J, and this dependence saturates with v growth.

As a result of work on the project, two versions of the numerical code for RF discharge modeling in CO-laser gas mixtures were developed and verified by the existing experiment. Satisfactory agreement demonstrated for fast-flow and diffusion cooled discharges indicates to usefulness of the package developed.

2.2. Experiments on RF discharge in gas mixtures containing CO molecules

2.2.1. Modification of the experimental RF discharge installation.

Experimental RF CO_2 laser setup was modified to perform the study of RF discharge in gas mixtures containing CO molecules. New gas mixing and vacuum pumping system was manufactured and connected to the RF discharge chamber. The system allowed us to mix up to four gases (CO , N_2 , He , X ; $\text{X}=\text{O}_2$, Ar , H_2 etc) directly inside the discharge chamber. Gas mixture pressure in the discharge chamber may be varied from $\sim 10^{-2}$ Torr (vacuum pumping) up to 1 atmosphere. The control of gas mixture components partial pressure was realized by means of different kinds of vacuum meters. The accuracy of pressure measurements was ± 0.1 Torr in the pressure range of 10^{-2} -10 Torr, ± 0.25 Torr in the range 10-30 Torr and ± 1.0 Torr in the range of 30-760 Torr. Also there was the possibility to use liquid N_2 cooled trap for extracting water vapor out of gases during the process of gas mixture composition.

Thermopile measuring system was included in the RF discharge chamber setup to control the power of gas heating inside the discharge zone. Two thermopiles were introduced into the water supply plastic tubes used for the electrode system cooling. They were positioned closely to water inlet and to water output points respectively. The system allowed us to monitor the difference less than 0.05K between input and output water flow temperature. This value corresponded to the heat power measurements accuracy better than ± 1 W with respect to typical planned value of input power of 100-250W. The thermopile system was calibrated to measure the input RF power dissipated in the RF discharge plasma and taken out by cooling water. The reference curve for cooper-constantan thermopile voltage is shown in Fig.2.14.

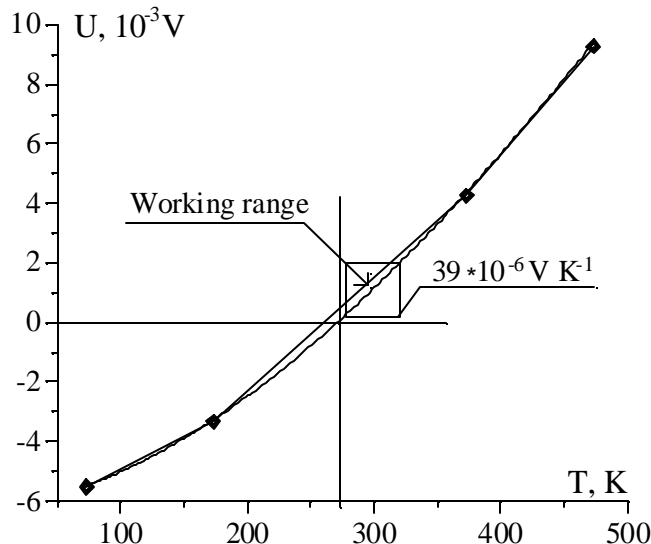


Fig. 2.14. The cooper-constantan thermopile reference curve (Grigoriev, 1991). One thermojunction of the thermopile have the temperature $T=273\text{K}$.

The Volt-Kelvin ratio S in the vicinity of $T \sim 290$ K appeared to be $S=39*10^{-6} \text{ VK}^{-1}$. Taking into account the real cooling water consumption ($dV/dt \sim 10 \text{ cm}^3\text{s}^{-1}$), water heat capacity per unit volume ($C=4.2 \text{ Jcm}^3\text{K}^{-1}$) and the sensitivity of measuring digital microvoltmeter ($dU_{\min}=1*10^{-6} \text{ V}$) we estimated the accuracy dP_{\min} of input power measurements by following relation:

$$dP_{\min}=dV/dt*C*dU_{\min}*S^{-1} \sim 1 \text{ W.}$$

So, during the operation of RF generator with output power up to ~ 250 W, the accuracy of input RF power measurements will be better than 1%.

2.2.2. Power supply, measuring system and additional electrical setup.

Narrow band four-channel generator usually used in aircraft radio stations (working frequency 81.3 MHz) was taken as a base of the RF discharge pumping system for the gas excitation. The scheme of the generator was modified for parallel simultaneous usage of all channels with mutual agreement and final summing of its output RF powers. Original power supply converter (220 VAC \Rightarrow stabilized, regulated 20-30 VDC, maximal output current up to 40 A) was constructed for the generator. During the tests of the generator operating at maximal output RF power (\sim 230 W) on equivalent active load, we observed significant and increasing (depending on working time) overheating of output RF transistors in final amplifiers of the generator. The overheating leaded to strong shifts of final amplifiers parameters, to its disagreement and, as a consequence, to sharp decrease of output RF power of the generator with the risk of its breakage. Additional high speed turbo fan (with its own power supply: 400 Hz, 30 VAC, 10 A) was integrated into the RF generator device to normalize its thermal regime. The repeated tests demonstrated that for all output RF powers of the generator (from \sim 50 up to \sim 230 W), semiconductor elements regimes have settled fast enough (during the time \sim 2-3 s) and remained stable during all the time of test circle (test circle duration \sim 10 min).

New electrical circuits were added to the discharge chamber to control RF discharge parameters.

- Manually driven wide range reactive impedance LC network was connected to the electrode system to match the total impedance of discharge chamber to 50Ω input power line.
- Calibrated RF power split-meter was integrated into the input power line to monitor the (reflected power)/(forwarded power) ratio minimum, that indicated the coincidence of input power line impedance and discharge chamber impedance.
- Two exactly identical capacitive sensors were coupled to both electrodes for time resolved (minimal step \sim 0.2 ns) measurements of its potentials with respect to the fixed ground point. The inter-electrode voltage time behavior was obtained by synchronous subtraction of these two potentials after respective calibration procedure.
- Low inductance, high resistance voltage dividing circuit was connected to discharge electrodes to obtain the signal that was phase proportional to amplitude of inter-electrode RF voltage. Inductive sensor was located near the input matching circuit to obtain the signal proportional to the discharge current. Phase shift between RF voltage and discharge current was calculated by measuring the time delay between the signals from these two sensors.

Two double-channel high frequency oscilloscopes were used to measure the parameters of RF discharge: amplitude (or RMS) value of inter-electrode voltage and current-to voltage phase shift dependencies versus input RF power. Final release of the experimental facility electrical scheme is presented in Fig.2.15.

Both cables in pairs (for measuring signals $U_1 \& U_2$ and $\sim U \& \sim I$) were exactly of the same length to avoid additional phase shifts. Oscillograms presented on Fig.2.16 illustrate the procedure of U_{RF} calculation using measured time dependencies of U_1 and U_2 . Measured maximal amplitude values of U_{RF} (U_{RF}^{AMP} , see Fig.2.16) were converted into inter-electrode RMS voltage using the relation: $U_{RF}^{RMS} = U_{RF}^{AMP} * 2^{-0.5}$.

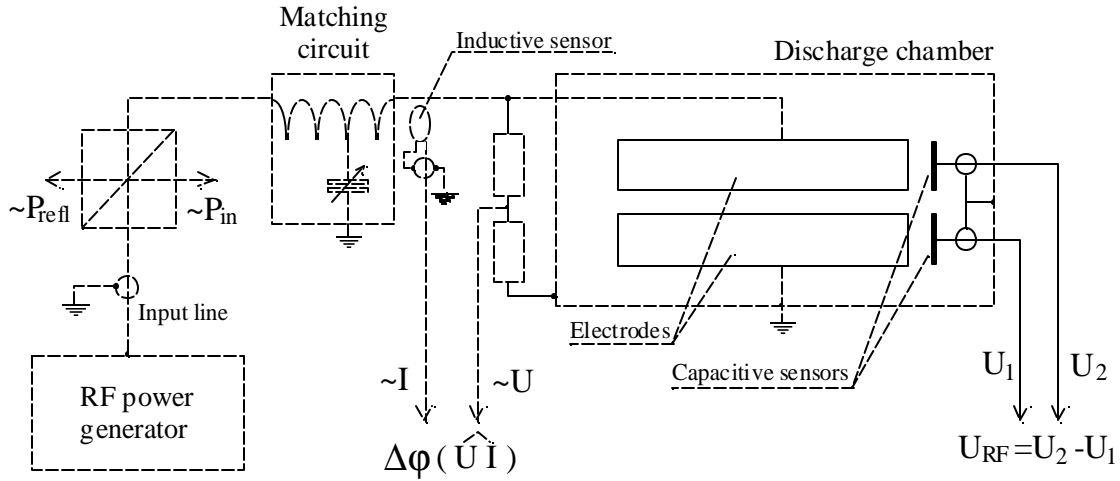


Fig.2.15. Electrical scheme of the RF discharge facility.

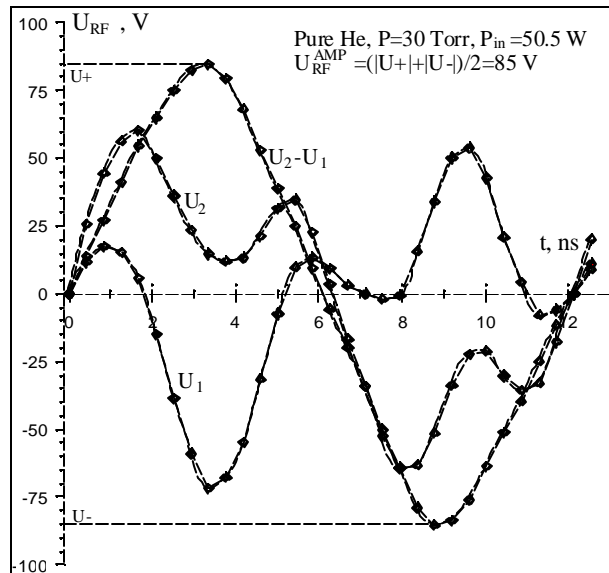


Fig.2.16. Typical oscillogram illustrated the procedure of inter-electrode voltage measuring and following calculations.

2.2.3. Experiments on RF discharge in transversal "slab" geometry.

The experiments on RF discharge were carried out in four gas mixtures He:CO=1:X, where X=0, 0.05, 0.1 and 0.2. The mixture components ratios X were chosen taking into account the theoretical modeling of the discharge parameters, where the same ones were used. Two values of the gas mixture total pressure (30 Torr and 60 Torr) were used in the experiments. The dependencies of inter-electrode RMS voltage on the total specific input RF power were measured for these conditions (Fig.2.17a). RF discharge volume in the experiments was equal to $24.5 \times 1.5 \times 0.25 = 9.2 \text{ cm}^3$. The same RF discharge characteristics calculated numerically are presented in Fig.2.17b. Measured in the experiments dependencies of current-to-voltage phase shift on SIP needed for the theoretical calculation are presented in Fig.2.18.

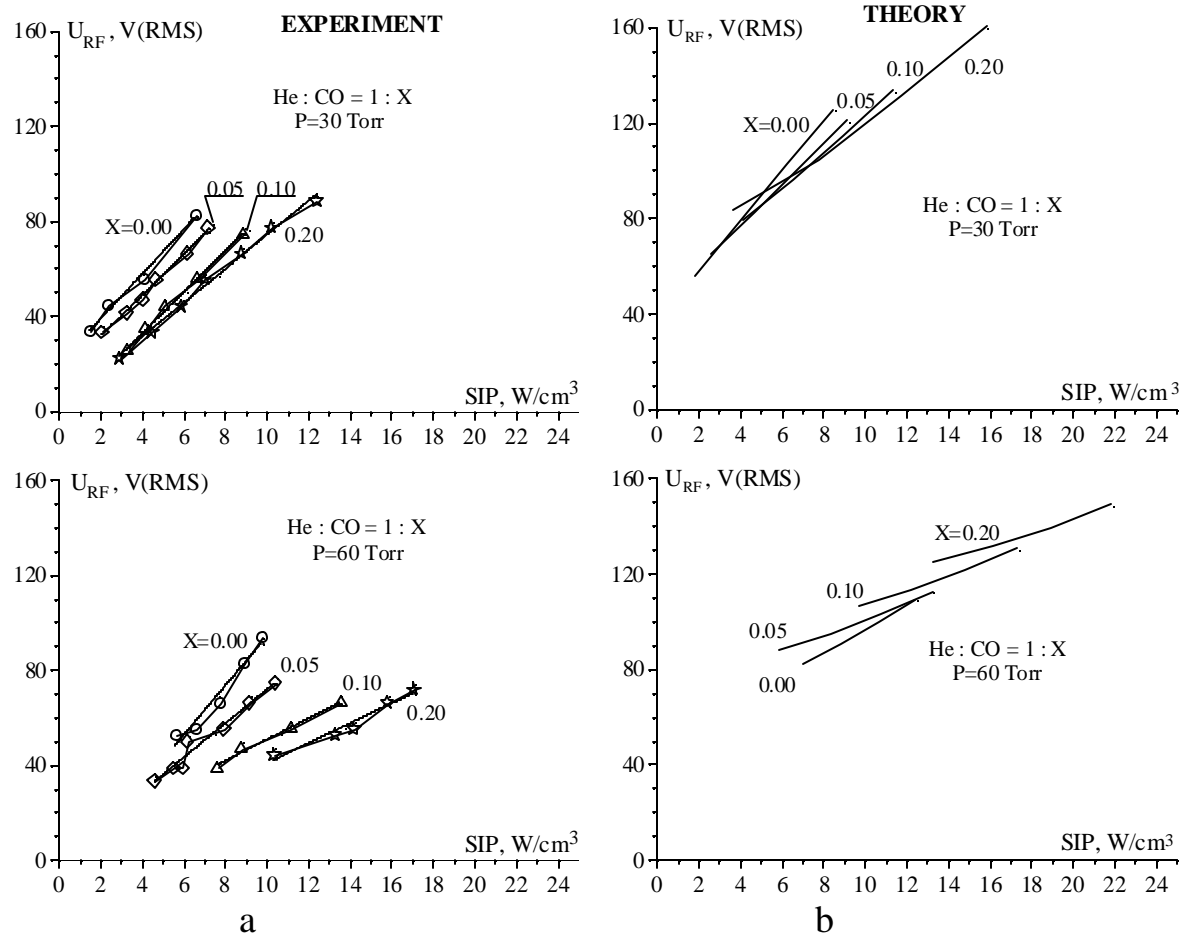


Fig. 2.17. Dependencies of inter-electrode RMS voltage on the specific input RF power for different component ratio and total pressures of gas mixture. (a) - experiment, (b) - theory.

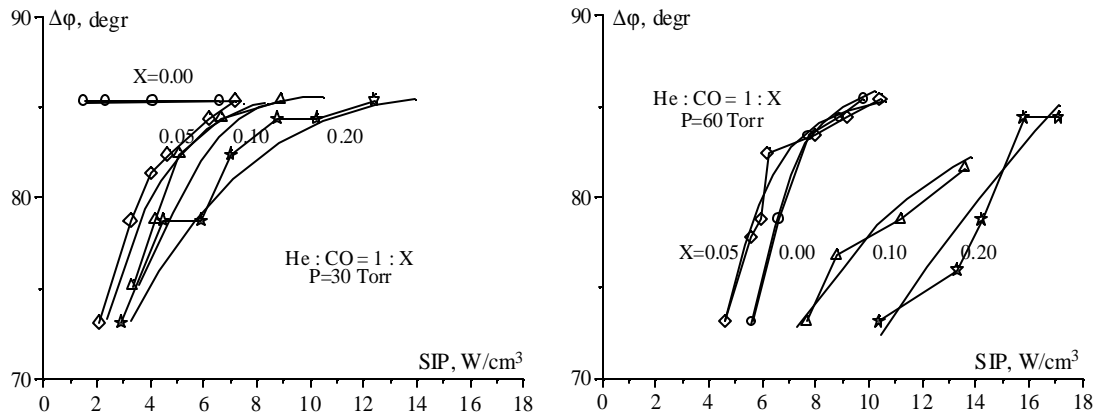


Fig. 2.18. Dependencies of RF discharge voltage-to-current phase shift on the specific input RF power for different component ratio and total pressures of gas mixture. (Experiment)

RF discharge specific input power corresponded to the minimal ("normal") current density, when RF discharge volume was homogeneously filled by discharge plasma, was determined during the experiments (Table 2.1).

Table 2.1. RF discharge specific input power corresponded to the minimal stable power loading.

He:CO=1:X	P=30 Torr	P=60 Torr
X=0.00	SIP ^{min} ~1.5 W cm ⁻³	SIP ^{min} ~5.5 W cm ⁻³
X=0.05	SIP ^{min} ~2.0 W cm ⁻³	SIP ^{min} ~4.5 W cm ⁻³
X=0.10	SIP ^{min} ~3.0 W cm ⁻³	SIP ^{min} ~7.5 W cm ⁻³
X=0.20	SIP ^{min} ~3.0 W cm ⁻³	SIP ^{min} ~10.0 W cm ⁻³

2.2.4. Experimental measurements of impedance and maximal SIP depending on mixture content and gas pressure.

It was shown experimentally that for available configuration of the electrode system (discharge volume 24.5 x 1.5 x 0.25 cm³) and RF generator frequency (fixed at ~81 MHz) the maximal input RF power that can be loaded into stable RF discharge was restricted only by non-overloading mode of RF generator operation (see Table 2.2). These maximal input powers were ~115 W (SIP~12.5 W cm⁻³) and ~156 W (SIP~17 W cm⁻³) for the total pressure of 30 Torr and 60 Torr, respectively (gas mixture He:CO=1:0.2).

Table 2.2. RF discharge specific input power corresponded to the maximal power loading.

He:CO=1:X	P=30 Torr	P=60 Torr
X=0.00	SIP ^{max} ~7.0 W cm ⁻³	SIP ^{max} ~9.5 W cm ⁻³
X=0.05	SIP ^{max} ~7.5 W cm ⁻³	SIP ^{max} ~10.0 W cm ⁻³
X=0.10	SIP ^{max} ~9.0 W cm ⁻³	SIP ^{max} ~13.5 W cm ⁻³
X=0.20	SIP ^{max} ~12.5 W cm ⁻³	SIP ^{max} ~17.0 W cm ⁻³

Taking into account the maximal output power of RF generator (~250 W) the way of the increasing of the total input RF discharge power is to use higher gas mixture pressure (up to ~100 Torr).

2.2.5. Data analysis

The comparative analysis of experimental and theoretical data obtained for the same conditions (see Fig.2.17a and 2.17b) showed that there are some problems concerning the accuracy of the modeling description of real experiments.

1. In general, all experimental points are located lower (about 30-50%) than theoretical ones on the U_{rf} vs. SIP diagram. It should be noted that in the experiments the inter-electrode voltage was measured at the ends of discharge electrodes (see Fig.2.15). RF power input connector was located at the center of the electrode system and due to the wave effects the profile of the inter-electrode voltage across the electrode length (245 mm) may be non-uniform. These effects were not taken into account in the modeling experiments.

2. The mutual position of theoretical curves corresponded to different CO molecules concentration is similar to experimental ones for the gas mixture pressure 30 Torr: increasing of CO concentration in gas mixture leaded to the increase of SIP that could be loaded into discharge at the same inter-electrode

voltage (Fig.2.17a and 2.17b, top diagrams). Another behavior of theoretical curves one can see in case of total gas pressure 60 Torr (Fig.2.17b, bottom diagram): increasing of CO concentration in this case leaded to the decrease of SIP that could be loaded into discharge at the same inter-electrode voltage.

3. The experimental curves have the same transformation tendencies (with respect to the increasing CO concentration) for both investigated pressures of the gas mixture (30 and 60 Torr). Thus, we can conclude that in our experimental conditions the impedance of RF discharge plasma decreased with the increase of CO molecules concentration in gas mixture.

Conclusions

Two versions of the numerical code for RF discharge modeling in CO laser gas mixtures were developed and verified by comparison with experiments on fast-flow and diffusion-cooled discharges. The numerical code taking into account effects of non-local electron energy distribution function in approximation of mean electron energy balance equation is more adequate for description of RF discharges, in particular at pressures lower than 50 Torr. The vibrational kinetic equations were introduced into the model of diffusion cooled RF discharge. This allows us to calculate spatial profiles of the VDF and SSG.

Further progress in RF discharge modeling can be made provided new more extended experimental data appear. Studies performed earlier by von Bulov demonstrated enhanced gas heating in comparison with simple theoretical estimations. It would be reasonable to analyze the causes for increased gas heating in the RF discharge in subsonic flow. One of factors to be evaluated is dissociation of O₂ and CO by electron impact with following relaxation of vibrational energy in collisions with O atoms. Modeling CO laser with diffusion cooling can be advanced in following directions: 1) inclusion of a subroutine for calculations of laser power based on usage waveguide optical modes, both for a constant refractive index profile and for index gradient produced by electrodes cooling; 2) for RF pumped laser operated in the overtone band it is necessary to account properly an influence of vibrationally excited molecules on ionization balance; 3) modification of electron continuity equation to include non-local effects.

Taking into account all the work (experimental and theoretical) which was carried out during the project and obtained results we can conclude:

There are serious experimental problems concerning accurate measurements of RF discharge parameters using electrode system geometry optimized for "slab" lasing when discharge region dimensions ratio is ~ 1 (electrode spacing) / 10 (electrode width) / 100 (electrode length). If we need to study RF discharge properties, special experimental setup should be developed and optimized for these purposes. The setup has to have probes coupled with the electrode system for accurate measuring of inter-electrode voltage, discharge current and RF power loaded into discharge. The electrode system has to be of special geometry and small size to exclude the influence of wave effects and other non-linearities on the results of measurements. Really, the RF discharge setup being developed in such a way will not be suitable for laser experiments at all. And on the contrary, "slab" geometry RF discharge setup optimized for lasing experiments usually is very inconvenient instrument for accurate study of RF discharge plasma parameters.

Further development of the theoretical model is necessary for better agreement of calculated an measured values of RF discharge parameters. The study should include both incorporating of new information about physical processes in RF discharge plasma in the model and modification of numerical codes by taking into account special features of existed experimental setup. Also up to this moment we have not the explanation for different behavior of theoretical curves families corresponding to total gas pressures 30 and 60 Torr.

Part III. Resonant absorption of first-overtone CO laser radiation by atmospheric water vapor and pollutants

Introduction

There was demonstrated quite recently that first-overtone (FO) CO laser [Bergman et al., 1977; Basov et al., 1978] is effective source of coherent IR radiation within spectral range of 2.5-4.2 μm , experimentally observed and theoretically calculated output efficiency of multiline FO CO laser coming up to 11% and 20%, respectively [Basov et al., 1999a-c; Ionin et al., 1998a-d, 1999]. Single-line FO CO lasing on more than 400 ro-vibrational lines was experimentally obtained with maximum output efficiency of 0.6% [Basov et al., 1999b-d]. The spectral range of FO CO lasing is very attractive, because it overlaps with 3-5 μm atmospheric "transparency window" and a lot of absorption lines belonging to numerous atmospheric pollutants and natural substances such as H_2O , CO_2 , O_3 , CH_4 , N_2O , NO_2 , NO , SO_2 , HCN , NH_3 , H_2CO , HOCl , CH_3Cl , C_2H_2 , C_2H_6 , CO , HCl , HF , HBr , HI , OH and various volatile organic substances such as acetone, benzene, toluene, hydrazine, methanol, ethanol, butanol, etc. FO CO laser seems to be quite a competitive source of IR radiation with well known chemical HF (DF) laser and frequency tunable optical parametric oscillators operating in the same spectral range, and looks like an attractive device for various applications such as remote sensing, spectroscopic gas analysis, medicine, etc.

Resonant absorption of FO CO laser radiation by atmospheric water vapor and various organic and inorganic pollutants is discussed in this chapter. Suitable ro-vibrational lines are selected for their potential use in traditional spectroscopic schemes of gas detection and for FO CO laser spectrum matching atmospheric "transparency windows". Atmospheric absorption of intense multiline FO CO laser radiation is simulated to exhibit an opportunity of FO CO laser application in future new spectroscopic detection schemes. Spectroscopic experiments were carried out with single-line FO CO laser. Absorption coefficients of ethanol and acetone vapor, N_2O and CH_4 on several FO CO ro-vibrational lines were measured. A comparative analysis of spectral characteristics of FO CO laser and HF (DF) laser demonstrates that potential of FO CO laser applications for spectroscopic detection of various molecular trace gases is greater than that of HF and DF lasers.

3.1. Spectroscopy of atmospheric gases within FO CO lasing spectral range

FO CO laser operates within 2.5-4.2 μm spectral range, that corresponds to overtone ro-vibrational transitions $(V+2,J-1)\rightarrow(V,J)$ with $V=4-36$, $J=4-25$ [Basov et al., 1999b-d]. **Fig. 3.1,a** demonstrates positions of FO CO laser lines within this spectral range calculated by using spectroscopic parameters of CO molecule presented in [Guelashvili et al., 1983]. For comparison, positions (location) of well-known chemical HF and DF lasers spectral lines calculated by using data of [Sengupta et al., 1979], are presented in **Figs. 3.1,b** and **c**. One can clearly see that FO CO laser spectrum region covers that of HF and DF lasers, interline spacing ($\sim 2 \text{ cm}^{-1}$) being far less than that of HF (DF) laser, i.e. the number of FO CO laser spectral lines available for practical use in the IR are much higher than that of HF (DF) laser.

The knowledge of atmospheric transmission spectra is of very importance for various laser applications. **Fig. 3.2** demonstrates typical linear transmission spectra (i.e. the spectra, that do not depend on radiation intensity) for the main atmospheric absorbers within 2.5-4.3 μm spectral region such as water vapor, carbon dioxide, methane and nitric oxide. One can clearly see from the **Fig. 3.2** that atmospheric vapor plays the principal role in absorption of laser radiation mostly in the short wavelength range of FO CO laser spectrum. Laser radiation on spectral lines lying within 3.4-4.2 μm spectral region is very suitable for efficient transportation through atmospheric air. It should be noted, that FO CO laser output spectrum strongly depends on spectral characteristics of laser optical elements. It enables us to control output

spectrum within rather wide spectral range. For example, two experimentally obtained multiline FO CO laser spectra are presented in **Figs. 3.2,d,e** [Basov et al., 1999b,c; Ionin et al., 1998d, 1999].

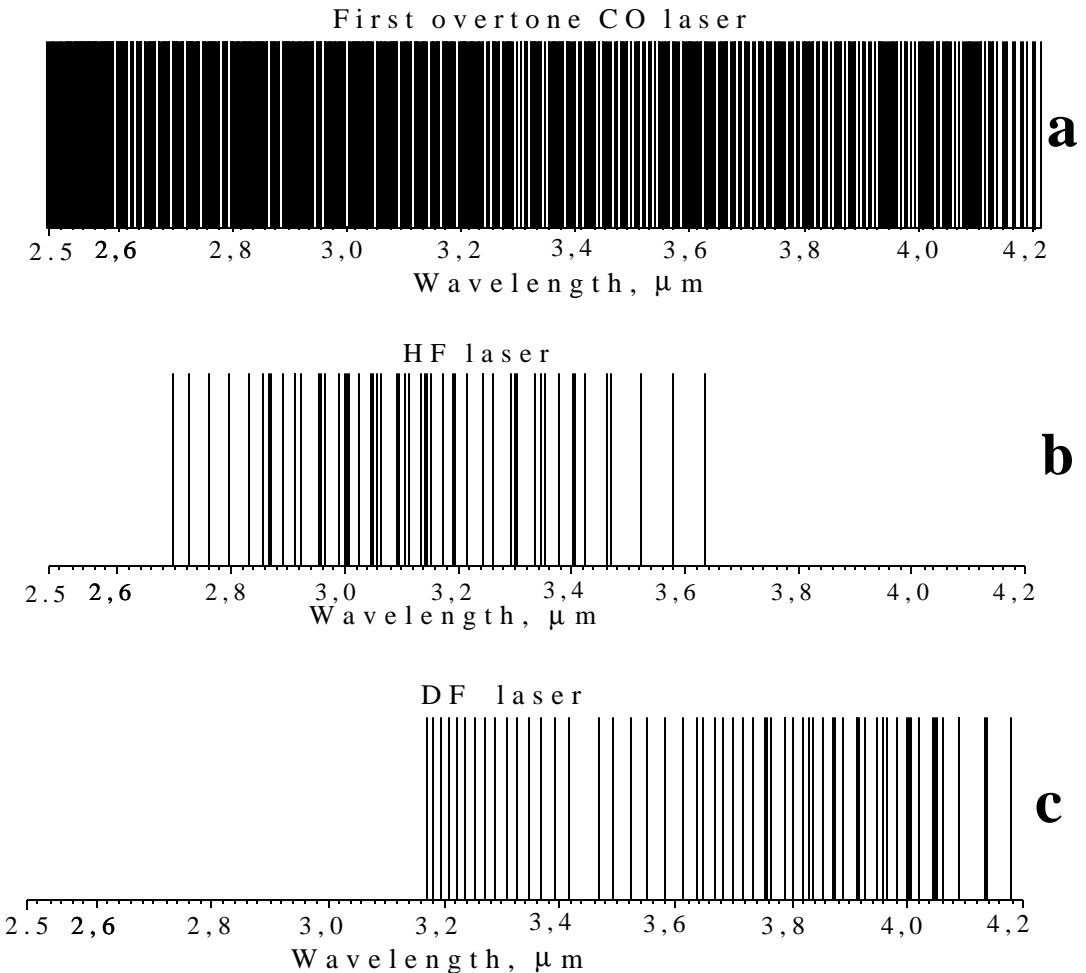


Fig. 3.1. Positions of emission lines of FO CO (a), HF (b) and DF (c) lasers within 2.5-4.2 μm spectral region.

For the purposes of spectroscopic diagnostics it is necessary to obtain good coincidences of laser lines with strong absorption lines of detected substances. Such laser lines are called analytical ones. Resonances with ro-vibrational transitions of different atmospheric molecules were searched for emission lines of FO CO and HF (DF) lasers using HITRAN-96 database [Rothman et al., 1992] and the conditions of atmospheric model No 6 - standard U.S. atmospheric model [Anderson et al., 1988; De Bievre et al., 1984] at altitude of $H = 0$ km. In this model total pressure is 1 atm, gas temperature is 288.2 K; relative concentrations of principal absorbing gases are: H_2O - 7750 ppmV (this corresponds to 46% relative humidity), CO_2 - 330 ppmV, CH_4 - 1.7 ppmV, N_2O - 0.32 ppmV ('ppmV' - parts per million by volume). The results are collected in the **Tables 3.1 - 3.3**. Rigorous selection criteria were used:

- 1) nearly exact resonance (within halfwidth of molecular absorption line);
- 2) the contribution of selected line into absorption cross-section is greater than 10^{-20} cm^2 .

The last columns in the tables contain absorption coefficients of the selected line in the atmosphere. In the case of detection of pollution these coefficients must be small. Emission lines with medium absorption characterized by the coefficient $0.1 \text{ km}^{-1} < \alpha_{\text{air}} < 1 \text{ km}^{-1}$ are labeled in **Tables 3.1-3.3** as (*); with strong

absorption ($1 \text{ km}^{-1} < \alpha_{\text{air}} < 10 \text{ km}^{-1}$) - as (**); with very strong absorption ($\alpha_{\text{air}} > 10 \text{ km}^{-1}$) - as (***)
Atmospheric absorption coefficients were calculated neglecting H_2O and CO_2 continuum contributions.

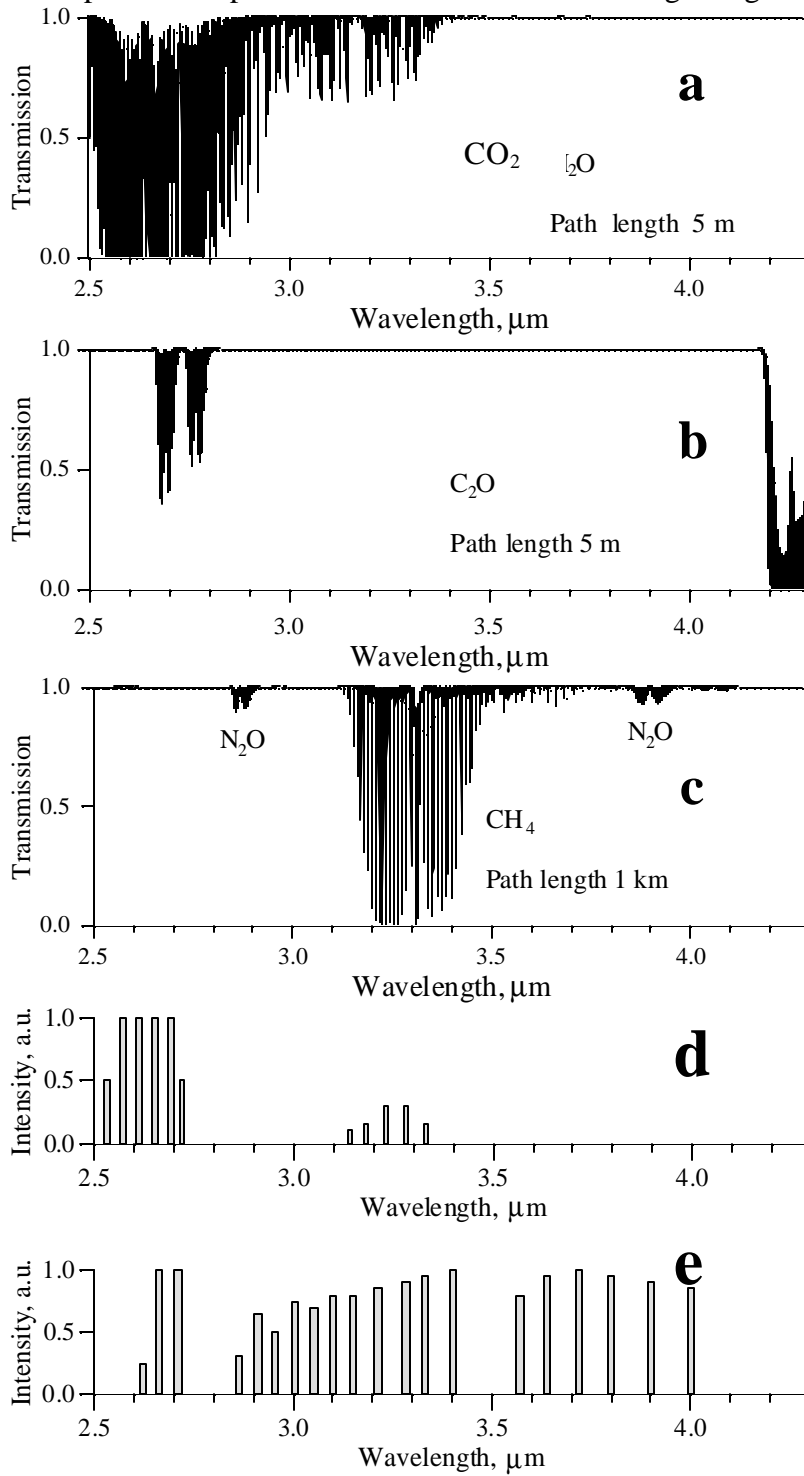


Fig. 3.2. Linear transmission spectra of atmospheric water vapor (a), carbon dioxide (b), methane and N_2O (c) within 2.5-4.2 μm spectral region. Experimentally obtained multiline FO CO laser spectra without rotational structure (d, e) [Basov et al., 1999b,c; Ionin et al., 1998d, 1999].

Standard atmospheric conditions at altitude $H=0$ km: total pressure is 1 atm, temperature is 288.2 K; relative concentrations of principal gases are : H_2O - 7750 ppmV (this corresponds to 46% relative humidity), CO_2 - 330 ppmV, CH_4 - 1.7 ppmV, N_2O – 0.32 ppmV.

Table 3.4 summarizes the results of the **Tables 3.1-3.3**. One can see that the share of analytical lines among tested ones and the share of weak absorbing lines in the atmosphere among analytical lines are intermediate one for FO CO laser as compared with HF and DF lasers. As for the diversity of detected

gases, FO CO laser has the leading position. In general, FO CO laser possesses significant potential for the applications in spectroscopic gas analysis. These potentialities are greater than those of HF and DF lasers.

It is interesting for practical use to determine those FO CO laser frequencies whose absorption coefficients in the atmosphere are maximum and minimum. The results for such 50 FO CO lines are presented in **Tables 3.5** and **3.6**. The conditions of calculations were the same as for the **Tables 3.1-3.3**, however, additionally continuum absorption was taken into account and its influence was examined. It is evident from the **Table 3.6** that for some lines continuum contribution to absorption is noticeable.

3.2. Theoretical model for nonlinear absorption of FO CO laser radiation

In order to clarify the FO CO laser high-power radiation transmission through the atmosphere, we have developed self-consistent theoretical model and computer code for the simulation of IR atmospheric absorption spectra under the action of intense IR radiation [Ivanov et al., 1998]. The model and code consist of two interconnected parts – spectroscopic and kinetic. In the spectroscopic part the absorption cross-section and absorption high-resolution spectra are calculated using the information about vibrational levels populations of the molecules considered and gas temperature and pressure affected by vibrational relaxation kinetics. In its turn, the absorption cross-section data for pumping laser radiation serve as input information for kinetic calculations.

The principal features of the spectroscopic model are as follows:

- 1) line-by-line computation of high-resolution absorption spectra neglecting collision-induced line-interference; possibility of spectra smoothing using typical apparatus functions of variable width;
- 2) HITRAN-96 database (the previous version HITRAN-92 was described by Rothman et al., 1992) for absorption line parameters of 35 principal atmospheric molecules;
- 3) pressure- and temperature- dependent Voigt contour for individual absorption lines in approximation given by Matveev, 1972; collisional halfwidths are calculated accounting for both air- and self-broadening;
- 4) Benedict [Winter et al., 1964] contour for CO₂ absorption line wings (up to ±25 cm⁻¹ from the line center);
- 5) water vapor continuum absorption CKD model [Clough et al., 1989] extended to nonequilibrium conditions in the region from 0 to 5000 cm⁻¹;
- 6) N₂ and O₂ collision-induced continuum absorption in 2080-2740 cm⁻¹ and 1365-1800cm⁻¹ regions respectively [Thibault et al., 1997; Kneizys et al., 1988];
- 7) six conventional season-latitude atmospheric models [Anderson et al, 1988, De Bievre et al., 1984] containing typical vertical distributions of total pressure, temperature and concentrations of 32 principal gases in altitude range from 0 to 120 km.

Vibrational kinetics model for IR laser excitation and collisional relaxation processes in air (N₂-O₂-H₂O-CO₂ mixture) includes:

- 1) laser pumping of selected vibrational transitions of CO₂ and H₂O by multifrequency radiation of variable spectral composition;
- 2) quasi-stationary approximation for rotational sublevels populations (this allows to model accurately the effect of entire absorption band saturation taking into account collisional rotation- translational (RT-) relaxation [Chugunov et al., 1985]);

- 3) time-dependent rate equations for the populations of 13 vibrational levels of CO₂, N₂, H₂O and O₂ accounting for VV-, VV'-, VT- collisional relaxation processes ([Britan and Starik, 1980; Taylor and Bitterman, 1964; Blauer and Nickerson, 1974], see **Fig. 3.3** and **Table 3.7**);
- 4) time-dependent equation for gas-kinetic temperature taking into account temperature dependencies of absorption cross-sections and vibrational relaxation rate constants (see **Table 3.7**);
- 5) ideal gas isochoric law for pressure rise effect.

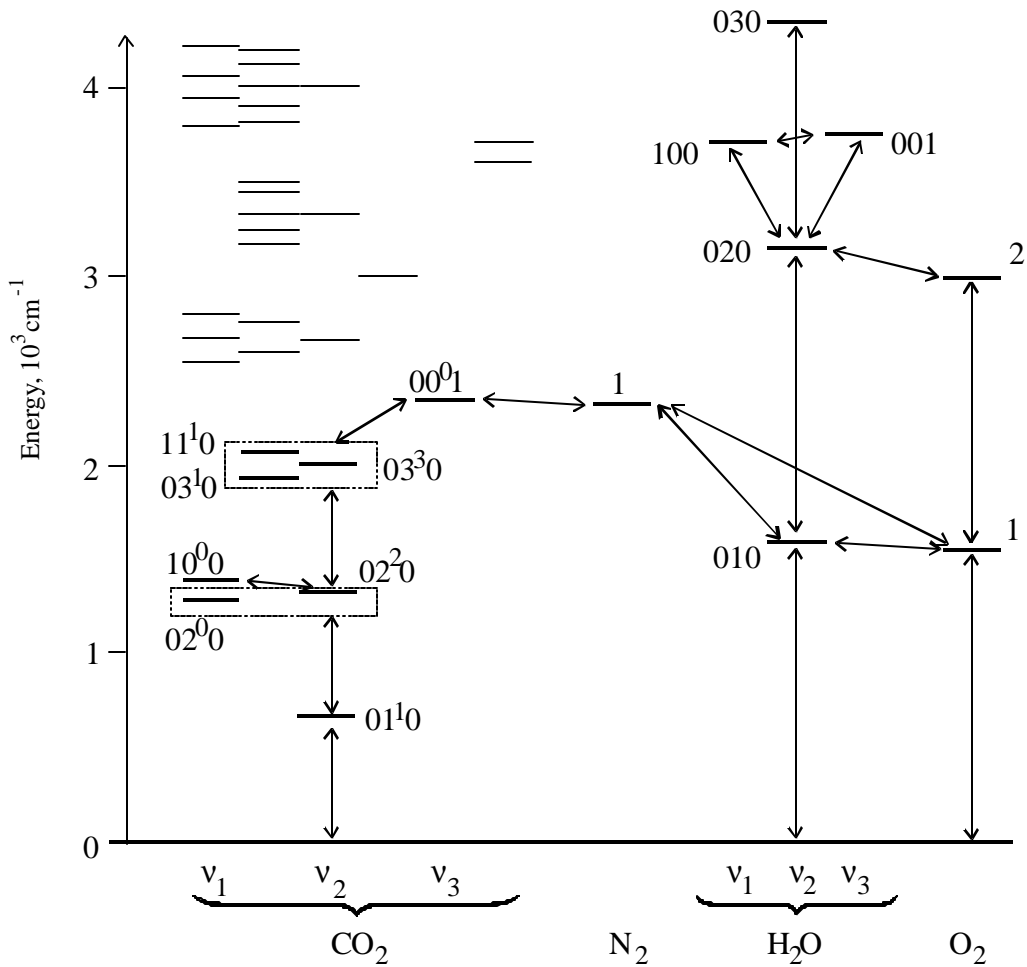


Fig. 3.3. Vibrational levels of principal atmospheric molecules included into collisional relaxation kinetics model (thick lines). The levels in dashed boxes are assumed to be of equal vibrational temperature.

3.2.1. Main equations of theoretical model

Let us consider molecular gas interacting with radiation. Rate equations for molecular vibration-rotational levels populations of lower $|v-1\rangle$ and upper $|v\rangle$ vibrational states coupled by laser radiation are as follows

$$\frac{dn_{v-1}^i}{dt} = -W_{v-1,v}^i n_{v-1}^i + W_{v,v-1}^i n_v^i + \frac{1}{t_{RT}} (N_{v-1} q_{R_{v-1}}^i - n_{v-1}^i),$$

$$\frac{dn_v^i}{dt} = +W_{v-1,v}^i n_{v-1}^i - W_{v,v-1}^i n_v^i + \frac{1}{t_{RT}}(N_v q_{R_v}^i - n_v^i)$$

$$W_{v,v-1}^i = \frac{g_{v-1}^i}{g_v^i} W_{v-1,v}^i, \quad W_{v-1,v}^i = \frac{S_{v-1,v}^i I(t)}{\hbar W_{v-1,v}^i}, \quad q_{R_v}^i = g_v^i \exp\left(-\frac{E_{R_v}^i}{k_B T}\right) / Q_R(T),$$

$$S_{v-1,v}^i = \frac{g_v^i}{g_{v-1}^i} \frac{c^2 p^2 A_{v,v-1}^i}{(W_{v-1,v}^i)^2} G(W - W_{v-1,v}^i), \quad A_{v,v-1}^i = \frac{64p^4}{3hc^3} \frac{(n_{v-1,v}^i)^3}{g_v^i} |\dot{a}| |\mathbf{R}_{lu}|^2$$

Here w and $I(t)$ are laser radiation frequency and time-dependent intensity; $W_{v-1,v}^i = 2pn_{v-1,v}^i$, $W_{v-1,v}^i$ and $S_{v-1,v}^i$ are the line center, laser excitation rate and corresponding absorption cross-section of molecular vibration-rotational transition i in $|v-1\rangle \otimes |v\rangle$ band; $g_{v-1}^i, g_v^i, E_{R_{v-1}}^i, E_{R_v}^i$ and $q_{R_{v-1}}^i, q_{R_v}^i$ are total statistical weights, rotational energies and rotational population Boltzmann factors; $A_{v,v-1}^i$ is the first Einstein coefficient for the transition i ; T - translational (gas-kinetic) temperature; $Q_R(?)$ is rotational partition function; N_{v-1}, N_v are total populations of vibrational levels; $G(W - W_{v-1,v}^i)$ is normalized spectral shape of absorption line being Voigt function in general case; t_{RT} is rotational-translational relaxation time; c - speed of light, k_B and $\hbar=h/2p$ - Boltzmann and Planck constants. In the last formula (the first Einstein coefficient for degenerate transition) the indexes "l" and "u" used in summation denote lower and upper M-sublevels coupled by radiation, $|\mathbf{R}_{lu}|$ is matrix element of $|\mathbf{l}'\rangle \otimes |\mathbf{u}'\rangle$ transition dipole moment [Penner, 1963].

The total statistical weights are the following products $g_k^i = g_I \times g_{vk} \times g_{Rk}^i$ with $k = v, v-1$, where g_{vk} is vibrational degeneracy of state k ; $g_{Rk} = 2J_k + 1$ is rotational degeneracy factor, J_k is rotational quantum number of angular momentum for vibrational state k ; g_I - nuclear spin degeneracy factor whose value for $H_2^{16}O$ molecule is $g_I = 2 - (-1)^{|t|}$, $t = K_a - K_c$, where K_a, K_c -rotational quantum numbers of the projections of angular momentum.

We use the following commonly used pressure and temperature dependence of collision- broadened halfwidth of absorption line $g = g^0 \times p \times [296/T]^n$ with g^0 and n taken from HITRAN-96. Rotational relaxation times for both H_2O-N_2 and CO_2-N_2 collisions are assume to be equal to $pt_R=0.12 \cdot 10^{-8}$ s atm.

Vibrational populations are described by following kinetic equations

$$\frac{dN_v}{dt} = \sum \frac{\alpha dN_v}{dt} \frac{\ddot{\theta}_w}{\ddot{\theta}_w} + \sum \frac{\alpha dN_v}{dt} \frac{\ddot{\theta}_{vv}}{\ddot{\theta}_{vv}} + \sum \frac{\alpha dN_v}{dt} \frac{\ddot{\theta}_{vv'}}{\ddot{\theta}_{vv'}} + \sum \frac{\alpha dN_v}{dt} \frac{\ddot{\theta}_{vr}}{\ddot{\theta}_{vr}}$$

The terms in right-hand part of this equation correspond to laser excitation, $VV-$, VV' - and VT -relaxation processes. Vibrational levels of principal atmospheric molecules (N_2, O_2, H_2O, CO_2) included into present kinetics model are shown in **Fig. 3.3**. Corresponding relaxation terms are modeled in conventional manner neglecting multiquantum collisional processes. Laser excitation term accounts for only stepwise single-photon transitions as follows

$$\sum \frac{\alpha dN_v}{dt} \frac{\ddot{\theta}_w}{\ddot{\theta}_w} = W_{v-1,v} N_{v-1} - W_{v,v-1} N_v - W_{v,v+1} N_v + W_{v+1,v} N_{v+1}$$

The probabilities per unit time (rates) of stimulated absorption and emission for $|v-1\rangle \langle v|$ and $|v\rangle \langle v+1|$ vibrational transitions accounting for their rotational structure were obtained in quasi-stationary approximation for rotational populations (see, for example, Chugunov et al., 1985).

$$\begin{aligned} W_{v,v-1} &= \dot{a} \frac{q_{R_v}^i W_{v,v-1}^i}{1 + (W_{v-1,v}^i + W_{v,v-1}^i)t_R}, \quad W_{v-1,v} = \dot{a} \frac{q_{R_{v-1}}^i W_{v-1,v}^i}{1 + (W_{v-1,v}^i + W_{v,v-1}^i)t_R} \\ W_{v,v+1} &= \dot{a} \frac{q_{R_v}^i W_{v,v+1}^i}{1 + (W_{v,v+1}^i + W_{v+1,v}^i)t_R}, \quad W_{v+1,v} = \dot{a} \frac{q_{R_{v+1}}^i W_{v+1,v}^i}{1 + (W_{v,v+1}^i + W_{v+1,v}^i)t_R} \end{aligned}$$

Calculation of monochromatic absorption coefficient is made with the assumption of the possibility of rotational saturation as follows

$$a_{v-1,v}^i(n) = s_{v,v-1}^i(n) D n_{v-1,v}^i = \frac{N_{v-1} q_{R_{v-1}}^i - N_v q_{R_v}^i}{1 + \frac{g_v}{g_{v-1}} \frac{\partial}{\partial} W_{v,v-1}^i t_{RT}}$$

Normalized spectral shape of absorption line ($\int_0^\infty G(n - n_{v-1,v}^i) dn = 1$) is expressed as the Voigt

function in Matveev approximation [Matveev, 1972]

$$\begin{aligned} G(n - n_0) &= \frac{1}{g_v} \left\{ 0.46971864 \times (1 - x) \times e^{-y^2 n^2} + \right. \\ &+ 0.31830989 \times \frac{x}{1 + y} - x \times (1 - x) \times (3.1640426 + x) \times \frac{0.066 \times e^{-y \times 0.4}}{y(y - 5.5) + 40} \times \frac{\partial u}{\partial p} \\ &\quad \left. x = \frac{g_L}{g_v}; \quad y = \frac{a n - n_0}{g_v} \frac{\partial}{\partial}; \quad g_v = a + 0.05 g_L \frac{a}{e} 1 - \frac{g_L}{a} \frac{\partial}{\partial}; \right. \\ &\quad a = 0.5 \times \frac{g_L}{e} + \sqrt{g_L^2 + 4 g_D^2} \frac{\partial}{\partial}; \quad g_D = 3.581157 \times 10^{-7} n_0 \sqrt{\frac{T}{m}}; \quad g_L = g^0 \times \frac{296}{e} \frac{\partial}{\partial} n \end{aligned}$$

Here m is the mass of molecule. All spectroscopic parameters of absorption lines were taken from HITRAN database. Rotational partition functions are calculated using formulae (see, for example, [Herzberg, 1945])

$$Q_R = \frac{kT}{S \cdot h c B} \times S \quad \text{for linear molecules (e.g., CO, CO}_2)$$

$$Q_R = \frac{1}{S} \sqrt{\frac{p}{A \times B \times C} \frac{a k T \frac{\partial}{\partial}^3}{h c \frac{\partial}{\partial}}} \times \exp \left(\frac{a h c}{4 k T} \sqrt{B \times C} \frac{\partial}{\partial} \right) \times S \quad \text{for top-like molecules (e.g., H}_2\text{O, O}_3).$$

Here A, B, C are rotational constants of molecule considered. Symmetry number σ takes different values: $\sigma = 1$ for molecules of $C_{\frac{1}{2}v}$ point group, and $\sigma = 2$ - for molecules of $D_{\frac{1}{2}h}$ groups. The value of $\frac{\partial}{\partial}$ is defined by spins of atoms, forming the molecule: $S = \sum_m (2I_m + 1)$, where I_m - spin of m -th nucleus (note that for the principal isotopes $I_C = 0; I_H = 1/2; I_N = 1/2; I_O = 0$). For example, for $H_2^{16}O \quad S = 4$ and $\sigma = 2$.

3.2.2 Multifrequency radiation

Our computational model allows us studying the processes of gas mixture excitation by laser radiation with complex spectrum. Emission spectrum is modeled by a series of arbitrary spaced monochromatic lines with specified intensity positioned in arbitrary wavenumber interval. Spectral distribution of radiation intensity is assumed to be constant during the time of action, while the integral intensity may vary. The main computational problem in operation with complex spectrum is a rapid increase of calculations with a rise of number of spectral lines considered. We use the method in which the computer code 1) scans the HITRAN database before time-dependent calculations and selects all lines relevant to the chosen bands, 2) calculates the parameters of absorption and non-linear interaction for these lines, and 3) finally forms the compact index which serves to retrieve the data for all influencing lines of multifrequency radiation for a given absorption line in a course of time-dependent calculation.

3.2.3 Gas-dynamic model

The heat release due to absorption of the radiation by gas is determined by the following equation

$$Q = \dot{\alpha} a_i(n_i) I_i - \dot{\alpha} R_j E_j$$

where i is the number of radiation line, R_j is the production rates of j - component (a molecule on a certain vibrational level), E_j is energy of formation of j - component. The rates of vibrational collisional relaxation are defined as follows:

$$R_i = - \dot{\alpha} k_{jk}^{lm} \frac{e}{\epsilon} N_j N_k - \exp \left(\frac{\alpha}{\epsilon} \right) \frac{D e_{jk}^{lm}}{kT} \frac{\dot{\alpha}}{\sigma} N_l N_m +$$

$$D e_{jk}^{lm} = E_j + E_k - E_l - E_m ,$$

Here N_j is number density of j - component, $k_{jk}^{lm}(T)$ are collisional relaxation rate constants.

The gas temperature and pressure due to heat release in the irradiated zone depend on a type of gas-dynamic process. Limiting cases are the isobaric heating, when heated gas has time to flow out from heated region, and isohoric heating taking place at a short time interval, when the gas spreading can be neglected. In all intermediate cases, the gas temperature T is obviously

$$T_a + \frac{1}{c_p} \int_0^t Q(t) dt \leq T \leq T_a + \frac{1}{c_v} \int_0^t Q(t) dt$$

where c_p and c_v are, respectively, the specific heat at constant pressure and density, $Q(t)$ is local heat release, T_a is ambient gas temperature. Because vibrationally excited molecules are considered here as separate components and rotational degrees of freedom are in thermal equilibrium (except for a small fraction of components, which belongs to optically active bands), the specific heats do not depend on the temperature and differ from each other about 1.4 times. So, all the temperature variations due to different heating conditions are confined to the narrow interval $\pm 20\%$. Gas density can vary in essentially wider range (is constant or reduce several times). The importance of an adequate gas-dynamic model is seen from aforesaid.

However, one should note, that, in fact, the density distribution in the irradiated region is affected by gas motion due to external causes (buoyancy driven convection, relative travel of radiation beam and gas volume, etc.). Taking these factors into account will involve into consideration many additional parameters describing the intensity distribution across the beam, gravity direction and ambient gas velocity. All of those can affect the result in a comparable extent. Thus, to make the results of present work more general, we adopt the simplest model of isochoric heating:

$$c_v \frac{dT}{dt} = \sum_i \dot{\alpha} a_i (n_i) I_i - \sum_j \dot{\alpha} R_j E_j$$

$$p = kT \dot{\alpha} N_j$$

This model is rather realistic at a time of radiation action less than the time of sound propagation across the characteristic dimension of irradiated region, e.g., for laser beam radius of 0.3 m the admissible pulse time is about 1 ms.

3.3. Simulation of nonlinear absorption

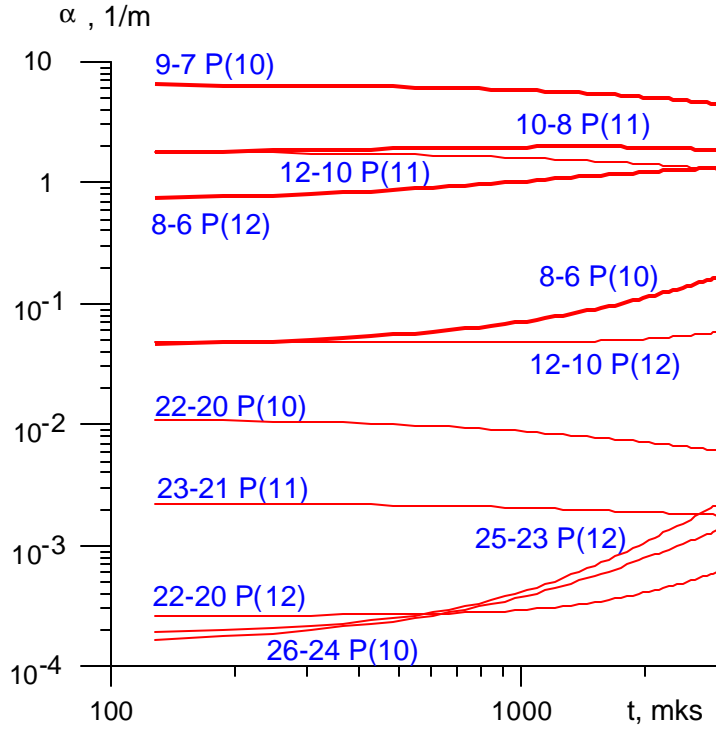


Fig. 3.4. Temporal evolution of atmospheric absorption coefficients for selected ro-vibrational emission lines of FO CO laser. Constant radiation intensity 10 kW/cm^2 is assumed for typical FO CO laser spectrum (see Fig.3.2d). Conditions of tropical atmospheric model at altitude $H=0 \text{ km}$ are used. Continuum absorption is neglected. Thick curves correspond to FO CO laser lines possessing significant relative intensity in the spectrum shown in Fig.3.2d.

The computations of nonlinear absorption of FO CO multifrequency radiation were performed with using typical FO CO laser output spectrum (see **Fig. 3.1,d**) for the conditions of tropical atmosphere (model No 1 [Anderson et al. 1988; De Bievre et al. 1984]) at altitudes $H=0$ and $H= 10 \text{ km}$. For $H=0 \text{ km}$ total pressure is 1 atm, temperature is 299.7 K; relative concentrations of principal absorbing gases are: $\text{H}_2\text{O} - 25900 \text{ ppmV}$, $\text{CO}_2 - 330 \text{ ppmV}$; for $H=10 \text{ km}$ total pressure is 0.282 atm, temperature is 237 K; relative concentrations are: $\text{H}_2\text{O} - 191 \text{ ppmV}$, $\text{CO}_2 - 330 \text{ ppmV}$. Only main isotopes of molecules are taken into account in nonlinear absorption computations.

Fig. 3.4 illustrates temporal evolution of absorption coefficients in selected FO CO laser lines showing significant change of relative absorption. For some lines the absorption increases while in other decreases. The analysis showed that this effect is mainly caused by simple laser heating of air (in the case considered the temperature at $t = 3 \text{ ms}$ achieves 548 K). Such heating will lead to marked deformation of FO CO laser spectrum in the course of beam propagation. Also the changes in refractive index will take place and, as a consequence, thermal blooming of laser beam will occur.

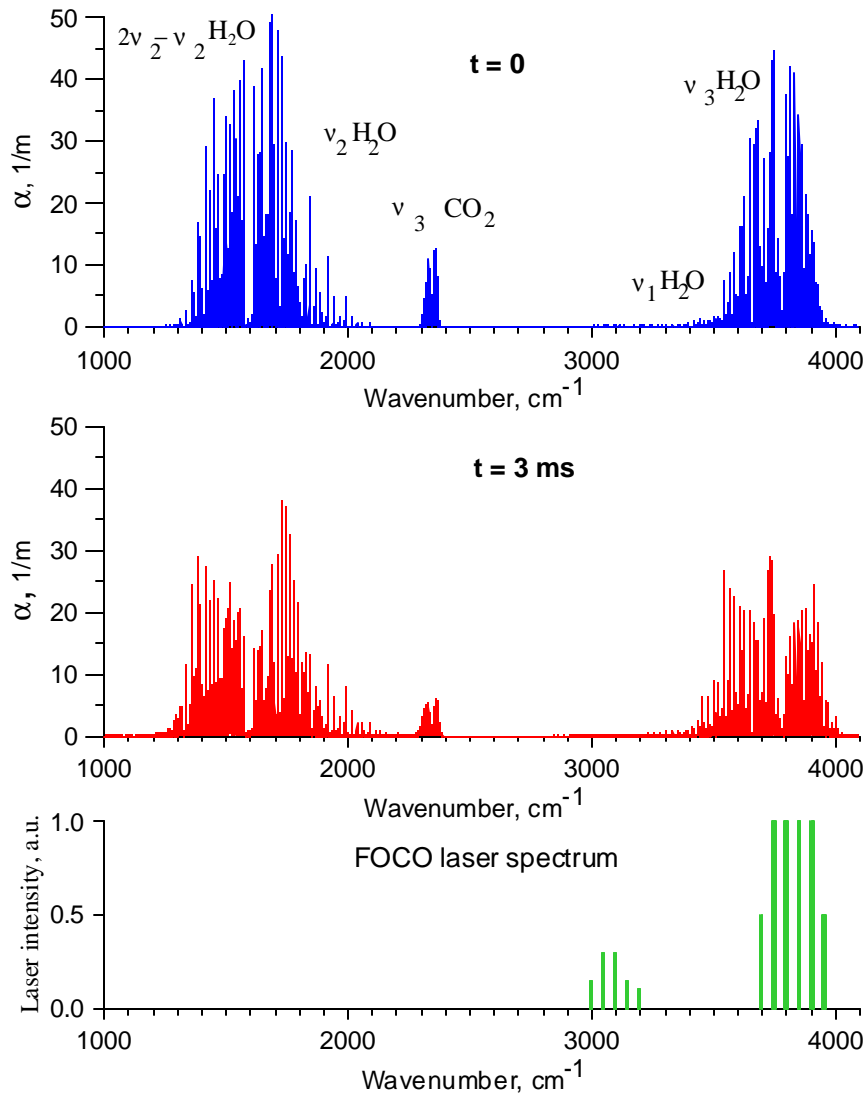


Fig. 3.5. Atmospheric absorption within 1000–4000 cm^{-1} region before ($t=0$) and after ($t=3$ ms) FO CO laser rectangular pulse action. Radiation intensity is 10 kW/cm^2 . Conditions of tropical atmosphere at altitude $H=0$ km are used. Continuum absorption is neglected. FO CO laser spectrum without rotational structure is shown at the bottom.

Several examples of nonlinear absorption spectra of FO CO laser radiation in different atmospheric conditions are presented in **Figs. 3.5, 3.6**. FO CO laser spectrum used in simulation is absorbed mainly by v_3 band of H_2O . Note that only high-frequency group of laser lines (3680 – 3960 cm^{-1}) interacts efficiently with this band. It is clear from **Fig. 3.5** that FO CO laser action upon water vapor results not only in decrease of absorption (laser "bleaching") but also in its increase (laser-induced absorption). Marked decrease (up to 3 times) of the absorption takes place in the spectral regions around the centers of v_2 and v_3 bands of H_2O ($\approx 1600 \text{ cm}^{-1}$ and 3800 cm^{-1}) as well as in v_3 band of CO_2 . Significant absorption increase caused by laser heating takes place for many lines (e.g., up to several tens times for weak lines). It is natural that temperature changes in air absorption reveal themselves not only in the spectral interval of pumping laser radiation but also in distant spectral regions. Good example is a marked decrease of absorption in v_3 CO_2 band centered at 2349 cm^{-1} ($\lambda=4.3 \mu\text{m}$). Complex changes of absorption also occur

in 1200-2200 cm⁻¹ spectral region (decrease and "blue" shift of absorption in ν_2 H₂O band region, increase and "red" shift of absorption in the region of $2\nu_2 - \nu_2$ H₂O band).

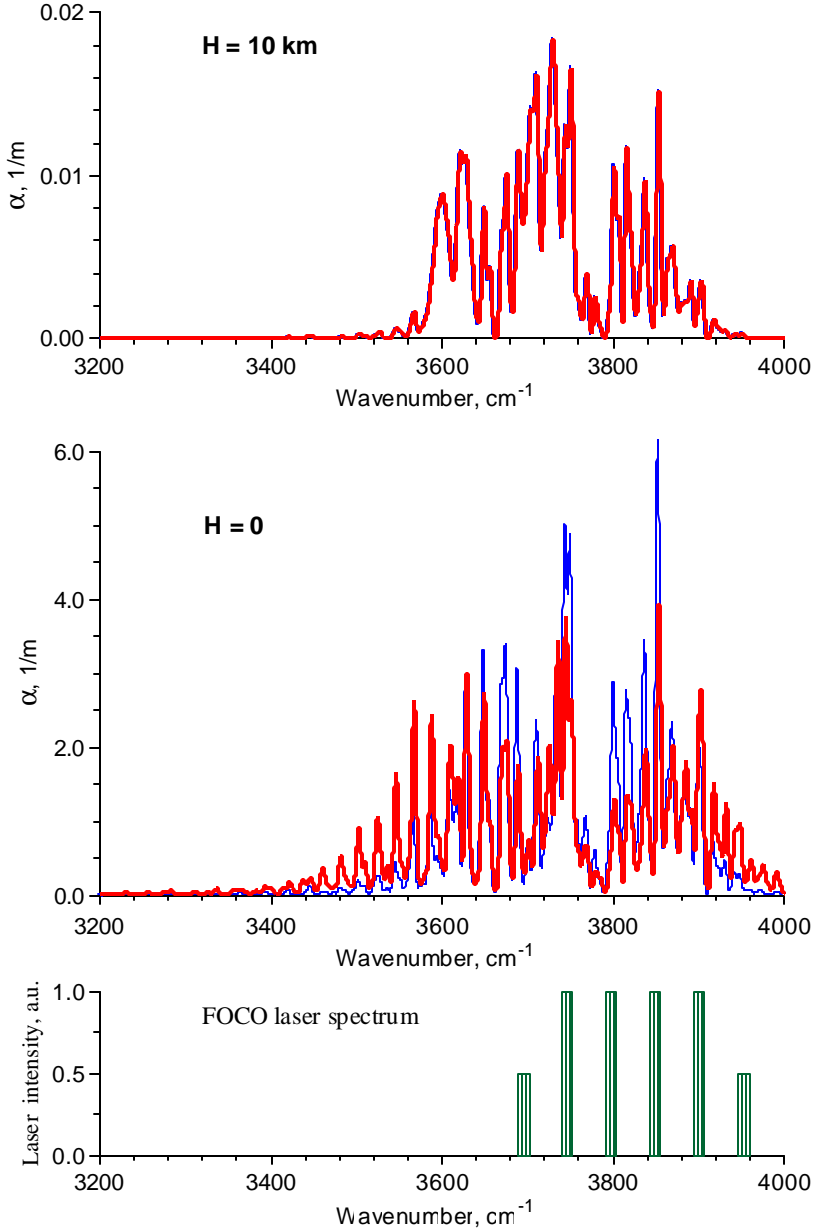


Fig. 3.6. Atmospheric absorption spectra before ($t=0$, thin line) and after ($t=3$ ms, thick line) FO CO laser rectangular pulse action for different altitudes ($H=0$ km and $H=10$ km). Radiation intensity is 10 kW/cm². Conditions of tropical atmosphere at altitude $H=0$ km are used. Continuum absorption is neglected. Spectra are smoothed; apparatus contour width is 5 cm⁻¹. FO CO laser spectrum without rotational structure is shown at the bottom.

Altitude dependent changes of atmospheric water vapor absorption in 3200-4000 cm⁻¹ region caused by the action of FO CO laser radiation are shown in **Fig. 3.6**. It is seen that laser-induced changes of air absorption depend on altitude. Namely, at $H=0$ marked laser induced bleaching and absorption increase take place, however, at $H=10$ km the changes in spectrum are negligible (air temperature is

practically constant). This fact is explained by rapid decrease of water vapor absorption with altitude related with concentration decrease.

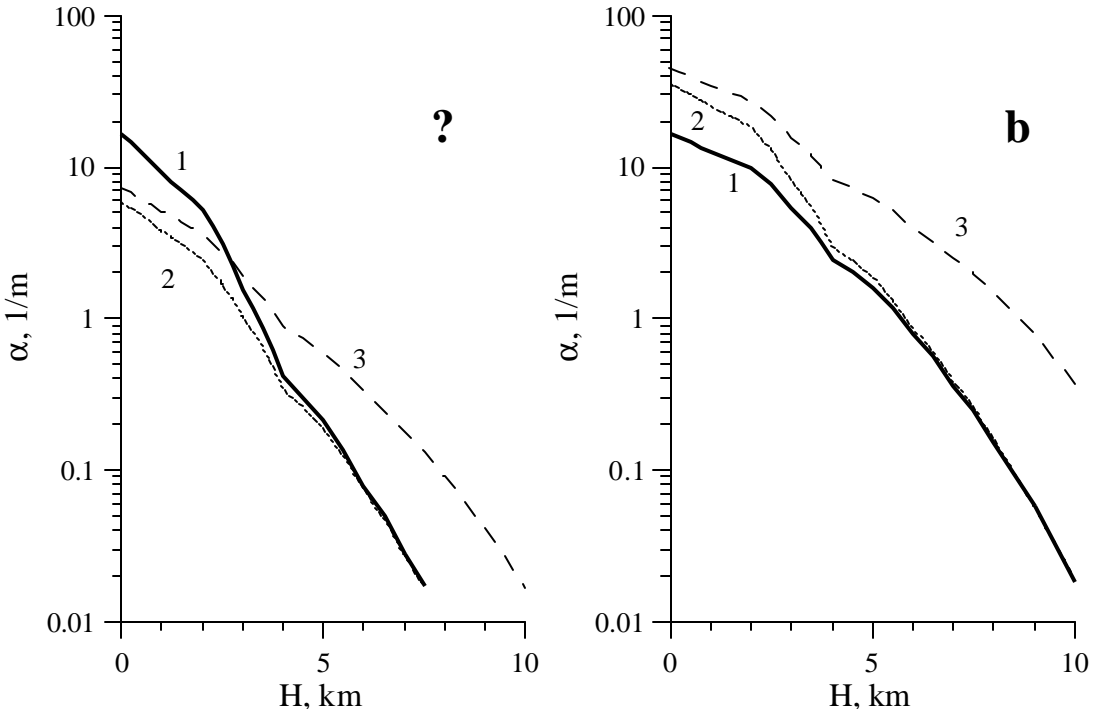


Fig. 3.7. Altitude profiles of absorption coefficient in tropical atmosphere on sounding laser frequencies 3546.9 cm^{-1} (a) and 3752.2 cm^{-1} (b) under the action of intense FOCO laser radiation (line 8-6 R(21), $n = 3853.9633 \text{ cm}^{-1}$) on atmospheric water vapor. Intensity of laser radiation $I = 1 \text{ MW/cm}^2$, pulse duration $1 \mu\text{s}$. Continuum absorption is taken into account. 1 - an account of absorption saturation and temperature rise due to laser heating; 2 - an account of only absorption saturation (air temperature in laser beam is assumed to be constant equal to ambient temperature at the considered altitude); 3 - linear absorption only ($I = 0$).

Laser-induced changes in atmospheric absorption strongly depend on the spectral composition of FOCO laser radiation. The calculations performed for FOCO "red-shifted" spectrum covering transmission window (see **Fig. 3.1,e**) showed that the changes in atmospheric absorption spectrum are much less than those presented in **Figs. 3.5, 3.6**. However, certain influence of radiation on air absorption takes place. This is mainly due to the pumping ν_3 band of H_2O by FOCO laser lines with $\nu > 3600 \text{ cm}^{-1}$.

Note that all mentioned phenomena are caused in the cases considered by laser heating. It is interesting to discuss another type of laser-induced changes IR radiation attenuation in the atmosphere caused both by laser heating and saturation of pumping radiation absorption. The joint influence of these phenomena reveals itself on small time scales under large enough intensities of laser radiation. High peak intensity and small pulse duration can be achieved in the case of mode-locked lasing. **Fig. 3.7** presents altitude profiles of absorption coefficient for two sounding frequencies 3546.9 cm^{-1} (a) and 3752.2 cm^{-1} (b) in the conditions of ν_3 H_2O pumping by short and intensive pulse of FOCO laser radiation. Air heating caused by the absorption of pumping beam decreases with altitude growth (at the altitude $H=0 \text{ km}$ the temperature reaches 490 K , while when $H > 7 \text{ km}$ the heating becomes small). The effect of absorption saturation becomes stronger as the altitude increases because of increasing the absorption cross section at pumping frequency considered and increasing the collisional relaxation time of H_2O levels. At sounding frequency 3546.9 cm^{-1} the absorption grows with the growing of temperature, whereas at 3752.2 cm^{-1} it falls. Note that the effect of saturation of pumping radiation absorption reduces the absorption at both

sounding frequencies. All these facts explain a behavior of $\alpha(H)$ dependence shown in **Fig. 3.7**. In particular, it becomes clear, why $\alpha(H)$ profile in the case (b) turns out to be as a whole more flat than in the case (a).

3.4. Experiments on absorption of FO CO laser radiation by gaseous substances

The spectral range of FO CO laser overlaps with absorption spectra of numerous atmospheric pollutants and natural gases. Only small portion of these substances is listed in **Table 3.8**. Most of them are caused by human activities. Their impact on vegetation, animals and people is very harmful. Maximum allowable exposures as well as optimum spectral regions suitable for detection of each substance are indicated in **Table 3.8**. From the other hand the spectrum of FO CO laser within wavelength range of 3.3–4.2 μm coincides with the atmospheric transparency window (**Fig. 3.8**). Both of these features of FO CO laser spectrum give the opportunity of effective usage of the laser for the purpose of laser remote gas analysis.

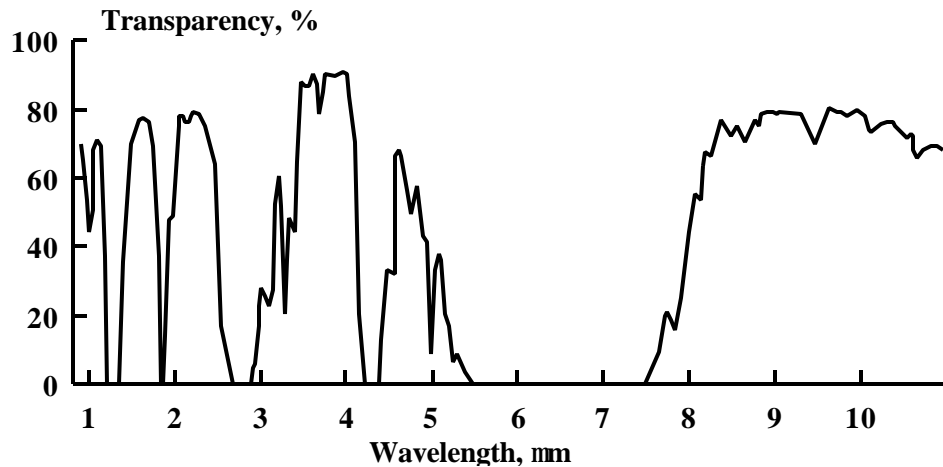


Fig. 3.8. Transparency of the atmosphere for 1 mile length trace (Measures, 1984).

The necessary step before the spectroscopic gas analysis consists in determination of absorption cross sections by considered substance at particular laser frequencies applied. At present, there are many absorption data related with organic substances. However, most of them were obtained with low spectroscopic resolution; in most cases it is hard to rescale these data to another pressures and temperatures; there are noticeable discrepancies between data (Meyer and Sigrist, 1990; Thöny and Sigrist, 1990). Therefore, the measurements of absorption of different substances for particular conditions are of great importance.

3.4.1. Experimental facility

Spectroscopic experiments were carried out on cryogenically cooled e-beam sustained discharge FO CO laser. The detailed description of the installation is presented above (see **Part I**) and in [Basov et al, 1999a-d; Ionin et al, 1998a-d, 1999]. Two gas cells were prepared for the study of FO CO laser radiation absorption in gaseous substances. Both of them are of cylindrical form and made of stainless steel. The first gas cell is of 60 mm inner diameter and 200 cm length. Output windows (BaF_2 flats of 80 mm in diameter) were attached directly to the ends of the cell. This cell was designed to study the laser radiation absorption in gases at pressures from 0.05 up to 3 bar and temperatures from ~300 up to 400 K. For this purposes the cell had vacuum-pressure measuring device and full-length heater. The second Brewster angled cell (30mm inner diameter and 10cm length) was prepared for the study of laser radiation absorption in vapors using intra- or extra-cavity techniques. The multifrequency FO CO laser radiation was directed to 10 cm

long absorption cell to measure its absorption in organic vapor (acetone, ethanol etc.). The spectral characteristics of the absorption were measured by using homemade spectrum analyzer using diffraction grating (200 grooves per mm) and thermovision apparatus. The visualized and digitized spectrum of the FO CO laser radiation was compared with the spectrum passed through the vacuum pumped cell and the cell filled by saturated vapor of organic substances at room temperature ~ 286 K.

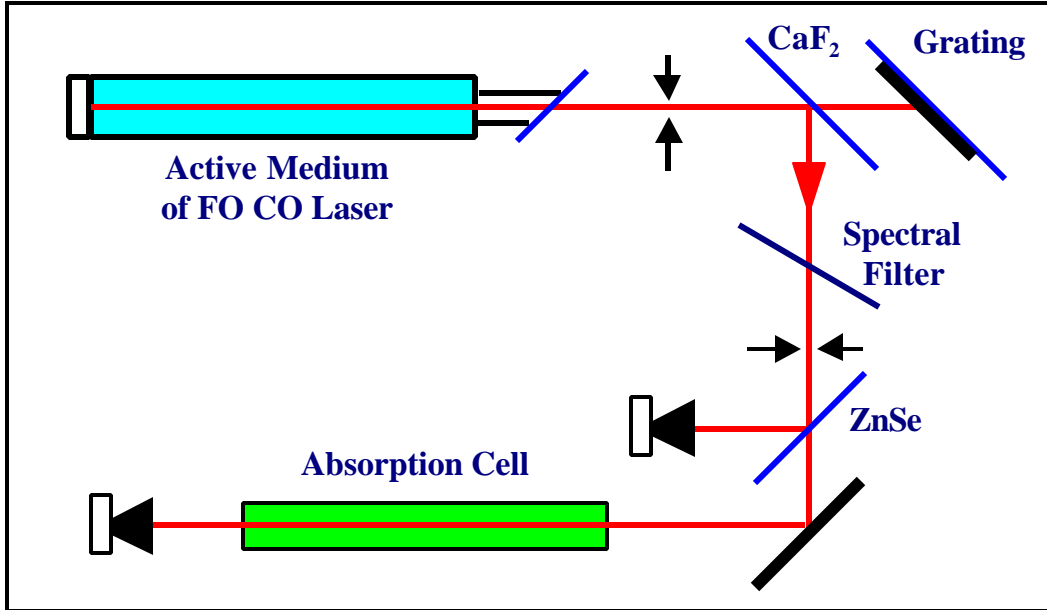


Fig. 3.9. Optical scheme of the experiments with 2 m long absorption cell.

The optical scheme of the experiments with the 2 m long absorption cell is presented in **Fig. 3.9**. The single line FO CO laser resonator (~ 3 m length) consisted of the rear spherical mirror (radius of curvature 10 m) and the diffraction grating (420 grooves per mm) operating in Littrow configuration. The intracavity diaphragm with 30 mm aperture in diameter was used in the experiments. The alignment of the laser resonator was done by using 650 nm semiconductor laser. To change the spectrum line of the laser output, the grating was rotated at the certain angle that was measured by means of auxiliary 650 nm laser at the distance ~ 4 m from the grating. The CO laser radiation was extracted from the resonator through its Fresnel reflection ($\sim 5\%$) from CaF_2 intracavity flat. To reduce the intensity of $5\mu\text{m}$ FB emission, the laser beam was passed through the spectral filter made of fused silica (~ 0.5 mm thickness; spectral characteristics of the filter was presented in (Basov et al, 2000a)). To measure the energy of the laser pulse at the entrance of the cell $E(0)$, the part of the laser beam passed through the diaphragm (22 mm in diameter) was directed on a calorimeter by reflection from beamsplitter made of ZnSe. The second calorimeter measured the energy of the laser beam $E(L)$ passed through the absorption cell with the length L . The absorption coefficient g was calculated in accordance with Bouger law $E(L) = E(0) \exp(-gL)$ from the ratio of the values $E(0)$ and $E(L)$ measured for vacuum pumped cell (or cell filled by nitrogen at atmospheric pressure) and for cell filled with gaseous absorber.

The feasibility of photo acoustic spectroscopy for multicomponent gas analysis has been demonstrated in many papers (see for example (Meyer and Sigrist, 1990)). The photo acoustic spectroscopic study of the FB CO laser absorption in atmospheric gases using our CO laser installation see in (Ageev et al, 1989). The photo acoustical system was manufactured and prepared especially for the experiments. The photo acoustical cell is schematically presented in **Fig. 3.3** and consisted of cylindrical acoustical resonator (length $L=0.32$ m, 30 mm-diameter) with high sensitive electrically polarized acoustic

microphone 2 integrated into cell's wall. The volume of the cell 1 may be filled by different gases and vapors at room temperature and different pressures (from several Torrs up to atmospheric). The system was prepared for the experiments with the laser pulse duration up to 500 μ s. This time was limited by build-up time for the first axial acoustic mode (\sim 1 ms) in acoustical resonator. The pressure pulse in the cell was formed due to relaxation of the absorbed laser energy in gas mixture. The membrane 4 detected the pressure pulse by changing the capacitance of the microphone 2. The polarized voltage up to 75 V was applied between highly polished electrode 5 and grounded membrane. The voltage was applied from external measuring system through the golden connector 3. The electrodes were separated by the isolated film of 40 μ m thickness 7. The flat electrode 5 has a set of holes to connect the volume between electrodes and ballasting volume with the reference pressure.

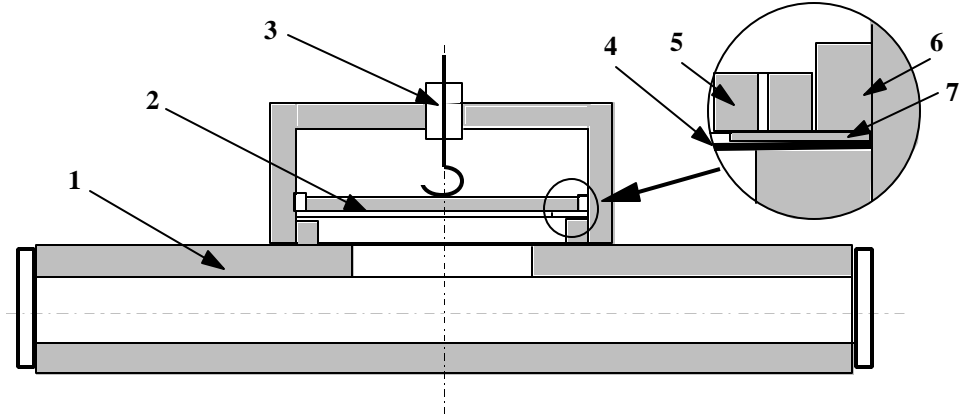


Fig. 3.10 Schematic of the photo acoustical cell.

- 1 - acoustical resonator with input and output windows made of CaF₂; 2 - microphone;
- 3 - golden cable connector; 4 - membrane;
- 5 - flat electrode of the microphone;
- 6 - hard isolator;
- 7 - isolator film 40 μ m thickness.

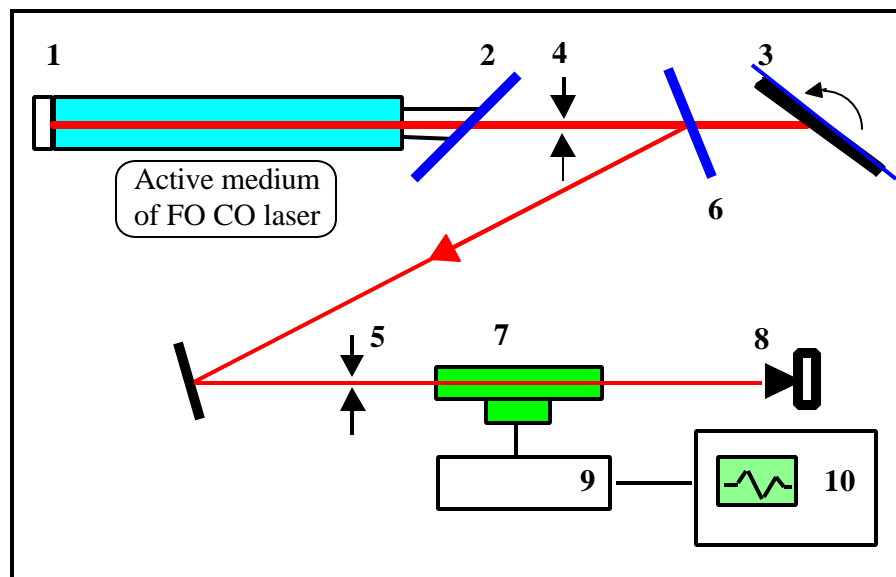


Fig. 3.11. Optical scheme of the experiments with photo acoustical cell.

- 1 - active medium of the FO CO laser with rear mirror;
- 2 - output window;
- 3 - diffraction grating (420 grooves per mm) in Littrow configuration;

4, 5 - diaphragms 30mm and 22mm, respectively; 6 - output coupler (CaF_2 flat);
 7 - photo acoustical cell; 8 - calorimeter; 9 - amplifier; 10 - oscilloscope.

Optical scheme of the photo acoustic measurements is presented in **Fig.3.11**. These experiments were carried out by using FO CO laser facility described above. The density of the laser mixture was chosen to satisfy the requirement of FO CO laser pulse duration being less than 500 μs . The laser pulse duration was about 300 μs under the experimental conditions $\text{CO:N}_2=1:4$, 0.3 Amagat, 100 K. FO CO laser output was directed into the photo acoustical cell 7 through the diaphragm 5 (~20 mm in diameter). The laser energy E was measured by calorimeter 8 installed behind the cell 7. The density of gaseous absorber inside the cell 7 was chosen to satisfy the requirement of small absorption ($gL \ll 1$). Electrical signal from the photo acoustical cell was amplified by the amplifier 9 and detected by the oscilloscope 10. Typical time behavior of FO CO laser pulse (1) and signal from photo acoustical cell (2) are presented in **Fig.3.12**. The first maximum of microphone signal U (2) was proportional to absorbed energy E_{ab} . The absorption coefficient g was calculated by following expression: $g \approx kU(EL)^{-1}$, where k is a cell constant depending on photo acoustical cell design.

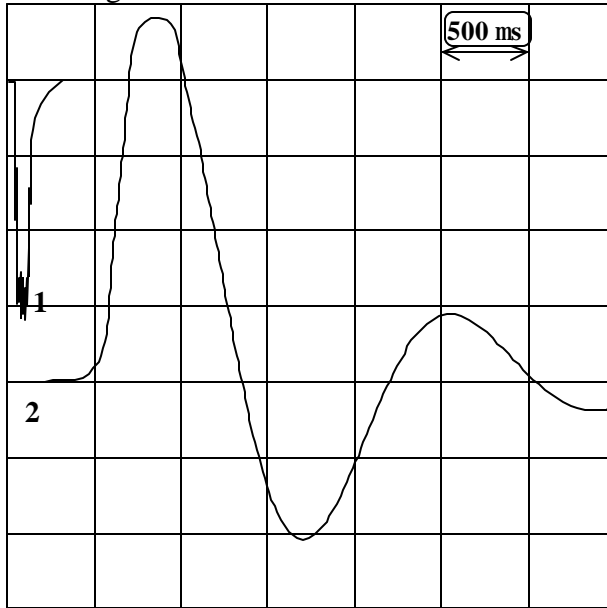


Fig. 3.11. Time history of FO CO laser pulse (1) and signal from photo acoustical cell (2).

3.4.2. Experimental results

The absorption cell of 10 cm length was used to measure absorption of FO CO laser radiation in organic vapors. **Fig.3.12** demonstrates spectral absorption of multiline FO CO radiation by ethanol and acetone vapor at the pressure ≈ 3.9 kPa and ≈ 17.3 kPa, respectively. One can see that ethanol (and acetone, respectively) maximum absorption lies within spectral intervals 3.29 - 3.52 μm and 3.77 - 3.84 μm (3.24 - 3.52 μm). These intervals correspond to 25→23 - 29→27 and 33→31 - 34→32 (24→22 - 29→27) FO CO laser vibrational bands. At the same experimental conditions absorption coefficients of ethanol and acetone on 24→22 P(16), 28→26 P(9) and 32→30 P(12) ro-vibrational lines of single-line FO CO laser corresponding to 3.25, 3.44 and 3.70 μm wavelengths, respectively, were measured (**Table 3.9**). The absorption coefficients were 0.06 cm^{-1} (3.25 μm), 0.20 cm^{-1} (3.44 μm) for ethanol and 0.16 cm^{-1} (3.44 μm) for acetone. Absorption coefficients for other spectral lines was less than

0.01 cm^{-1} . Various FO CO laser energy densities from 10 up to 50 mJ/cm^2 with pulse duration about 1.2 ms were used. Thus, FO CO laser can be used for observation and measurement of absorption by various gases and vapors.

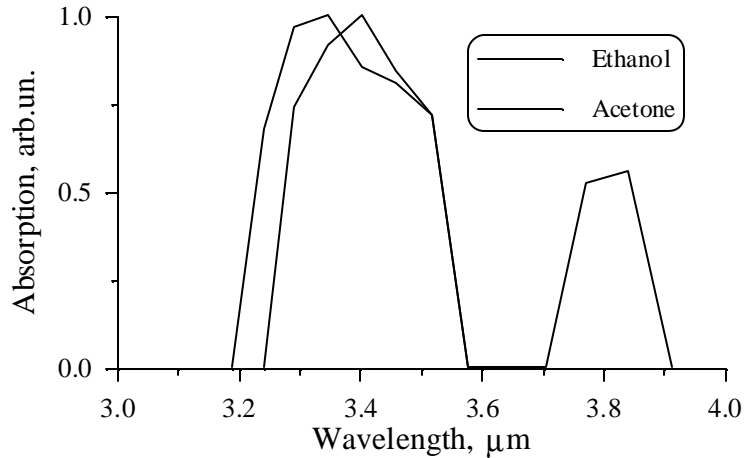


Fig.3.12. Spectral absorption of multiline FO CO radiation by ethanol and acetone vapor at gas pressure $\approx 3.9 \text{ kPa}$ and $\approx 17.3 \text{ kPa}$, respectively.

For different applications of FO CO laser it is very important identify laser transition correctly. The single-line FO CO laser can operate on more than 400 ro-vibrational transitions. Some of the spectrum lines corresponding to adjacent vibrational bands are very close. To identify the spectrum lines, we analysed the absorption of them in gaseous absorbers - in N_2O in particular. The molecule of N_2O is asymmetric three atomic molecule (Fig. 3.13) with well known spectral characteristics. The molecule has strong absorption within wavelength ranges $3.53\text{-}3.62 \mu\text{m}$ and $3.8\text{-}4.0 \mu\text{m}$. The set of analytical lines of FO CO laser in the latter spectral range is presented in Fig. 3.14. For example, the more detailed part of the diagram for two FO CO laser transitions $35\rightarrow33$ and $34\rightarrow32$ is presented in Fig.3.15. One can see that ro-vibrational lines near wavenumbers 2572 cm^{-1} and 2584 cm^{-1} are very close one to another: $35\rightarrow33\text{P}(8) 2571,61 \text{ cm}^{-1}$ and $34\rightarrow32\text{P}(21) 2571.67 \text{ cm}^{-1}$ ($\Delta\nu\approx0.06 \text{ cm}^{-1}$); $35\rightarrow33\text{P}(4) 2583,97 \text{ cm}^{-1}$ and $34\rightarrow32\text{P}(18) 2583.72 \text{ cm}^{-1}$ ($\Delta\nu\approx0.25 \text{ cm}^{-1}$). From the other hand, the absorption coefficients for the lines are very different. For example, at the left edge of the figure one can see absorption coefficient for ro-vibrational transition $34\rightarrow32 \text{ P}(21)$ (white bar) which is more than two times higher than for $35\rightarrow33 \text{ P}(8)$ (black bar).

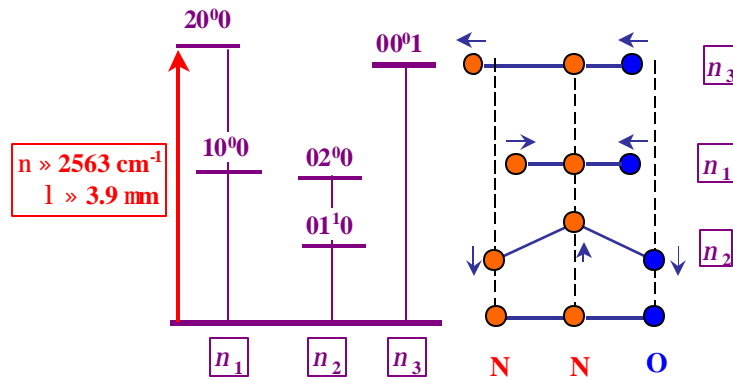


Fig. 3.13 Schematic structure of N_2O molecule (right) and its vibrational modes (left)

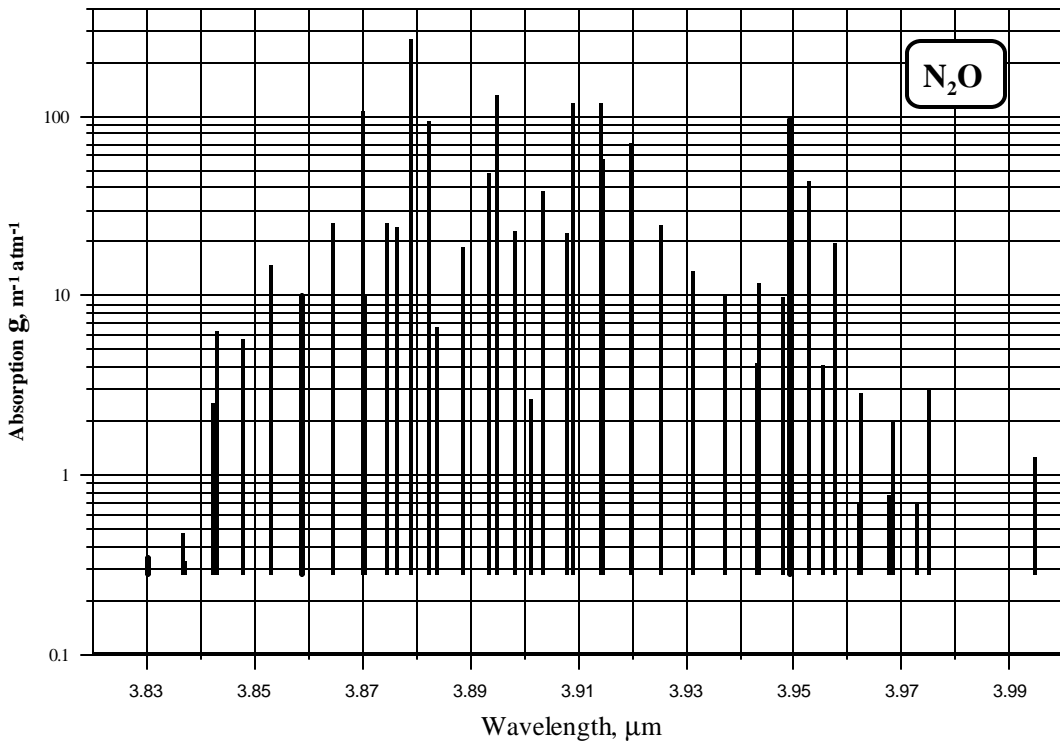


Fig. 3.14 N_2O absorption coefficient g [$\text{m}^{-1} \text{ atm}^{-1}$] for analytical spectral lines of FO CO laser within wavelength range $3.8\text{--}4.0 \mu\text{m}$.

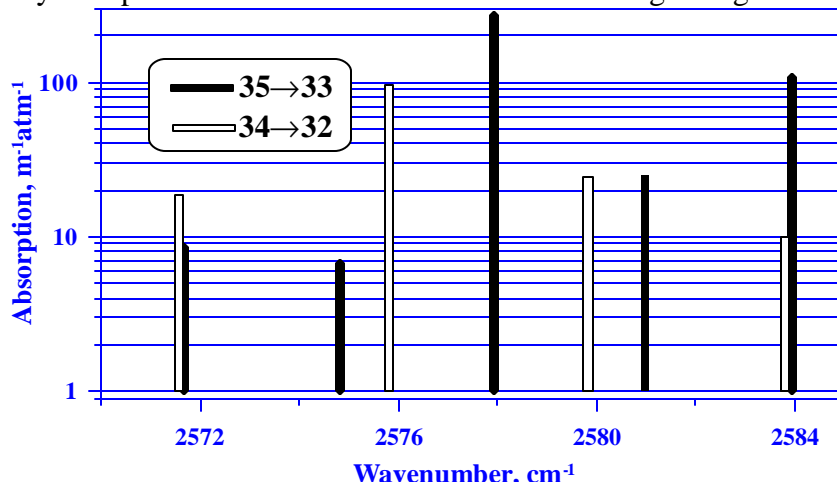


Fig. 3.15. N_2O absorption coefficient calculated for different FO CO ro-vibrational lines (transitions $35\rightarrow33$ and $34\rightarrow32$)

Linear absorption coefficients in $\text{N}_2\text{O:N}_2$ gas mixtures for several FO CO laser spectral lines (vibrational transition $35\rightarrow33$) were measured experimentally. The absorption cell of 2 m length filled by gas mixture N_2 and N_2O at atmospheric pressure was used. The absorption coefficient was determined as energy ratio of input and output FO CO laser pulses. As a result of the experiments, absorption cross-sections of N_2O were calculated and one can see a good agreement between theoretical and experimentally obtained data (**Fig. 3.16**). The same measurement of absorption was carried out for gas mixture $\text{CH}_4:\text{N}_2$ for spectrum lines corresponding to FO CO laser transitions: $28\rightarrow26\text{P}(12)$ $3.454 \mu\text{m}$ and $31\rightarrow29\text{P}(14)$ $3.646 \mu\text{m}$. Experimental data were also in a good agreement with theoretical ones.

For ro-vibrational line $35\rightarrow33 \text{ P}(13)$ it was obtained dependence of absorption coefficient g of gas mixture $\text{N}_2\text{O:N}_2$ on mixture pressure p (**Fig.3.17**) at the constant pressure of N_2O fraction (0.01 atm). One

can see that g increases with pressure growing. It can be explained by changing of absorption line profile due to collisional broadening which is changed for various pressures p_1 and p_2 (see **Fig.3.18**).

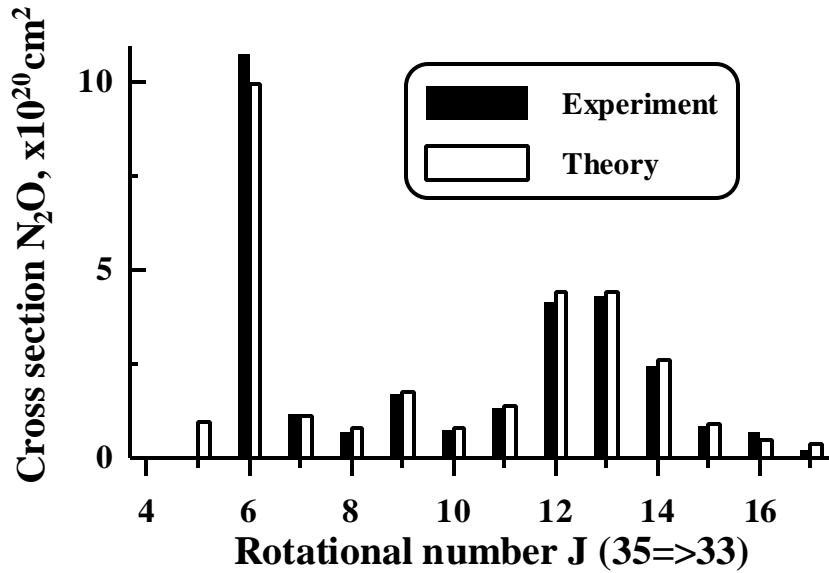


Fig. 3.16. N₂O absorption cross-sections for several FO CO laser spectral lines (vibrational transition 35→33)

The photo acoustic system described above was tested in our experiments. The absorption cross-sections of N₂O (gas mixture N₂O:N₂ = 1:100 at atmospheric pressure) obtained for several FO CO laser spectral lines (vibrational transition 35→33) are in good agreement with theoretical data (**Fig. 3.19**). The good agreement between theoretical and experimentally obtained data (see **Fig. 3.16, 3.19**) shows that identification of ro-vibrational lines in the experiment was correct and that the method of spectral line identification can be used for other vibrational bands.

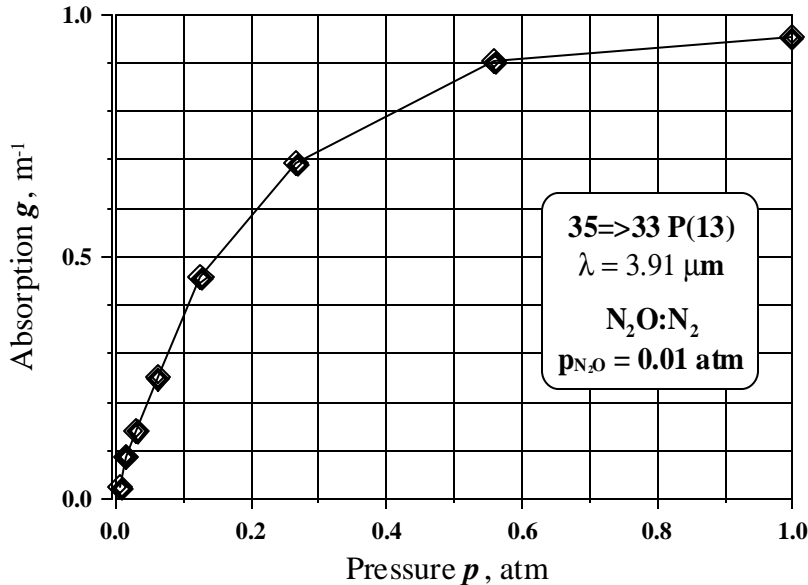


Fig.3.17. Dependence of absorption coefficient of gas mixture N₂O:N₂ on mixture pressure p at constant pressure of N₂O fraction (0.01 atm). Overtone transition 35→33 P(13) ($\lambda=3.91 \mu\text{m}$).

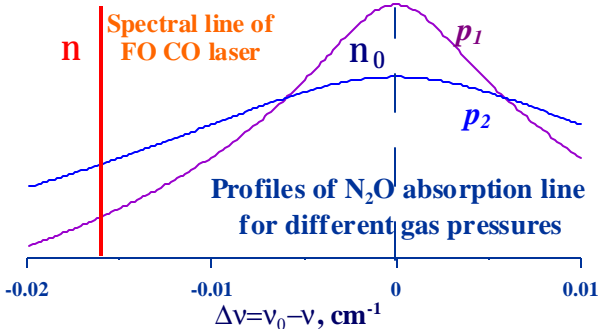


Fig.3.18. A spectral line of FO CO laser (v) and the profiles of N_2O absorption line (v_0 - center) for different gas pressures ($p_1 < p_2$).

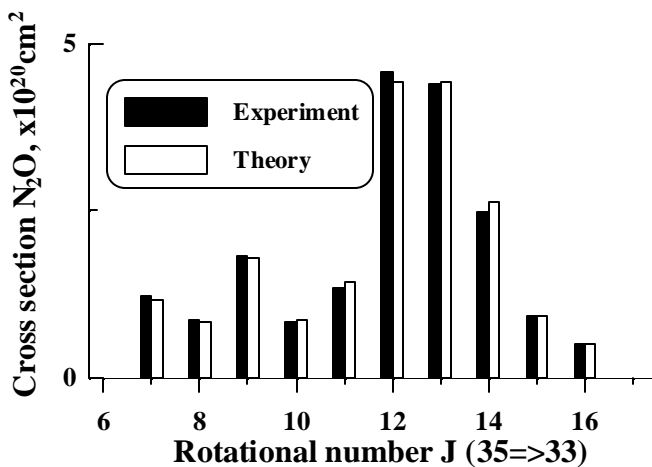


Fig. 3.19. N_2O absorption cross-sections for several FO CO laser spectral lines (vibrational transition $35 \rightarrow 33$). Experimental data was obtained by using photo acoustic system.

The results of the feasibility study of FO CO laser radiation absorption research demonstrated the real opportunity of measuring absorption characteristics of various organic and non-organic gaseous substances by using multi-line or single-line FO CO laser. To measure low concentration of absorber, it is needed to increase FO CO laser radiation intensity and to reach high amplification of electrical signal at low noise/signal level for the purpose of photo acoustic spectroscopy. To use the method for intracavity spectroscopy it is needed to change photo acoustic cell design installing Brewster window to the cell. The increase of CO laser radiation intensity and accuracy of spectroscopic measurement will allow us to study non-linear absorption in gaseous substances.

Conclusions

A comparative analysis of spectral emission characteristics of FO CO laser and HF (DF) laser demonstrated that FO CO lasing range $2.5\text{-}4.2 \mu\text{m}$ covers those of HF and DF lasers, the number of spectral lines lying in the same spectral band is much higher for FO CO laser. The potential of FO CO laser application for spectroscopic detection of various molecular trace gases is greater than that of HF and DF lasers.

Water vapor plays the principal role in FO CO radiation attenuation. Many of FO CO lines are undergone by very strong absorption in the atmosphere (for some lines absorption coefficient exceeds 1 m^{-1}). Such absorption is not obtainable for HF and DF lasers. Lines of FO CO laser with strong absorption by water can be used for laser heating, e.g., in medical applications. Alternatively, FO CO emission lines with $\lambda \geq 3.4 \mu\text{m}$ are excellent for efficient energy transmission through the atmosphere.

Temporal evolution of atmospheric absorption coefficients for different FO CO laser emission lines can be different - increasing or decreasing (for some lines the changes achieve several times of initial value). Intense multifrequency FO CO laser radiation can strongly change the absorption spectrum of atmospheric air. These changes depend on altitude and might be used in future for elaboration of novel methods in spectroscopic diagnostics of molecular gases, e.g., for aircraft wake visualization via its irradiation and nonuniform heating.

Optimum spectral regions are selected for detection of different organic and inorganic compounds. Spectroscopic experiments were carried out with multi- and single-line FO CO laser. Absorption coefficients of ethanol and acetone vapor, methane and N₂O for several ro-vibrational lines of single-line FO CO laser were measured. Photo acoustical system was manufactured and prepared especially for the experiments. Spectroscopic experiments demonstrated good agreement between theoretical and experimentally obtained data. The increase of CO laser radiation intensity and accuracy of spectroscopic measurement will allow us to study non-linear absorption in gaseous substances.

Table 3.1. Analytical lines of FO CO laser.

726 FO CO emission transitions $(V+2, J-1) \rightarrow (V, J)$ with $J = 4 \div 25$ and $V = 4 \div 36$ were examined. Conditions of atmospheric model No 6 - standard U.S. atmospheric model (Anderson et al. 1988; De Bievre et al. 1984) at altitude $H = 0$ km were used (total pressure $P=1$ atm, temperature $T=288.2$ K; relative concentrations of principal absorbing gases: H_2O - 7750 ppmV, CO_2 - 330 ppmV, CH_4 - 1.7 ppmV, N_2O - 0.32 ppmV).

Only those lines are selected for which $|v - v_i| < \gamma_i$ and individual absorption cross-section $\sigma(v) > 10^{-20} \text{ cm}^2$.

Lorentz contour is assumed for absorption lineshape. Continuum is not taken into account.

v - laser line wavenumber, cm^{-1} ; v_i - absorption line-center, cm^{-1} ;

Iso - molecular isotope number (1- most abundant, 2 – less abundant, etc.);

S_i - integral intensity of absorption line, $\text{cm}/\text{molec.}$:

γ_i - absorption line halfwidth, cm^{-1} ;

σ_i - absorption cross-section at frequency v caused by single-line considered, cm^2 ;

α_{air} - absorption coefficient in standard atmosphere at altitude $H = 0$ km, km^{-1} ;

I – index of atmospheric absorption strength for given laser line: * - medium absorption; ** - strong absorption; *** - very strong absorption. Lines possessing weak absorption are not labeled.

Laser line	v	v_i	Gas	Iso	$S_i \cdot 10^{19}$	γ_i	$\sigma_i \cdot 10^{19}$	$\alpha_{\text{air}} (\text{km}^{-1})$	I
37-35 P(16)	2448.3916	2448.3800	N_2O	1	.0508	.0768	.206	.074	
37-35 P(15)	2452.0593	2452.0449	HBr	1	.376	.0580	1.94	.057	
35-33 P(25)	2507.0795	2507.0890	HBr	2	.573	.0920	1.96	.020	
36-34 P(6)	2529.9428	2530.0049	N_2O	1	.0645	.0704	.164	.031	
35-33 P(19)	2532.1239	2532.1283	N_2O	1	.0807	.0707	.362	.040	
35-33P (13)	2554.7228	2554.6535	N_2O	1	.194	.0814	.439	.045	
35-33 P(12)	2558.2496	2558.2093	N_2O	1	.133	.0857	.406	.044	
35-33 P(11)	2561.7074	2561.6565	N_2O	1	.048	.0927	.127	.021	
34-32 P(22)	2567.4384	2567.4273	N_2O	1	.117	.0870	.421	.048	
35-33 P(7)	2574.8475	2574.7650	HBr	2	.280	.1230	.500	.017	
35-33 P(6)	2577.9590	2577.9648	N_2O	1	.232	.0752	.974	.090	
35-33 P(4)	2583.9726	2584.0318	N_2O	1	.147	.0717	.389	.039	
31-29 P(22)	2710.4484	2710.5141	H_2CO	1	.0694	.1080	.149	.055	
31-29 P(15)	2738.9260	2738.9985	H_2CO	1	.153	.1080	.311	.319	*
31-29 P(14)	2742.7236	2742.7403	H_2CO	1	.269	.1080	.774	.054	
		2742.7430	CH_4	1	.0234	.0620	.109		
30-28 P(25)	2744.9902	2744.9051	H_2CO	1	.199	.1080	.362	.023	
		2744.9488	H_2CO	1	.0924	.1080	.237		
		2745.0872	H_2CO	1	.109	.1080	.178		
30-28 P(24)	2749.4942	2749.4492	H_2CO	1	.368	.1080	.924	.020	
31-29 P(12)	2750.1143	2750.0187	H_2CO	1	.768	.1080	1.27	.012	
		2750.1377	HCl	2	.614	.0439	3.47		
		2750.2132	H_2CO	1	.218	.1080	.350		
31-29 P(11)	2753.7072	2753.7963	H_2CO	1	.234	.1080	.410	.162	*
30-28 P(21)	2762.6057	2762.5115	H_2CO	1	.126	.1080	.211	.015	

Laser line	ν	ν_i	Gas	Iso	$S_i \cdot 10^{19}$	γ_i	$\sigma_i \cdot 10^{19}$	$\alpha_{\text{air}} (\text{km}^{-1})$	I
31-29 P(8)	2764.0743	2764.0925	H ₂ CO	1	.710	.1080	.203	.025	
30-28 P(20)	2766.8423	2766.7602	H ₂ CO	1	.142	.1080	.265	.039	
		2766.8102	H ₂ CO	1	.124	.1080	.336		
		2766.8554	H ₂ CO	1	.102	.1080	.296		
		2766.8931	H ₂ CO	1	.0573	.1080	.138		
31-29 P(7)	2767.3923	2767.2859	H ₂ CO	1	.384	.1080	.575	.252	*
		2767.3038	H ₂ CO	1	.107	.1080	.189		
		2767.4971	H ₂ CO	1	.0839	.1080	.127		
31-29 P(6)	2770.6412	2770.5452	H ₂ CO	1	.341	.1080	.561	.018	
31-29 P(5)	2773.8209	2773.8250	HCl	2	.922	.0541	5.39	.040	
30-28 P(18)	2775.1138	2775.1770	H ₂ CO	1	.0843	.1080	.185	.005	
31-29 P(4)	2776.9313	2776.8686	H ₂ CO	1	.138	.1080	.304	.047	
30-28 P(15)	2787.0149	2786.9912	H ₂ CO	1	.126	.1080	.354	.055	
		2787.0187	H ₂ CO	1	.169	.1080	.497		
		2787.1069	H ₂ CO	1	.168	.1080	.287		
30-28 P(14)	2790.8463	2790.7385	H ₂ CO	1	.217	.1080	.320	.018	
30-28 P(13)	2794.6098	2794.5458	H ₂ CO	1	.130	.1080	.284	.020	
29-27 P(24)	2797.3927	2797.3727	H ₂ CO	1	.411	.1080	1.17	.144	*
29-27 P(23)	2801.8635	2801.7752	H ₂ CO	1	.184	.1080	.325	.119	*
		2801.8710	H ₂ CO	1	.196	.1080	.575		
30-28 P(11)	2801.9321	2801.8710	H ₂ CO	1	.196	.1080	.438	.087	
		2802.0183	H ₂ CO	1	.202	.1080	.364		
30-28 P(10)	2805.4907	2805.5506	H ₂ CO	1	.296	.1080	.668	.0159	
		2805.5722	H ₂ CO	1	.484	.1080	.909		
29-27 P(22)	2806.2676	2806.2136	H ₂ CO	1	.120	.1080	.283	.006	
		2806.2273	H ₂ CO	1	.122	.1080	.316		
		2806.2707	H ₂ CO	1	.168	.1080	.495		
30-28 P(9)	2808.9808	2808.9276	H ₂ CO	1	.163	.1080	.387	.054	
		2809.0143	H ₂ CO	1	.067	.1080	.180		
30-28 P(8)	2812.4021	2812.2957	H ₂ CO	1	.444	.1080	.664	.041	
		2812.3546	H ₂ CO	1	.323	.1080	.798		
		2812.4314	H ₂ CO	1	1.13	.1080	3.10		
		2812.4723	H ₂ CO	1	.227	.1080	.470		
29-27 P(20)	2814.8751	2814.8341	H ₂ CO	1	.238	.1080	.613	.159	*
		2814.8595	H ₂ CO	1	.311	.1080	.898		
29-27 P(19)	2819.0783	2819.0390	H ₂ CO	1	.552	.1080	1.44	.031	
30-28 P(6)	2819.0381	2819.0390	H ₂ CO	1	.552	.1080	1.63	.028	
30-28 P(5)	2822.2524	2822.1919	H ₂ CO	1	.819	.1080	1.84	.051	
29-27 P(18)	2823.2142	2823.2151	H ₂ CO	1	.256	.1080	.754	.030	
30-28 P(4)	2825.3974	2825.3647	H ₂ CO	1	.0565	.1080	.153	.037	
29-27 P(17)	2827.2827	2827.2111	H ₂ CO	1	.0674	.1080	.138	.262	*
29-27 P(16)	2831.2837	2831.2732	H ₂ CO	1	.180	.1080	.526	.022	

Laser line	v	v_i	Gas	Iso	S_i·10 ¹⁹	γ_i	$\sigma_i·10^{19}$	$\alpha_{\text{air}} (\text{km}^{-1})$	I
		2831.3540	H ₂ CO	1	.127	.1080	.263		
29-27 P(12)	2846.6098	2846.6304	H ₂ CO	1	.0653	.1080	.186	.012	
29-27 P(10)	2853.8641	2853.7816	H ₂ CO	1	.0581	.1080	.108	.041	
28-26 P(22)	2854.3549	2854.3196	H ₂ CO	1	.0609	.1080	.162	.075	
		2854.4276	H ₂ CO	1	.181	.1080	.367		
29-27 P(9)	2857.3885	2857.4838	H ₂ CO	1	.144	.1080	.239	.042	
28-26 P(21)	2858.7260	2858.8015	H ₂ CO	1	.264	.1080	.522	.075	
28-26 P(20)	2863.0302	2862.9268	H ₂ CO	1	.566	.1080	.870	.086	
		2862.9943	H ₂ CO	1	.411	.1080	1.09		
		2863.0230	CH ₄	1	.0159	.0403	.122		
		2863.0238	HCl	2	.708	.0892	2.51		
29-27 P(7)	2864.2313	2864.1288	H ₂ CO	1	.121	.1080	.188	.138	*
		2864.1561	H ₂ CO	1	.822	.1080	1.63		
28-26 P(19)	2867.2673	2867.1811	H ₂ CO	1	.411	.1080	.740	.051	
29-27 P(6)	2867.5494	2867.6320	H ₂ CO	1	.368	.1080	.684	.012	
28-26 P(18)	2871.4373	2871.3317	H ₂ CO	1	.290	.1080	.437	.068	
29-27 P(4)	2873.9781	2874.0718	H ₂ CO	1	.221	.1080	.372	.014	
28-26 P(15)	2883.5426	2883.5271	H ₂ CO	1	.110	.1080	.318	.029	
28-26 P(14)	2887.4424	2887.5024	H ₂ CO	1	.231	.1080	.520	.017	
27-25 P(25)	2888.9574	2888.9583	NO ₂	1	.0523	.0630	.264	.011	
		2888.9588	NO ₂	1	.0553	.0630	.279		
		2888.9899	NO ₂	1	.0395	.0630	.158		
		2888.9925	NO ₂	1	.0419	.0630	.162		
		2888.9981	NO ₂	1	.0302	.0630	.108		
		2889.0038	NO ₂	1	.0322	.0630	.105		
28-26 P(13)	2891.2743	2891.3317	NO ₂	1	.112	.0630	.310	.014	
28-26 P(12)	2895.0382	2894.9793	NO ₂	1	.0505	.0630	.136	.377	*
		2894.9804	NO ₂	1	.0549	.0630	.151		
		2894.9959	CH ₄	1	.112	.0470	.419		
		2895.0557	CH ₄	1	.0667	.0619	.318		
		2895.0986	H ₂ CO	1	.210	.1080	.472		
27-25 P(23)	2898.1009	2898.0466	NO ₂	1	.0428	.0630	.124	.008	
		2898.0490	H ₂ CO	1	.131	.1080	.314		
		2898.0491	NO ₂	1	.0478	.0630	.144		
		2898.0684	H ₂ CO	1	.0944	.1080	.255		
28-26 P(11)	2898.7339	2898.7904	NO ₂	1	.0388	.0630	.109	.023	
		2898.7928	NO ₂	1	.0440	.0630	.119		
28-26 P(8)	2909.4106	2909.3579	H ₂ CO	1	.0702	.1080	.167	.044	
27-25 P(19)	2915.5878	2915.5254	NO ₂	1	.0531	.0630	.136	.024	
		2915.5333	NO ₂	1	.0492	.0630	.142		
28-26 P(6)	2916.1849	2916.1769	NO ₂	1	.0452	.0630	.225	.509	*
		2916.1890	NO ₂	1	.0423	.0630	.213		

Laser line	v	v_i	Gas	Iso	S_i·10 ¹⁹	γ_i	$\sigma_i·10^{19}$	$\alpha_{\text{air}} (\text{km}^{-1})$	I
		2916.1975	NO ₂	1	.0543	.0630	.264		
		2916.2014	CH ₄	1	.183	.0552	.969		
		2916.2049	NO ₂	1	.0506	.0630	.232		
28-26 P(5)	2919.4686	2919.4552	NO ₂	1	.0430	.0630	.208	.020	
		2919.4641	NO ₂	1	.0409	.0630	.206		
28-26 P(4)	2922.6831	2922.6260	NO ₂	1	.0495	.0630	.137	.018	
		2922.6327	NO ₂	1	.0475	.0630	.146		
		2922.7017	NO ₂	1	.0507	.0630	.236		
		2922.7033	NO ₂	1	.0485	.0630	.222		
27-25 P(17)	2923.9288	2923.8436	H ₂ CO	1	.187	.1080	.340	.016	
		2923.8892	NO ₂	1	.0453	.0630	.164		
		2923.8908	NO ₂	1	.0435	.0630	.161		
27-25 P(16)	2927.9983	2927.9634	CH ₄	1	.281	.0630	1.09	.758	*
26-24 P(25)	2937.2113	2937.1162	H ₂ CO	1	.0948	.1080	.157	1.302	**
		2937.2348	CH ₄	1	.391	.0550	1.91		
27-25 P(8)	2958.1098	2958.1199	CH ₄	1	.632	.0617	3.18	2.493	**
26-24 P(17)	2972.4572	2972.3682	H ₂ CO	1	.0609	.1080	.107	.248	*
25-23 P(19)	3012.6528	3012.6139	CH ₄	1	.152	.0450	.616	23.096	***
		3012.6175	CH ₄	1	.228	.0540	.942		
		3012.6216	CH ₄	1	.379	.0530	1.69		
25-23 P(18)	3016.9259	3016.9395	CH ₄	1	.658	.0640	3.13	2.309	**
26-24 P(5)	3017.2157	3017.1631	CH ₄	1	.927	.0660	2.73	5.058	**
		3017.2281	CH ₄	1	.800	.0640	3.83		
		3017.2666	CH ₄	1	.919	.0660	2.78		
24-22 P(10)	3097.7481	3097.7442	HCl	1	.0092	.0090	.273	.621	*
23-21 P(14)	3131.3626	3131.3238	CH ₄	1	.0296	.0410	.121	1.919	**
		3131.3472	CH ₄	1	.0735	.0510	.420		
		3131.3825	CH ₄	1	.299	.0520	1.60		
		3131.3985	CH ₄	1	.0916	.0410	.403		
		3131.4013	CH ₄	1	.0983	.0510	.389		
22-20 P(25)	3131.7294	3131.7353	CH ₄	1	.170	.0510	1.05	1.532	**
		3131.7376	CH ₄	1	.173	.0510	1.05		
20-18 P(24)	3234.7988	3234.7520	NH ₃	1	.0410	.0887	.115	.445	*
20-18 P(20)	3253.5245	3253.4851	C ₂ H ₂	2	.0476	.0803	.152	1.884	**
21-19 P(8)	3253.4515	3253.4851	C ₂ H ₂	2	.0476	.0803	.161	1.541	**
20-18 P(19)	3258.0390	3257.9976	C ₂ H ₂	1	.765	.0818	2.37	3.550	**
21-19 P(6)	3260.7133	3260.7310	C ₂ H ₂	2	.0548	.0818	.204	3.086	**
21-19 P(4)	3267.6993	3267.6573	C ₂ H ₂	1	.661	.0861	1.97	.152	*
20-18 P(14)	3279.6024	3279.5459	C ₂ H ₂	1	.408	.1063	.952	1.395	**
19-17 P(24)	3284.1950	3284.1277	HCN	1	3.19	.1089	6.75	14.518	***
		3284.2443	C ₂ H ₂	1	.137	.1158	.319		
20-18 P(12)	3287.7544	3287.7544	C ₂ H ₂	1	1.10	.0977	3.60	.565	*

Laser line	ν	v_i	Gas	Iso	$S_i \cdot 10^{19}$	γ_i	$\sigma_i \cdot 10^{19}$	$\alpha_{\text{air}} (\text{km}^{-1})$	I
20-18 P(9)	3299.4714	3299.5205	C_2H_2	1	.770	.1027	1.94	.241	*
		3299.5273	HCN	1	2.35	.1269	4.94		
18-16 P(25)	3328.8419	3328.7759	HCN	1	3.31	.1215	6.69	.756	*
19-17 P(13)	3333.4944	3333.4551	C_2H_2	1	.183	.0629	.664	.291	*
		3333.5052	NH_3	1	.0422	.0845	.157		
		3333.5733	NH_3	1	.0704	.0862	.141		
19-17 P(8)	3353.1974	3353.2847	HCN	1	2.29	.1062	4.10	4.147	**
18-16 P(8)	3403.3237	3403.3841	NH_3	1	.106	.0998	.246	3.906	**
17-15 P(13)	3433.5663	3433.6307	NH_3	1	.066	.0877	.156	.623	*
16-14 P(20)	3452.6855	3452.6199	NH_3	1	.0499	.0863	.117	.315	*
16-14 P(18)	3461.9284	3461.9474	NH_3	1	.0376	.0998	.116	4.386	**
16-14 P(12)	3488.0387	3488.0220	H_2O	1	.0261	.0419	.171	317.2	***
16-14 P(11)	3492.1528	3492.1333	N_2O	1	.330	.0775	1.27	1.164	**
16-14 P(7)	3507.9254	3507.8652	OH	1	.168	.0830	.422	2.846	**
		3507.8972	NH_3	1	.0353	.0927	.111		
16-14 P(6)	3511.6968	3511.7678	NH_3	1	.106	.0937	.229	45.984	***
15-13 P(18)	3512.2115	3512.1756	NH_3	1	.107	.0937	.316	5.492	**
16-14 P(5)	3515.3993	3515.3148	NH_3	1	.0927	.0891	.174	.809	*
15-13 P(9)	3550.7754	3550.7628	NH_3	1	.0551	.0814	.210	10.537	***
15-13 P(8)	3554.7194	3554.7189	OH	1	.0340	.0830	.130	9.730	**
15-13 P(5)	3566.1386	3566.0801	H_2O	1	.0553	.0655	.150	397.57	***
15-13 P(4)	3569.8069	3569.7957	HOCl	1	.0226	.0600	.116	16.507	***
13-11 P(25)	3579.0190	3579.0256	HOCl	1	.0212	.0600	.111	16.561	***
13-11 P(24)	3584.1133	3584.0766	HOCl	1	.0291	.0600	.112	22.121	***
		3584.0816	HOCl	1	.0291	.0600	.121		
13-11 P(23)	3589.1411	3589.1551	HOCl	1	.0460	.0600	.231	104.29	***
		3589.1843	HOCl	1	.0363	.0600	.127		
		3589.1873	HOCl	1	.0363	.0600	.121		
14-12 P(12)	3589.1940	3589.1551	HOCl	1	.0460	.0600	.172	84.446	***
		3589.1843	HOCl	1	.0363	.0600	.188		
		3589.1873	HOCl	1	.0363	.0600	.190		
		3589.2281	HOCl	1	.0430	.0600	.173		
14-12 P(11)	3593.3784	3593.3326	HOCl	1	.0360	.0600	.121	237.75	***
		3593.3785	HOCl	1	.0555	.0600	.294		
14-12 P(10)	3597.4945	3597.4368	HOCl	1	.0552	.0600	.152	24.309	***
14-12 P(8)	3605.5212	3605.4891	HOCl	1	.0256	.0600	.106	19.996	***
13-11 P(19)	3608.5851	3608.6080	HOCl	1	.0222	.0600	.103	77.892	***
14-12 P(5)	3617.0455	3617.0584	HOCl	1	.0489	.0600	.248	67.174	***
13-11 P(16)	3622.4636	3622.4903	CO_2	1	.365	.0762	1.36	134.00	***
12-10 P(25)	3629.5530	3629.5281	HOCl	1	.0532	.0600	.241	4160.0	***
12-10 P(24)	3634.6825	3634.7045	HOCl	1	.0367	.0600	.171	32.430	***
13-11 P(12)	3640.0215	3640.0548	CO_2	1	.0732	.0672	.278	70.254	***

Laser line	v	v _i	Gas	Iso	S _i ·10 ¹⁹	γ _i	σ _i ·10 ¹⁹	α _{air} (km ⁻¹)	I
13-11 P(11)	3644.2410	3644.2238	CO ₂	1	.0233	.0661	.105	23.376	***
		3644.2808	HOCl	1	.0323	.0600	.119		
13-11 P(10)	3648.3922	3648.4257	HOCl	1	.0265	.0600	.107	168.16	***
12-10 P(17)	3668.7206	3668.7771	H ₂ O	1	.630	.0951	1.56	3079.6	***
12-10 P(13)	3686.6903	3686.7139	CO ₂	1	.241	.0682	1.00	172.95	***
11-9 P(23)	3690.5118	3690.5666	CO ₂	1	.337	.0690	.954	399.58	***
12-10 P(7)	3711.6014	3711.6224	CO ₂	1	.222	.0863	.772	370.08	***
12-10 P(6)	3715.5129	3715.5561	CO ₂	1	.0577	.0949	.160	33.161	***
11-9 P(16)	3724.3272	3724.3528	CO ₂	1	.558	.0762	2.09	237.97	***
10-8 P(23)	3741.4375	3741.4598	HF	1	4.85	.0310	32.8	499.37	***
10-8 P(14)	3784.6249	3784.5840	H ₂ O	1	.124	.0924	.357	712.56	***
10-8 P(11)	3797.8037	3797.7881	H ₂ O	1	.0775	.0860	.278	541.73	***
9-7 P(16)	3826.8277	3826.7539	H ₂ O	1	.328	.0904	.693	1402.0	***
8-6 P(23)	3843.7554	3843.7510	H ₂ O	1	.394	.0871	1.44	2804.0	***
9-7 P(10)	3853.5993	3853.5759	H ₂ O	1	.185	.0876	.627	2037.4	***
8-6 P(21)	3853.9633	3853.9661	H ₂ O	1	1.20	.0904	4.22	10076.	***
9-7 P(6)	3870.0791	3870.1299	H ₂ O	1	1.32	.0741	3.86	7541.5	***
7-5 P(21)	3905.4198	3905.3711	H ₂ O	1	.0368	.0732	.111	259.10	***
7-5 P(18)	3920.3349	3920.3119	HF	1	13.5	.1028	39.8	156.65	***
7-5 P(17)	3925.1721	3925.1350	H ₂ O	1	.0719	.0905	.217	1153.9	***
		3925.1760	H ₂ O	1	.116	.0887	.415		

Table 3.2. Analytical lines of HF laser (comment see in a title of Table 3.1). 58 lines of HF given by [Sengupta et al., 1979] were examined.

Laser line	v	v _i	Gas	Iso	S _i ·10 ¹⁹	γ _i	σ _i ·10 ¹⁹	α _{air} (km ⁻¹)	I
6-5 P(10)	2749.4869	2749.4492	H ₂ CO	1	.368	.1080	.967	.020	
6-5 P(8)	2838.3071	2838.3618	H ₂ CO	1	.118	.1080	.277	.070	
		2838.3862	H ₂ CO	1	.071	.1080	.136		
		2838.3971	H ₂ CO	1	.0702	.1080	.122		
6-5 P(7)	2880.4508	2880.4152	H ₂ CO	1	.223	.1080	.593	.015	
4-3 P(13)	2889.0386	2888.9899	NO ₂	1	.0395	.0630	.125	.012	
		2888.9925	NO ₂	1	.0419	.0630	.138		
		2888.9981	NO ₂	1	.0302	.0630	.108		
		2889.0038	NO ₂	1	.0322	.0630	.125		
		2889.0683	H ₂ CO	1	.228	.1080	.625		
		2889.1010	H ₂ CO	1	.0774	.1080	.171		
6-5 P(6)	2921.3201	2921.3014	NO ₂	1	.0383	.0630	.178	.046	
		2921.3095	NO ₂	1	.0367	.0630	.180		
		2921.3691	NO ₂	1	.0482	.0630	.152		
		2921.3747	NO ₂	1	.0460	.0630	.133		
6-5 P(5)	2961.0811	2961.0688	HCl	2	1.55	.0624	7.60	.300	*
3-2 P(8)	3280.5700	3280.5922	C ₂ H ₂	1	.620	.0861	2.15	1.528	**

Laser line	v	v _i	Gas	Iso	S _i ·10 ¹⁹	γ_i	$\sigma_i \cdot 10^{19}$	$\alpha_{\text{air}} (\text{km}^{-1})$	I
4-3 P(4)	3304.3349	3304.3650	C ₂ H ₂	2	.062	.0840	.208	.224	*
1-0 P(13)	3326.0181	3325.9456	HCN	1	2.96	.1278	5.58	7.674	**
3-2 P(4)	3461.4396	3461.4763	NH ₃	1	.0374	.0998	.105	31.833	***
1-0 P(10)	3489.5599	3489.5260	NH ₃	1	.0417	.0988	.120	1.035	**
		3489.5592	HF	1	.0043	.0100	.136		
3-2 P(3)	3503.6117	3503.5426	N ₂ O	1	.106	.0704	.244	37.210	***
1-0 P(9)	3542.1595	3542.1590	HF	1	.0266	.0103	.820	4.373	**
1-0 P(8)	3593.7062	3593.6767	HOCl	1	.0510	.0600	.218	47.865	***
		3593.7059	HF	1	.135	.0116	3.69		
2-1 P(4)	3622.5768	3622.5530	HOCl	1	.0548	.0600	.251	75.412	***
1-0 P(7)	3644.1430	3644.1428	HF	1	.553	.0145	12.1	18.700	***
2-1 P(3)	3666.3565	3666.3457	HOCl	1	.0231	.0600	.119	19.031	***
1-0 P(6)	3693.4130	3693.4129	HF	1	1.83	.0204	28.6	68.869	***
2-1 P(2)	3708.7832	3708.7024	OH	1	.214	.0830	.421	140.66	***

Table 3.3. Analytical lines of DF laser (comment see in a title of Table 3.1). 63 lines of DF given by [Sengupta et al., 1979] were examined.

Laser line	v	v _i	Gas	Iso	S _i ·10 ¹⁹	γ _i	σ _i ·10 ¹⁹	α _{air} (km ⁻¹)	I
3-2 P(7)	2570.5157	2570.5747	N ₂ O	1	.190	.0823	0.484	.046	
2-1 P(10)	2580.0932	2580.0485	N ₂ O	1	.210	.0738	0.663	.059	
1-0 P(13)	2583.4534	2583.3850	N ₂ O	1	.159	.0720	0.368	.037	
2-1 P(9)	2605.8041	2605.8040	HBr	2	.624	.0920	2.16	.015	
2-1 P(5)	2703.9965	2704.0106	H ₂ CO	1	.074	.1080	0.215	.003	
2-1 P(3)	2750.0841	2750.0187	H ₂ CO	1	.768	.1080	1.66	.014	
1-0 P(6)	2767.9674	2767.9523	H ₂ CO	1	.143	.1080	0.413	.025	
1-0 P(5)	2792.4318	2792.3511	H ₂ CO	1	.293	.1080	0.554	.027	
1-0 P(4)	2816.3765	2816.3557	H ₂ CO	1	.378	.1080	1.07	.027	
1-0 P(2)	2862.6467	2862.5818	H ₂ CO	1	.341	.1080	0.738	.023	
		2862.6077	H ₂ CO	1	.372	.1080	0.970		
		2862.6836	H ₂ CO	1	.305	.1080	0.805		
		2862.7499	H ₂ CO	1	.398	.1080	0.613		
1-0 R(7)	3057.9530	3057.9702	CH ₄	2	.023	.0588	0.112	1.246	**

Table 3.4. Comparison of spectral emission and absorption features of FO CO, HF and DF lasers within 2.5-4.2 μm spectral region based on the results of **Tables 3.1-3.3**.

Laser and spectral range, cm ⁻¹	Total number of tested laser lines	Density of laser lines, lines/cm ⁻¹	Percent of analytical laser lines among tested laser lines, %	Detecting inorganic molecules selected from HITRAN-96 database	Percent of weak absorbing lines in the atmosphere among laser analytical lines, %	Percent of strong absorbing lines in the atmosphere among laser analytical lines, %	Percent of very strong absorbing lines in the atmosphere among laser analytical lines, %
FO CO 2364.93- 4034.06	726	0.43	19	H ₂ O, CO ₂ , N ₂ O, CH ₄ , NO ₂ , NH ₃ , OH, HF, HCl, HBr, H ₂ CO, HOCl, HCN, C ₂ H ₂	41	13	28
HF 2749.49- 3693.41	58	0.06	33	N ₂ O, NO ₂ , NH ₃ , OH, HF, HCl, H ₂ CO, HOCl, HCN, C ₂ H ₂	26	16	42
DF 2750.08- 2463.33	63	0.22	17	N ₂ O, CH ₄ , HBr H ₂ CO	91	9	-

Table 3.5. Fifty most absorbed lines of FO CO laser in the atmosphere. 726 FO CO emission transitions (**V+2, J-1**) ® (**V, J**) with **J** = 4 ÷ 25 and **V** = 4 ÷ 36 were examined. Conditions of atmospheric model No 6 - standard U.S. atmospheric model at altitude **H** = 0 km were used. The lines are ordered in descending order of absorption coefficient. Computations were performed separately for two cases: with and without continuum absorption.

Laser line	v, cm ⁻¹	$\alpha_{\text{air}} (\text{km}^{-1})$ with contin.	$\alpha_{\text{air}} (\text{km}^{-1})$ no contin.
8- 6 P(21)	3853.96327	10043.	10036.
9- 7 P(6)	3870.07913	7503.	7497.
12-10 P(25)	3629.55301	4155.	4151.
12-10 P(17)	3668.72055	3075.	3069.
38-36 P(24)	2369.18124	2924.	2924.
8- 6 P(23)	3843.75541	2797.	2790.
9- 7 P(10)	3853.59929	2038.	2032.
9- 7 P(16)	3826.82768	1405.	1397.
13-11 P(8)	3656.48902	1378.	1372.
7- 5 P(17)	3925.17210	1150.	1148.
14-12 P(7)	3609.43154	1125.	1121.
10- 8 P(14)	3784.62486	717.	710.
9- 7 P(15)	3831.45951	690.	683.
12-10 P(21)	3649.67172	581.	575.
9- 7 P(8)	3861.97677	554.	547.
12-10 P(12)	3691.01304	553.	547.
10- 8 P(11)	3797.80367	546.	539.
10- 8 P(20)	3756.43786	524.	517.
10- 8 P(21)	3751.50457	514.	508.
9- 7 P(5)	3874.02676	508.	502.
10- 8 P(23)	3741.43748	506.	499.
38-36 P(25)	2364.92918	483.	483.
13-11 P(17)	3617.90477	472.	467.
9- 7 P(17)	3822.12824	464.	456.
11- 9 P(23)	3690.51185	406.	399.
15-13 P(5)	3566.13858	398.	396.
10- 8 P(10)	3802.06014	388.	381.
12-10 P(7)	3711.60138	377.	370.
8- 6 P(24)	3838.55148	334.	327.
16-14 P(12)	3488.03866	312.	312.
10- 8 P(24)	3736.30397	283.	277.
9- 7 P(20)	3807.62563	274.	267.
11- 9 P(8)	3758.91458	268.	262.
7- 5 P(21)	3905.41978	261.	258.
38-36 P(23)	2373.36532	258.	258.
11- 9 P(16)	3724.32725	244.	237.
14-12 P(11)	3593.37840	240.	238.

10- 8 P(18)	3766.10319	239.	232.
8- 6 P(17)	3873.57501	235.	229.
10- 8 P(5)	3822.31232	232.	224.
9- 7 P(21)	3802.65716	226.	219.
9- 7 P(7)	3866.06242	224.	218.
15-13 P(15)	3525.67663	221.	221.
8- 6 P(13)	3892.10702	210.	205.
11- 9 P(10)	3750.67740	208.	202.
11- 9 P(11)	3746.45604	202.	195.
8- 6 P(10)	3905.29186	199.	196.
10- 8 P(9)	3806.24812	189.	182.
12-10 P(13)	3686.69029	178.	171.
13-11 P(10)	3648.39215	174.	168.

Table 3.6. Fifty least absorbing lines of FO CO laser in the atmosphere. 726 FO CO emission transitions ($\mathbf{V}+2, \mathbf{J}-1$) ® (\mathbf{V}, \mathbf{J}) with $\mathbf{J} = 4 \div 25$ and $\mathbf{V} = 4 \div 36$ were examined. Conditions of atmospheric model No 6 - standard U.S. atmospheric model at altitude $\mathbf{H} = 0$ km were used. The lines are ordered in ascending order of absorption coefficient. Computations were performed separately for two cases: with and without continuum absorption.

Laser line	ν, cm^{-1}	$\alpha_{\text{air}} (\text{km}^{-1})$ with continuum	$\alpha_{\text{air}} (\text{km}^{-1})$ no continuum
31-29 P(9)	2760.68731	.0106	.0026
34-32 P(9)	2616.37580	.0107	.0014
31-29 P(13)	2746.45306	.0113	.0034
33-31 P(22)	2615.02977	.0118	.0024
31-29 P(16)	2735.06054	.0120	.0040
31-29 P(24)	2701.70687	.0131	.0050
30-28 P(18)	2775.11382	.0131	.0051
34-32 P(13)	2602.54833	.0136	.0035
28-26 P(23)	2849.91696	.0137	.0052
29-27 P(22)	2806.26756	.0138	.0056
34-32 P(4)	2632.10366	.0138	.0048
32-30 P(16)	2687.10766	.0141	.0057
33-31 P(19)	2627.44142	.0142	.0051
32-30 P(4)	2728.56865	.0144	.0064
32-30 P(15)	2690.93954	.0147	.0064
33-31 P(23)	2610.75792	.0149	.0054
33-31 P(18)	2631.44358	.0151	.0062
32-30 P(11)	2705.58525	.0153	.0072
33-31 P(14)	2646.77331	.0153	.0064
33-31 P(8)	2667.71626	.0157	.0069
32-30 P(24)	2654.01934	.0163	.0074
33-31 P(12)	2654.02896	.0165	.0076

31-29	P(25)	2697.23596	.0166	.0084
34-32	P(15)	2595.22263	.0172	.0068
33-31	P(25)	2602.01305	.0174	.0073
29-27	P(25)	2792.85529	.0177	.0096
33-31	P(13)	2650.43535	.0177	.0088
32-30	P(9)	2712.49707	.0178	.0097
27-25	P(23)	2898.10094	.0178	.0081
34-32	P(11)	2609.59976	.0181	.0086
29-27	P(8)	2860.84429	.0184	.0099
34-32	P(14)	2598.91970	.0186	.0084
32-30	P(18)	2679.24032	.0187	.0102
29-27	P(14)	2839.08263	.0190	.0106
34-32	P(23)	2563.19871	.0193	.0063
33-31	P(7)	2670.96560	.0193	.0107
34-32	P(10)	2613.02227	.0194	.0099
34-32	P(5)	2629.09721	.0195	.0105
31-29	P(12)	2750.11431	.0198	.0118
33-31	P(6)	2674.14565	.0204	.0118
27-25	P(25)	2888.95738	.0204	.0111
33-31	P(21)	2619.23439	.0204	.0112
29-27	P(12)	2846.60978	.0205	.0121
29-27	P(6)	2867.54936	.0205	.0118
34-32	P(17)	2587.62375	.0207	.0098
34-32	P(18)	2583.72221	.0207	.0094
32-30	P(23)	2658.39071	.0207	.0119
35-33	P(17)	2539.92998	.0208	.0045
32-30	P(17)	2683.20788	.0209	.0125
34-32	P(6)	2626.02105	.0213	.0122

Table 3.7. Vibrational relaxation processes included into computational model.

$$\text{Characteristic relaxation time is } t = \frac{\dot{e}k(\text{cm}^3/\text{s}) \times 10^{-6} \times \frac{1.03 \times 10^5}{k_B T} \times p_1 x_1}{\dot{e}} \text{, where } p_1, x_1 - \text{pressure and relative}$$

concentration of buffer gas. Typical concentrations used: CO₂ – 330 ppmV, H₂O – 7750 ppmV, O₂ – 2.09·10⁵ ppmV, N₂ – 7.81·10⁵ ppmV. p1 = 1 atm, T=300 K.

	Relaxation process		Rate constant k , cm ³ /s	t , s·atm
VT- processes				
k_3^M	$CO'_2(01^00) + M \leftrightarrow CO_2 + M$	N_2, O_2	$0.136 \cdot 10^{-21} \exp(18.6186 - 35.9205 \cdot T^{1/3})$	$5.33 \cdot 10^{-4}$
		CO_2	$0.136 \cdot 10^{-21} \exp(18.1335 - 40.2402 \cdot T^{1/3})$	4.95
		H_2O	$2.0 \cdot 10^{-11}$	$2.64 \cdot 10^{-7}$
k_{31}^M	$CO'_2(02^l0) + M \leftrightarrow CO_2(01^00) + M$	M	$2 \cdot k_3^M$	$M=N_2, O_2 2.67 \cdot 10^{-4}$ $M=CO_2 2.48$ $M=H_2O 1.32 \cdot 10^{-7}$
k_{32}^M	$CO'_2(03^l0) + M \leftrightarrow CO_2(02^l0) + M$	M	$3 \cdot k_3^M$	$M=N_2, O_2 1.78 \cdot 10^{-4}$ $M=CO_2 1.65$ $M=H_2O 8.79 \cdot 10^{-8}$
k_4^M	$H_2O'(010) + M \leftrightarrow H_2O + M$	N_2, O_2	$\exp(-32.973 + 2.0 \cdot T^{1/3} + 80.535 \cdot T^{2/3} + 68.1595 \cdot T^1)$	$8.45 \cdot 10^{-7}$
		CO_2	$0.5 \cdot k_4^{N_2}$	$5.12 \cdot 10^{-3}$
		H_2O	$\exp(-11.05 - 222.4 \cdot T^{1/3} + 924 \cdot T^{2/3} + 82.0 \cdot T^1)$	$7.52 \cdot 10^{-8}$
k_{41}^M	$H_2O'(020) + M \leftrightarrow H_2O(010) + M$	M	$2 \cdot k_4^M$	$M=N_2, O_2 4.23 \cdot 10^{-7}$ $M=CO_2 2.56 \cdot 10^{-3}$ $M=H_2O 3.76 \cdot 10^{-8}$
k_{42}^M	$H_2O'(030) + M \leftrightarrow H_2O(020) + M$	M	$3 \cdot k_4^M$	$M=N_2, O_2 2.82 \cdot 10^{-7}$ $M=CO_2 1.71 \cdot 10^{-3}$ $M=H_2O 2.51 \cdot 10^{-8}$
k_5^M	$O'_2(1) + M \leftrightarrow O_2 + M$	N_2	$1.12 \cdot 10^{-8} \exp(-152 \cdot T^{1/3})$	$3.39 \cdot 10^{-2}$
		O_2	$1.11 \cdot 10^{-8} \exp(-157 \cdot T^{1/3})$	$2.70 \cdot 10^{-1}$
		H_2O	$100 \cdot k_5^{N_2}$	$4.38 \cdot 10^{-2}$
		CO_2	$1.34 \cdot 10^{-12} \exp(-146.5 \cdot T^{1/3}) \cdot T$	984.11
k_{51}^M	$O'_2(2) + M \leftrightarrow O'_2(1) + M$	M	$2 \cdot k_5^M$	$M=N_2 1.70 \cdot 10^{-2}$ $M=O_2 1.35 \cdot 10^{-1}$ $M=H_2O 2.19 \cdot 10^{-2}$

				$M = CO_2 \quad 492.05$
VV' – processes				
k_6	$CO'_2(00^01) + N_2 \leftrightarrow CO_2 + N'_2(1)$		$4.16 \cdot 10^{-14} \exp(-2.072 \cdot 10^{-3} \cdot T + 8.842 \cdot 10^{-7} \cdot T^2) \cdot T^{1/2}$	$9.76 \cdot 10^{-8}$
k_7	$N'_2(1) + H_2O \leftrightarrow N_2 + H_2O'(010)$		$\exp(-17.658 - 149.023 \cdot T^{1/3} + 347.214 \cdot T^{2/3} - 881.093 \cdot T^1)$	$7.23 \cdot 10^{-5}$
k_8	$N'_2(1) + O_2 \leftrightarrow N_2 + O'_2(1)$		$\exp(-15.397 - 281.451 \cdot T^{1/3} + 902.709 \cdot T^{2/3} - 638.17 \cdot T^1)$	$5.41 \cdot 10^{-3}$
k_9	$H_2O'(010) + O_2 \leftrightarrow H_2O + O'_2(1)$		$1.73 \cdot 10^{-11} \cdot T^{1/2}$	$4.09 \cdot 10^{-8}$
		VV – processes		
k_{10}^M	$CO'_2(00^01) + M \leftrightarrow CO'_2(11^10, 03^00) + M$	N_2, O_2	$0.136 \cdot 10^{-15} \cdot T \cdot \exp(-15.456 + 424.029 \cdot T^{1/3} - 3852.67 \cdot T^{2/3} + 10672 \cdot T^1)$	$1.25 \cdot 10^{-5}$
		CO_2	$0.136 \cdot 10^{-15} \cdot T \cdot \exp(-9.45 + 218.23 \cdot T^{1/3} - 1687.7 \cdot T^{2/3} + 3909.27 \cdot T^1)$	$1.33 \cdot 10^{-2}$
		H_2O	$4 \cdot 10^{-15} \cdot T \cdot [1 - \exp(-960 \cdot T^1)]^3 \cdot [1 - \exp(-3380 \cdot T^1)]^{-1}$	$4.98 \cdot 10^{-6}$
k_{11}^M	$CO'_2(10^00) + M \leftrightarrow CO'_2(02^10) + M$	M	$6.128 \cdot 10^{-14} \cdot T$	$2.22 \cdot 10^{-9}$
k_{121}^M	$H_2O(100) + M \leftrightarrow H_2O(020) + M$	M	$1.15 \cdot 10^{-12} \cdot T^{1/2}$	$2.05 \cdot 10^{-9}$
k_{122}^M	$H_2O(001) + M \leftrightarrow H_2O(020) + M$	M	$1.15 \cdot 10^{-12} \cdot T^{1/2}$	$2.05 \cdot 10^{-9}$
k_{123}^M	$H_2O(100) + M \leftrightarrow H_2O(001) + M$	M	$1.15 \cdot 10^{-12} \cdot T^{1/2}$	$2.05 \cdot 10^{-9}$

Table 3.8. Some organic and inorganic compounds having noticeable absorption in 2.5-4.2 μm spectral range. OSR – optimum spectral region (the region of the greatest absorption of the gas considered in 2.5-4.2 μm range). MAE - maximum allowable exposure at $?=300$? (scaled from the Russian Standard in mg/m^3 [Grushko, 1986 and Grushko 1987]). HR – high-resolution spectra from HITRAN-96 database. LR – low-resolution ($4\text{-}6 \text{ cm}^{-1}$) spectra from NIST/EPA-93 database. For HR spectra only those spectral intervals were considered where integral intensity of absorption lines exceeds $10^{-23} \text{ cm/molec}$. For LR spectra only visual selection was applied. Background – typical concentrations for ground level of Standard US atmosphere (Anderson et al. 1988; De Bievre et al. 1984) and for forest air (Brimblecombe, 1986).

Substance	OSR, cm^{-1} (HR)	Background, ppbV	MAE, ppbV	Substance	OSR, cm^{-1} (LR)	Background, ppbV	MAE, ppbV
Water vapor H_2O	3580- 3950	$7.75 \cdot 10^6$		Acetone $\text{C}_3\text{H}_6\text{O}$	2890- 3110		148
Carbon dioxide CO_2	3570- 3645 3670- 3745	$3.3 \cdot 10^5$	$5 \cdot 10^5$	Benzene C_6H_6	3000- 3130		252
Ozone O_3	2970- 3060	0.27	15.4	Toluene C_7H_8	2800- 3150		160
Nitrous oxide N_2O	2525- 2600 3435- 3510	320		Pentane C_5H_{12}	2840- 3010	0.3	8524
Methane CH_4	2890- 3160	1700		1-Pentanol $\text{C}_5\text{H}_{12}\text{O}$	2820- 3010		2.8
Nitrogen monoxide NO	2630- 3780	0.3	32.8	Ethanol $\text{C}_2\text{H}_6\text{O}$	2700- 3050 3610- 3730		2670
Sulfur dioxide SO_2	2470- 2520	0.3	19.2	1-Butanol $\text{C}_4\text{H}_{10}\text{O}$	2820- 3010		33.2
Nitrogen dioxide NO_2	2850- 2935	$2.3 \cdot 10^{-2}$	21.4	Propylene C_3H_6	2850- 3150	0.15	1754
Ammonia NH_3	3150- 3600	0.5	58	p-Xylene C_8H_{10}	2790- 3150		46.3
Hydroxyl OH	3320- 3780	$4.4 \cdot 10^{-5}$		Acrolein $\text{C}_3\text{H}_4\text{O}$	2650- 2890		12.9
Hydrogen fluoride HF	3490- 3950	10^{-5}	6.15	Cyclopentane C_5H_{10}	2830- 3020		35
Hydrogen chloride HCl	2620- 3080	1	10	Cyclohexane C_6H_{12}	2840- 2970		409

Hydrogen bromide HBr	2380-2720	$1.7 \cdot 10^{-3}$		Acetic acid <chem>C2H4O2</chem>	3540-3620		24.6
Formaldehyde <chem>H2CO</chem>	2710-3000	2.4	9.8	Acetonitrile <chem>C2H3N</chem>	2840-3100		60
Hydrogen hypochlorite <chem>HOCl</chem>	3440-3790	$7.7 \cdot 10^{-3}$		Pyridine <chem>C5H5N</chem>	2990-3120		311
Hydrogen cyanide HCN	3200-3400	0.17	9.1	Butane <chem>C4H10</chem>	2830-3020	0.6	8465 2
Methyl chloride <chem>CH3Cl</chem>	2930-3150	0.7		Isobutane <chem>C4H10</chem>	2840-3010	0.25	
Acetylene <chem>C2H2</chem>	3190-3370	0.3		m-Chloraniline <chem>C6H6ClN</chem>	3000-3110 3990-3540		1.9
Ethane <chem>C2H6</chem>	2970-3000	2		Phenol <chem>C6H6O</chem>	3000-3130 3620-3680		2.6
Hydrogen sulfide <chem>H2S</chem>	2380-3780		5.8	1,2-Dichloroethane <chem>C2H4Cl2</chem>	2930-3050		249

Table 3.9. Absorption coefficients of ethanol and acetone vapor on three FO CO ro-vibrational lines measured at the pressure $P_{\text{ethanol}} \approx 3.9 \text{ kPa}$ and $P_{\text{acetone}} \approx 17.3 \text{ kPa}$, respectively.

	Absorption coefficient, cm^{-1}		
	24→22 P(16)	28→26 P(9)	32→30 P(12)
$\lambda, \mu\text{m}$	3.252	3.4403	3.6998
Ethanol	0.06	0.20	0
Acetone	0	0.16	0

References

Ageev B.G., Ionin A.A., Mitsel A.A., Nesmelov L.I., Ponomarev Yu.N., Rudenko V.P., Sazhina N.N., Sapozhnikova V.A., Seregin A.M., Sinitsyn D.V., Tvorogov S.D., Terletskaya S.V. 1989, Investigation of absorption coefficients for atmospheric gases on wavelengths of CO laser generation., Preprint of Institute optics of atmosphere No.65, Tomsk (in Russian).

Alexandrov N.L., Konchakov A.M., Son E.E., 1979, Sov. J. Techn. Phys., **49**, 1200.

Allen D.C., Price T.J., Simpson C.J.S.M., 1979, Chem. Phys., **41**, 449.

Allen D.C., Simpson C.J.S.M., 1980, Chemical Physics, **45**, 203.

Anderson G., Clough S., Kneizys F., Chetwynd J., Shettle E., 1988, AFGL Atmospheric Constituent Profiles (0 - 120 km), Air Force Geophysics Laboratory, AFGL-TR-86-0110, Environmental Research Paper No. 954,

Bachem E., Dax A., Fink T. et al. 1993, Appl. Phys., **B57**, 185

Basov N.G., V.A. Danilychev, A.A. Ionin, V.S. Kazakevich, I.B. Kovsh, 1978, *Kvantovaja Elektronika* 8, p.1058 (in Russian)

Basov N., Hager G., Ionin A., Kotkov A. et al., 1999a, Opt. Comm., 171, pp.107-112

Basov N., Hager G., Ionin A., Kotkov A. et al., 1999b, Multiline and single-line pulsed first-overtone CO laser frequency tuned within spectral range of 2.5-4.2 μm ", Preprint #15 of P.N.Lebedev Physics Institute, Moscow p.1-23

Basov N., A.Ionin, G.Hager et al., 1999c, Effictive multiline pulsed first-overtone CO laser operating in spectral range of 2.5-4.2 μm , Proc. Int. Conf. LASERS'98, 7-11 Dec, 1998, Tucson, AZ, USA, Ed. by V.Corcoran & T.Goldman, STS Press, McLean, VA, USA p.481,

Basov N., A.Ionin, G.Hager et al., 1999d, Frequency tunable single-line pulsed first-overtone carbon monoxide laser, Int. Forum on Advanced High Power Lasers and Applications (AHPLA'99), Osaka, Japan, 1-5 November

Basov N.G., Hager G.D., Ionin A.A., et al, 2000a, IEEE Journ.of Quant. Electronics, **36**, 810.

Basov N., Hager G. et al., 2000b, Quantum Electronics, **30**, 771-777

Basov N., Hager G. et al., 2000c, Quantum Electronics, **30**, 859-866

Basov N., Hager G. et al., 2000d, Opt. Commun., **180**, 285-300

Bergman R. C., J. W. Rich, 1977, Appl. Phys. Lett. 31, p.597.

Berns R.M., Van der Avoid, 1980, The Journal of Chemical Physics, **72**, 6104.

Billing G.D., 1980, Chemical Physics, **50**, p.165.

Billing G.D., 1984, Comput. Phys. Comm., **1**, 237.

Billing G.D., Cacciatore M., 1983, Chemical Physics Letters, **94**, 218.

Billing G.D., 1986. In: Non-equilibrium vibration kinetics, Ch.4. Ed. by M.Capitelli (Springer, Berlin).

Billingsley F.P., Krauss M., 1974, The Journal of Chemical Physics, **60**, 2767.

Blauer J.A., Nickerson G.R., 1974, A survey of vibrational relaxation rate data for processes important to CO₂-N₂-H₂O infrared plume radiation, AIAA Paper No 74-536, AIAA 7-th Fluid and Plasma Dynamics Conference, Paolo Alto, Ca, June 1-19

Boeuf J. P., Belenguer Ph., "Fundamental properties of RF glow discharges: An approach based on self-consistent numerical models", *Nonequilibrium Processes in Partially Ionized Gases*, Edited by M. Capitelli and J. N. Bardsley, Plenum Press, New York, 155, 1990.

Brimblecombe P. 1986, Air Composition & Chemistry. Cambridge University Press, Cambridge, London, etc.

Britan A.B., Starik A.M., 1980, Study of vibrationally- nonequilibrium flow in wedged nozzle in N_2 - CO_2 mixture, *Zh. Prikl. Matem. i Tekhn. Fiz.*, 4, p.41-50. (in Russian)

Cacciatore M., Billing G.D., 1981, *Chemical Physics*, **58**, 395.

Cacciatore M., Capitelli M., Billing G.D., 1983, *Chem. Phys.*, **82**, 1.

Cacciatore M., 2000, private communication

Chackerian C., et al, 1980, *The Journal of Chemical Physics*, **72**, 6107.

Chen J.C.Y., 1964, *J. Chem. Phys.*, **40**, 3507.

Chugunov A.V., Djidjoev M.S., Ivanov S.V., Panchenko V.Ya., 1985, Nonlinear absorption of strong IR radiation by triatomic molecules, *Opt. Lett.*, V. **10**, p.615-617

Clough S.A., Kneizys F.X., Davies R.W., 1989, Line shape and the water vapor continuum, *Atmospheric Research*, V. **23**, p. 229-241

Coletti C., Billing G.D., 2000, *The Journal of Chemical Physics*, **113**, 4869.

Colley A. D., Villarreal F., Baker H. J., Hall D. R., *Appl. Phys. Lett.*, **64**, 2916, 1994.

De Bievre P., Gallet M., Holden N.E., Barnes I.L., 1984, Isotopic Abundances and Atomic Weights of the Elements, *J. Phys. Chem. Ref. Data*, V. **13**, p.809-891.

Dem'yanov A.V., Kochetov I.V., Napartovich A.P., et al, 1980, *Teplofiz. Vys. Temp., (Moscow)* **18**, 916. (in Russian)

Dem'yanov A. V., Zhdanok S. A., Kochetov I. V. et al, 1981, *Journal of Applied Mechanics and Technical Physics*, **22**, 287.

Farrenq R. and Rossetti C. 1985, *Chem. Phys.*, **92**, 401

Gordietz B.F., Osipov A.I., Shelepin L.A., 1980, Kinetic processes in gases and molecular lasers. *Nauka Publ.*, Moscow, (In Russian).

Grigoriev I. S. , Meilikhov E. Z., "Handbook of physical quantities", Moscow, Energoatomizdat, 1991 (in Russian)

Grushko Ya.M. 1986, Harmful organic compounds in industrial emissions into atmosphere. Leningrad: Khimiya (in Russian)

Grushko Ya.M. 1987, Harmful inorganic compounds in industrial emissions into atmosphere. Leningrad: Khimiya (in Russian)

Guelachvili G., Villeneuve D., Farrenq R. et al., 1983, *J. Molec. Spectrosc.*, V. **98**, p.64.

Hake R.D., Phelps A.V., 1967, *Phys. Rev.*, **158**, 70.

Herzberg G. 1945, Infrared and Raman Spectra of Polyatomic Molecules, New York

Ilukhin B. I., Kochetov I. V., Ochkin V. N., Tskhai S. N., Napartovich A. P., Witteman W. J., 1998, *Quantum Electronics*, **28**, 497-501..

Ilukhin B. I., Udalov Yu. B., Kochetov I. V., Ochkin V. N., Heeman-Ilieva M. B., Peters P. J. M., Witteman W. J., *Appl. Phys.*, **B 62**, 113-127, 1996.

Ionin A.A., Kotkov A.A., Kurnosov A.K., Napartovich A.P. 1998a, et al, Proc. Int. Conf. LASERS'97, Dec 1997, New Orleans, LA, USA, STS Press, McLean, VA, p.92

Ionin A. A., Klimachev Yu. M., Kotkov A.A. et al, 1998b, "Experimental and theoretical study on first overtone carbon monoxide laser physics", Preprint #11 of P.N.Lebedev Physics Institute, Moscow, Russia.

Ionin A. A., Klimachev Yu. M., Konev Yu. B. et al, 1999, "Experimental and theoretical study of multiquantum vibrational kinetics in active medium of CO laser", Preprint #70 of P.N.Lebedev Physics Institute, Moscow, Russia.

Ionin A.A., Kotkov A.A., Kurnosov A.K., Napartovich A.P. et al, 1998c, *Opt. Comm.*, **155**, p. 197-205

Ionin A.A., A.A. Kotkov, A.K. Kurnosov, A.P. Napartovich et al, 1998d, Pulsed First-Overtone CO Laser: Effective Source of Radiation in Spectral Range of 2.5-4.0 μm , Preprint No.34 of Lebedev Physics Institute, Moscow, p. 1-16 (in Russian)

Ionin A.A., Kotkov A.A., Kurnosov A.K., Napartovich A.P., Seleznev L.V. et al, 1999, *Opt. Comm.*, **160**, p. 255-260

Ionin A.A., Klimachev Yu. M., Konev Yu. B., Kurnosov A.K. et al, 2000a, *Kvantovaya Electronika*, **30**, 573. [*Quantum Electron.*, **30**, 573.]

Ionin A.A., Klimachev Yu. M., Konev Yu. B., Kurnosov A.K. et al, 2000b, Interim Report #1 on ISTC project 1865-P

Ionin A.A., Klimachev Yu.M., Konev Yu.B., Kotkov A.A., Kurnosov A.K., Napartovich A.P., Seleznev L.V., Sinitsyn D.V., Terekhov Yu.V. "Theoretical modeling and experimental studies of the multi-quantum vibration exchange in vibrationally excited CO molecules". 2001a, *J. Phys. D: Appl. Phys.*, v.34, 1-7.

Ionin A.A., Klimachev Yu. M., Konev Yu. B., Kurnosov A.K. et al, 2001b, Interim Report #3 on ISTC project 1865-P

Kanazawa H., Matsuzaka F., Uehara M., Kasuya K., *IEEE J. of QE*-**30**, 1448, 1994.

Konev Yu.V., Kochetov I.V., Kurnosov A.K., Mirzakarimov B.A., 1994, *Kvantovaya Electronika*, **21**, 133 (in Russian)

Konev Yu.V., Kochetov I.V., Kurnosov A.K., Mirzakarimov B.A., 1994a, *J. Phys. D:Appl. Phys.*, **27**, 2054-2059.

Kneizys F.X., Shettle E.P., Abreu L.W., Chetwynd J.H., Anderson G.P., Gallery W.O., Selby J.E.A., Clough S.A., 1988, "User's guide on LOWTRAN-7", *Report AFGL-TR-88-0177*, Air Force Geophysics Laboratory, Hanscom AFB, Ma 01731

Kunn V. V., Leont'ev V.G., Novgorodov M. Z., Ochkin V. N., Shishkanov E. F., Stepanov V. A., "Compact gap single-mode radio-frequency excited laser with a hybrid unstable and waveguide cavity", ICPIG XXII Haboken, v.3, pp.67-68, 1995.

Langhoff S.R., Bauschlicher C.W., 1995, *The Journal of Chemical Physics*, **102**, 5220.

Likal'ter A.A., 1979, *Kvant. Electr.*, **6**, 1816-1818 (In Russian).

Ling M.S.H., Rigby M., 1984, *Molecular Phys.*, **51**, 855.

Mason E. A., Saxena S. C., *Physics of Fluids*, **1**, 361, 1958

Matveev V.S., 1972, Approximative descriptions of the absorption coefficient and the spectral linewidth with the Voigt profile, *Zh. Prikl. Spektrosk.*, V. **16**, 2, p.228-233 (in Russian)

McCord J., Tate R., Hager G., Ionin A., Seleznev L. et al., 2001, "Multi-line and single-line spectral characteristics of RF discharge supersonic CO laser", Proc. Int.Conf. LASERS 2000, 4-8 Dec 2000, Albuquerque, NM, USA, STS Press, McLean, VA, USA

Meyer P.L., Sigrist M.W. 1990, Atmospheric pollution monitoring using CO₂ - laser photoacoustic spectroscopy and other techniques, *Review of Scientific Instruments*. V. **61** , No 7 p. 1779-1807.

Napartovich A.P., Novobrantsev I.V., Starostin A.N., 1977, *Kvant. Electr.*, **4**, 2125 (In Russian).

Ochkin V. N., Witteman W. J., Ilukhin B. I., Kochetov I. V., Peters P. J. M., Udalov Yu. B., Tskhai S. N., *Appl. Phys.*, **B 63**, 575-583, 1996.

Penner S.S. 1959, Quantitative Molecular Spectroscopy and Gas Emissivities. Addison-Wesley, Reading

Reid J.P., Simpson C.J.S.M., 1997, *The Journal of Chem. Phys.*, **107**, 9929.

Reid J.P., Simpson C.J.S.M., et al, 1995, *The Journal of Chem. Phys.*, **103**, 2528.

Reuter D., Jennings D.E., 1986, *The Journal of Molec. Spectr.*, **115**, 294.

Rigrod W.W., 1963, *J. Appl. Phys.*, **34**, 2602.

Rockwood S., Brau J., Proctor W. et al., 1973, *IEEE J. Quantum Electronics*, **QE-9**, 120

Rothman L.S., Gamache R.R., Tipping R., et al., 1992, The HITRAN molecular database: editions of 1991 and 1992, *J. Quant. Spectrosc. Radiat. Transfer*, V. **48**, p.469-507. . [Update HITRAN-96 version on CD-ROM].

Sengupta U.K., Das P.K., Rao K.N., 1979, Infrared laser spectra of HF and DF , *J. Molec Spectrosc.*, V. **74**, p.322-326.

Smith N.S., Hassan H.A., 1976, *AIAA Journal*, **14**, 374.

Sobolev N., Sokovikov V., 1971, *Uspekhi Fizicheskikh Nauk*, **110**, 191 (*in Russian*)

Starostin S. A., Kochetov I. V., Peters P. J. M., Udalov Yu. B., Witteman W. J., Napartovich A. P., *Appl. Phys. B.*, **71**, 491, 2000.

Takayanagi K., 1966, *J. Phys. Soc. Japan*, **21**, 507.

Taylor R.L., Bitterman S., 1969, Survey of vibrational relaxation data for processes important in the CO₂-N₂ laser system, *Reviews of Modern Physics*, V. **41**(1), p.26-47.

Thibault F., Menoux V., LeDoucen R., et al., 1997, Infrared collision-induced absorption by O₂ near 6.4μm for atmospheric applications: measurements and empirical modeling, *Appl. Opt.*, V. **36**(3), p.563-567.

Thöny A. Sigrist M.W. 1990, New developments in CO₂ - laser photoacoustic monitoring of trace gases, *Infrared Phys. Technol.* V. **61**, No 7 p. 1779-1807.

Treanor C.H., Rich J.W., Rehm R.G., 1968, *J. Chem. Phys.*, **48**, 1798.

Urban W. 1991, *Laser und Optoelektronik*, **23**, 56

von Bulow H., Schellhorn M., *Appl. Phys. Lett.*, 63, 287-287, 1993a.

von Bulow H., Zeyfang E., *Rev. Sci. Instrum.* 64, 1784, 1993b.

Winter B.N., Silverman S.S., Benedict W.S., 1964, Line shape in the wing beyond the band head of the 4.3μ band of CO₂, *J. Quant. Spectrosc. Radiat. Transfer*, V. **4**(4), p.527-538.

Xin J., Zhang W., Jiao W., *Appl. Phys. Lett.*, **75**, 1369, 1999.

Yong L.A., Eachus W.J., 1966, *The Journal of Chemical Physics*, **44**, 4196.

Zeyfang E., Mayerhofer W., Walther S., 2000, "Room-temperature repetitively pulsed CO overtone laser", XIII Int. Symposium GCL/HPL, 18-22 Sept. 2000, Florence, Italy

Zhdanok S. A., Napartovich A. P., Starostin A. N., 1979, *Sov. Phys. JETP*, **49**, 66.

List of Publications

1. Ionin A., CO Overtone transition laser (invited paper), XIII Int. Symp. Gas Flow and Chemical Lasers and High-Power Lasers Conf., 18-22 Sept. 2000, Florence, Italy, Conf. Program, p. 49; Proc. SPIE (2001).
2. Ionin A. A., Klimachev Yu. M., Kotkov A.A. et al, Single-line pulsed first-overtone CO laser: small-signal gain and spectrum formation, Proc. Int.Conf. LASERS 2000, 4-8 Dec 2000, Albuquerque, NM, USA, STS Press, McLean, VA, USA (2001)
3. O. Buzykin, A. Ionin, S. Ivanov et al., Propagation of overtone CO laser radiation through the atmosphere, Proc. Int. Conf. LASERS 2000, 4-8 Dec 2000, Albuquerque, NM, USA, STS Press, McLean, VA, USA (2001).
4. McCord J., Tate R., Hager G., Ionin A., Seleznev L. et al., Multi-line and single-line spectral characteristics of RF discharge supersonic CO laser, Proc. Int.Conf. LASERS 2000, 4-8 Dec 2000, Albuquerque, NM, USA, STS Press, McLean, VA, USA (2001)
5. Vetroshkin S.V, Ionin A.A., Klimachev Yu.M., Kotkov A.A. et al., Time behavior of pulsed overtone CO laser gain, Proc. of "Scientific session of Moscow State Engineering-Physics Institute (Technical University)", v.4, p.46, 2001, Moscow (in Russian)
6. Buzykin O., Ionin A., Ivanov S. et al., Resonance gas medium absorption of first-overtone CO laser radiation, Proc. of "Scientific session of Moscow State Engineering-Physics Institute (Technical University)", v.4, p.46, 2001, Moscow (in Russian)
7. Ionin A.A., Klimachev Yu.M., Konev Yu.B., Kotkov A.A., Seleznev L.V., Kurnosov A.K., Napartovich A.P., Sinitsyn D.V., Terekhov Yu.V., Shnyrev S.A., Correction of pulsed CO laser theoretical model taking into account the recent experimental and theoretical researches, Proc. All-Russia Scientific Conference on Molecular physics of nonequilibrium systems, 28 May - 1 June 2001, Ivanovo - Ples, Russia, pp. 88-89, 2001. (in Russian)
8. Ionin A.A., Overtone CO laser ($\lambda=2.5\text{-}4.2 \mu\text{m}$) (invited paper), VII Intern. Conf. "Laser And Laser-Information Technologies: Basic Research and Applications": Program and Abstracts, June 22-26, 2001, Vladimir - Suzdal / Ed. by V.Ya. Panchenko, V.S. Golubev - ILIT RAS, Shatura - VSU, Vladimir, 2001, - p. 13. ISBN 5-89368-254-8, Proc. SPIE (2001).
9. Baldwin W.N., Hager G.D., Ionin A.A., Kochetov I.V., Konev Yu.B., McIver J.K., Napartovich A.P., Numerical studies of the fundamental and first-overtone transitions CO laser gain excited in slab RF discharge, VII Intern. Conf. "Laser And Laser-Information Technologies: Basic Research and Applications": Program and Abstracts, June 22-26, 2001, Vladimir - Suzdal / Ed. by V.Ya. Panchenko, V.S. Golubev - ILIT RAS, Shatura - VSU, Vladimir, 2001, - p. 40. ISBN 5-89368-254-8, Proc. SPIE (2001).
10. Buzykin O.G., Ionin A.A., Ivanov S.V., Kotkov A.A., Seleznev L.V., Quantative spectroscopic atmospheric pollution diagnostics using first-overtone CO laser radiation, VII Intern. Conf. "Laser And Laser-Information Technologies: Basic Research and Applications": Program and Abstracts, June 22-26, 2001, Vladimir - Suzdal / Ed. by V.Ya. Panchenko, V.S. Golubev - ILIT RAS, Shatura - VSU, Vladimir, 2001, p. 75. ISBN 5-89368-254-8, Proc. SPIE (2001).
11. Buzykin O., Ionin A., Ivanov S. et al., Linear and non-linear atmospheric absorption of first-overtone CO laser radiation, Optics of Atmosphere and Ocean, #5, 2001
12. Ionin A.A., Klimachev Yu.M., Konev Yu.B., Kotkov A.A., Kurnosov A.K., Napartovich A.P., Seleznev L.V., Sinitsyn D.V., Terekhov Yu.V. "Theoretical modeling and experimental studies of the multi-quantum vibration exchange in vibrationally excited CO molecules". 2001a, *J. Phys. D:*

